Cell

Article

Rational discovery of therapeutic PAK1 allosteric activators

Graphical abstract

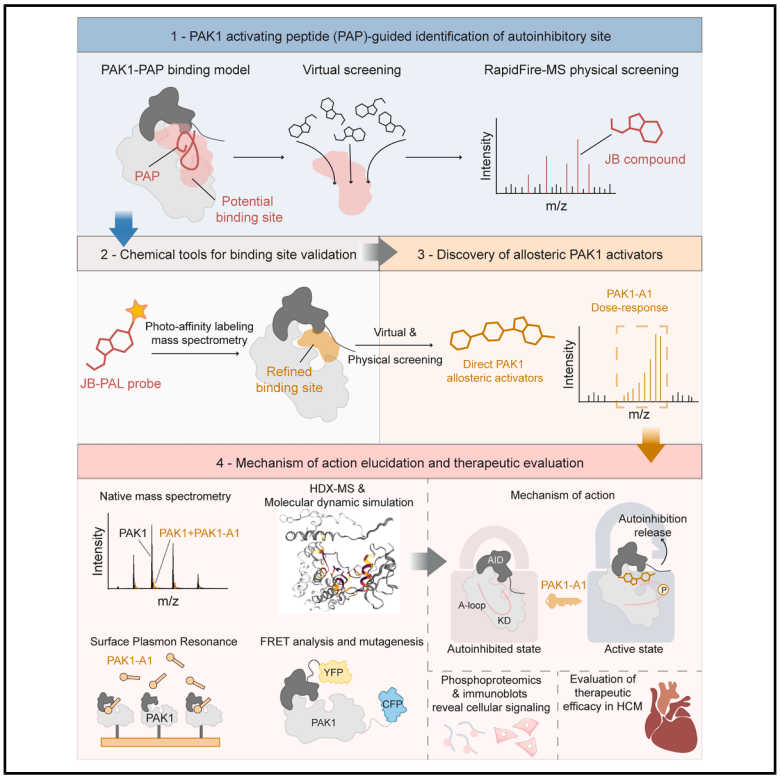

Highlights

- Peptide-guided strategy reveals an autoinhibition-release site in PAK1
- PAK1 activators selectively and directly enhance PAK1 activity *in vitro*
- Activators unlock PAK1 by displacing the kinase inhibitory segment
- PAK1 activators exhibit therapeutic effects in hypertrophic cardiomyopathy

Authors

Yu He (何钰), James S.H. Bae, Elżbieta Nowak, ..., Manuela Zaccolo, Marcin Nowotny, Ming Lei

Correspondence

shb45@cam.ac.uk (J.S.H.B.), ming.lei@pharm.ox.ac.uk (M.L.)

In brief

Kinase activators are difficult to develop despite their therapeutic promise. Here, we report the discovery of small-molecule p21-activated kinase 1 (PAK1) allosteric activators using a rational, peptide-guided strategy targeting the autoinhibitory mechanism. These compounds exhibit therapeutic efficacy in hypertrophic cardiomyopathy, underscoring the potential of this strategy for therapeutic kinase activator discovery.

He et al., 2026, Cell *189*, 3444–3464
May 28, 2026
https://doi.org/10.1016/j.cell.2026.03.008

CellPress

CellPress
OPEN ACCESS

Cell

Article

Rational discovery of therapeutic PAK1 allosteric activators

Yu He (何钰),[1,21] James S.H. Bae,[1,21,*] Elżbieta Nowak,[2,3] Carlos Outeiral,[4] Daniel A. Nissley,[4] Anthony Tumber,[5] Georgina Berridge,[6] Eidarus Salah,[5] Yi Wang,[7] Wenqi He,[8] Hongyuan Zhang,[8] Tangting Chen,[9] Samuel Tusk,[10,11] Sebastian Mathea,[12,13] Ying-Jie Wang,[14] Alexander Grassam-Rowe,[1] Philipp Kukura,[10,11] Christopher J. Schofield,[5] Darragh P. O'Brien,[6] Andrea Pierangelini,[6] Grant C. Churchill,[1] Thomas Lanyon-Hogg,[1] Yunbo Ke,[15] Chao Xu,[16] Tao Ye,[16,17] Hugh Watkins,[14] Liming Ying,[18] Andreas Koschinski,[19] R. John Solaro,[20] Xiaoqiu Tan,[9] Jani R. Bolla,[7] Xin Wang,[8] Stefan Knapp,[12,13] Charlotte M. Deane,[4] Manuela Zaccolo,[19] Marcin Nowotny,[2] and Ming Lei[1,22,*]

[1]Department of Pharmacology, University of Oxford, Mansfield Road, Oxford OX1 3QT, UK
[2]Laboratory of Protein Structure, International Institute of Molecular and Cell Biology, Trojdena 4, 02-109 Warsaw, Poland
[3]Preclinical Drug Development Facility at IN-MOL-CELL, International Institute of Molecular and Cell Biology, Trojdena 4, 02-109 Warsaw, Poland
[4]Department of Statistics, University of Oxford, Oxford OX1 3PB, UK
[5]Chemistry Research Laboratory, Department of Chemistry and the Ineos Oxford Institute for Antimicrobial Research, University of Oxford, 12 Mansfield Road, Oxford OX1 3TA, UK
[6]Target Discovery Institute, Centre for Medicines Discovery, Nuffield Department of Medicine, University of Oxford, Roosevelt Drive, Oxford OX3 7FZ, UK
[7]Department of Biology, University of Oxford, Mansfield Road, Oxford OX1 3SZ, UK
[8]Faculty of Biology, Medicine and Health, University of Manchester, Oxford Road, Manchester M13 9PT, UK
[9]Key Laboratory of Medical Electrophysiology of the Ministry of Education, Medical Electrophysiological Key Laboratory of Sichuan Province, Institute of Cardiovascular Research, School of Basic Medical Sciences, Southwest Medical University, Luzhou 646000, Sichuan, China
[10]Physical and Theoretical Chemistry Laboratory, Department of Chemistry, University of Oxford, South Parks Road, Oxford OX1 3QZ, UK
[11]The Kavli Institute for Nanoscience Discovery, Oxford OX1 3QU, UK
[12]Institute of Pharmaceutical Chemistry, Goethe-University Frankfurt, Max-von-Laue-Str. 9, 60438 Frankfurt, Germany
[13]Structural Genomics Consortium (SGC) and Buchmann Institute for Molecular Life Sciences, Max-von-Laue-Str. 15, 60438 Frankfurt, Germany
[14]Department of Cardiovascular Medicine, Wellcome Trust Centre for Human Genetics, University of Oxford, Oxford OX3 7BN, UK
[15]Department of Anesthesiology, University of Maryland School of Medicine, Baltimore, MD, USA
[16]State Key Laboratory of Chemical Oncogenomics, Peking University Shenzhen Graduate School, Shenzhen 518055, China
[17]Global AI Drug Discovery Center, College of Pharmacy and Graduate School of Pharmaceutical Sciences, Ewha Woman's University, Seoul 03760, Republic of Korea
[18]National Heart and Lung Institute, Imperial College London, Molecular Sciences Research Hub, 82 Wood Lane, London W12 0BZ, UK
[19]Department of Physiology, Anatomy and Genetics, University of Oxford, Parks Road, Oxford OX1 3PT, UK
[20]Department of Physiology and Biophysics, University of Illinois at Chicago, Chicago, IL 60612, USA
[21]These authors contributed equally
[22]Lead contact
*Correspondence: shb45@cam.ac.uk (J.S.H.B.), ming.lei@pharm.ox.ac.uk (M.L.)
https://doi.org/10.1016/j.cell.2026.03.008

SUMMARY

Although kinase activators hold significant therapeutic promise, their development remains challenging and rarely achieved. Here, we report the discovery of direct small-molecule activators of p21-activated kinase-1 (PAK1), a key regulator of cardiac homeostasis, using a rational peptide-guided strategy. Targeting PAK1 autoinhibitory regulation, we identified a previously unrecognized autoinhibition-release site between the autoregulatory region and the kinase domain. Subsequent high-throughput screening and medicinal chemistry optimization yielded selective allosteric activators that enhance PAK1 activity with micromolar potency and isoform selectivity. Structural and mechanistic analyses indicate that these activators disrupt autoinhibitory regulation and promote local and global conformational transitions to the active state. Enhanced PAK1 signaling was confirmed in cardiac cells, and *in vivo* studies demonstrated therapeutic efficacy in both inherited and acquired cardiac hypertrophy. Collectively, these findings establish rational modulation of kinase autoinhibitory regulation as a potential strategy for the broader discovery of kinase activators, a largely unexplored area of therapeutic development.

INTRODUCTION

Protein kinases, which represent ~1.7% of all human genes, are key modulators of a wide range of intracellular signal transduction pathways by modifying the activity of their substrate proteins via phosphorylation.[1] Given their significant roles in cellular functions and in diseases, protein kinases have emerged as a class of highly attractive therapeutic targets.[2] Although protein kinases have been extensively targeted for developing kinase inhibitors for cancer and immune dysregulation, the development of therapeutic kinase activators in cardiovascular, metabolic, neuroprotective, and regenerative medicine has encountered limited success.[3–5] Unlike kinase inhibitors that target highly conserved kinase domains, developing kinase activators requires an in-depth understanding of their individual regulatory mechanisms.[6,7] Metformin serves as an exemplary drug that highlights the beneficial implications of kinase activators.[8] By indirectly activating the energy-sensor AMP-activated protein kinase (AMPK), metformin exhibits benefit for the treatment of diabetes, cardiovascular diseases, and cancer. Other direct AMPK activators, such as A-769662 and O304, also hold promise in treating metabolic and cardiac diseases, highlighting the importance of understanding kinase activation mechanisms.[9–11] A more recent study has reported the development of a phosphatidylinositol 3-kinase (PI3K) activator for cardioprotection and neuroregeneration.[12] Despite some successes in recent years, only limited protein kinases have been successfully targeted, reflecting the challenges for developing kinase activators, including the difficulty in defining specific targeted sites, and underscoring the need for a new strategic approach.[6,7] The identification of key regulatory sites of kinases can therefore facilitate the development of activators and provide valuable biological insights into modulating kinase activity.[3,13,14]

In pursuit of a rational strategy, we have focused on PAK1, a member of the group 1 p21-activated kinases (PAKs), in the serine/threonine protein kinase family.[15] PAK1 plays a pivotal role in maintaining cellular homeostasis and metabolism, enhancing the adaptability of cardiomyocytes to stress. In PAK1, there are N-terminal regulatory domains, comprising a small GTPase-binding domain as well as an autoinhibitory domain (amino acid [aa] 67–150), which govern the kinase activity of the kinase domain (aa 249–545). In its inactive conformation, PAK1 is present as an autoinhibited dimer that can be activated by binding to the small GTPases Cdc42 and Rac1, triggering dimer dissociation and exposing the kinase domain for activation through autophosphorylation at Thr423 on the activation loop.[16,17] Over the past decade, a series of studies, including our own, have highlighted the therapeutic potential of PAK1 activation through genetic approaches and pathway agonists (e.g., FTY720) in treating pathological hypertrophy, heart failure, ischemic heart disease, and associated ventricular arrhythmias.[18–27] Moreover, in our previous study, we demonstrated that a bioactive PAK1-activating peptide (PAP) induces PAK1 activation and is associated with a significant reduction of pathological hypertrophy in both cellular and mouse models, but the precise molecular mechanism underlying this peptide's action remains to be defined.[28] Despite these findings highlighting the promising application of pharmacological PAK1 activation in the management of cardiovascular diseases, no direct PAK1 activators have been discovered to facilitate a deeper understanding of PAK1-mediated signaling dynamics and its therapeutic implications.

Here, we identified a series of allosteric PAK1 kinase activators using a rational and targeted strategy. We first employed the PAP, derived from the PAK1 autoinhibitory domain, as a molecular guide to identify an allosteric regulatory site within PAK1. This site, located between the autoinhibitory domain and the kinase domain, serves as an autoinhibition-release region, encompassing the Asp-Phe-Gly motif, Glu315 on the αC helix, and the kinase inhibitory segment. Then, by targeting this allosteric site, we identified small-molecule PAK1 activators (denoted as JB compounds) capable of directly and effectively activating the PAK1 protein. Using these chemical tools, further photo-affinity labeling-coupled mass spectrometry (PAL-MS) studies elucidated the key binding site of the PAK1 activators, leading to the identification of more potent and effective small-molecule activators, such as PAK1-A1, which demonstrates selectivity over other group I PAK isoforms. Moreover, hydrogen-deuterium exchange (HDX)-MS, biochemical assays, mutagenesis analyses, and structural studies confirmed the direct binding of these activators to PAK1 and demonstrated their mechanism of action by alleviating autoinhibitory regulation and inducing conformational changes in PAK1. We also demonstrated that PAK1 activators effectively activate PAK1 signaling in both *in vitro* and *in vivo* settings, demonstrating therapeutic potential for treating both acquired and inherited forms of hypertrophic cardiomyopathy (HCM). Overall, by leveraging a PAP as an initial molecular guide, we successfully discovered small-molecule activators that alleviate autoinhibition and enhance kinase activity. To further explore the potential of this peptide-guided screening strategy, we applied it to protein kinase A (PKA) and identified a PKA-activating peptide derived from the regulatory subunit RIα. Through this peptide-guided identification of a potential allosteric site, we discovered allosteric PKA activators. Building on this mechanistic understanding of kinase activation, the peptide-guided screening strategy targeting autoinhibitory regulation may offer a promising approach to facilitate the early-stage discovery of other kinase activators.

RESULTS

Bioactive peptide-guided identification of an autoinhibition-release site

Our previous study reported a bioactive PAP,[28] derived from the PAK1 kinase inhibitory segment (aa 136–149) within the autoinhibitory domain, which exhibited a concentration-dependent stimulatory effect on PAK1 (Figures 1A and 1B); however, the underlying mechanism by which PAP activates PAK1 remains unclear. To understand the interaction between PAP and full-length PAK1, we performed surface plasmon resonance (SPR) analysis, which revealed a dose-dependent and reversible interaction with an equilibrium dissociation constant (K_D) of 2.69 ± 1.21 μM (Figure 1D). To further elucidate the PAP-PAK1 interaction, and given the lack of a full-length PAK1 crystal structure, we used AlphaFold2 to model the structure of PAP-bound PAK1.[29] In the autoinhibited state of PAK1, the kinase inhibitory segment

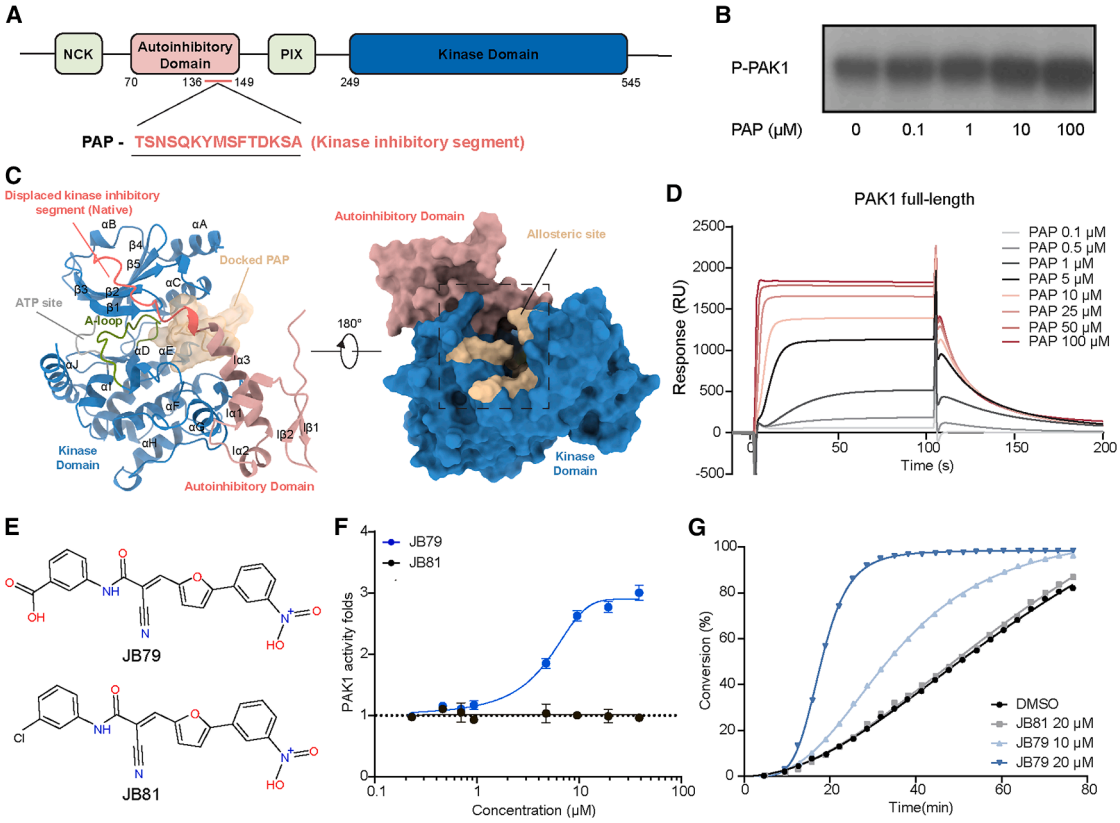

Figure 1. Bioactive peptide-guided identification of autoinhibition-release site

(A) PAP sequence, derived from the PAK1 kinase inhibitory segment.

(B) PAP enhances cellular PAK1 activity in a dose-dependent manner.

(C) AlphaFold2-predicted model for PAP-bound PAK1 (UniProt: Q13153) complex (left) and the potential allosteric active site for PAK1 activator screening (right). Docked PAP: shown in light brown, this segment is the PAP docked into the PAK1 full-length structure. Displaced kinase inhibitory segment (native): shown in coral red, this is the native kinase inhibitory segment within the autoinhibitory domain of the full-length PAK1 structure. It has been dislocated due to the presence of the docked PAP. The low-confidence flexible loop within the PAK1 structure (aa 1–16; aa 87–185) has been removed for clarity.

(D) Representative surface plasmon resonance (SPR) sensorgrams from three independent experiments showing the binding of PAP to full-length PAK1 at the indicated PAP concentrations. Binding is observed as an increase in resonance units (RUs) relative to baseline, demonstrating a dose-dependent interaction. The equilibrium dissociation constant (K_D = 2.69 ± 1.21 μM) was determined by steady-state (equilibrium) analysis, as described in the STAR Methods.

(E) Chemical structures of PAK1 activator JB79 (up) and a control compound JB81 (bottom). JB79 and JB81 are structurally identical except for the substituent on the phenyl ring adjacent to the amide. In JB79, this phenyl ring carries a meta-carboxylic acid group, whereas in JB81 the same position contains a meta-chlorine substituent.

(F) Dose-response curves for JB79 and JB81 were generated to assess their effects on PAK1 activity. RapidFire-MS was applied for the direct quantification of PAK1 activity, measuring PAK1 kinase activity based on the ratio of phosphorylated to total PAK1 substrate peptide. Data are presented as mean ± SEM. n = 3.

(G) Kinetic study of JB79 and JB81 to assess their time-dependent effects on PAK1 activity as the percentage conversion to phosphorylated/total PAK1 substrate.

See also Figure S1.

occupies the cleft between the N- and C-lobes of the kinase domain, interacting with the active site, where Lys141 makes hydrogen bonds with Asp389 of the catalytic loop and Asp407 of the activation loop.[16] This conformational arrangement induces a turn in the activation loop, thereby hindering the interaction between Glu315 of the αC helix and Lys299, preventing ATP binding.[16] AlphaFold2 analysis predicts that PAP binds at this interface between the autoinhibitory domain and kinase domain, displacing the native kinase inhibitory segment from the kinase domain (Figures 1C and S1A). Based on these findings, we proposed a potential mechanism in which PAP activates PAK1 by disrupting its autoinhibitory interactions, exposing the autophosphorylation site and the ATP-binding site and inducing an activating conformational change.

We hypothesized that this autoinhibition-release site can serve as a promising target for developing small-molecule activating compounds. To test this, we screened approximately 2 million compounds from the ZINC[15] in-stock lead-like library against this site using Autodock Vina[30] and ICM-VLS.[31] The top 100 compounds were further evaluated using a high-throughput RapidFire liquid chromatography-MS (LC-MS) enzymatic assay, which directly measures the kinase substrate phosphorylation[32] (Figure S1A). Among 18 initial hit compounds that demonstrated PAK1 activation, JB01 and JB79 emerged as notable activators,

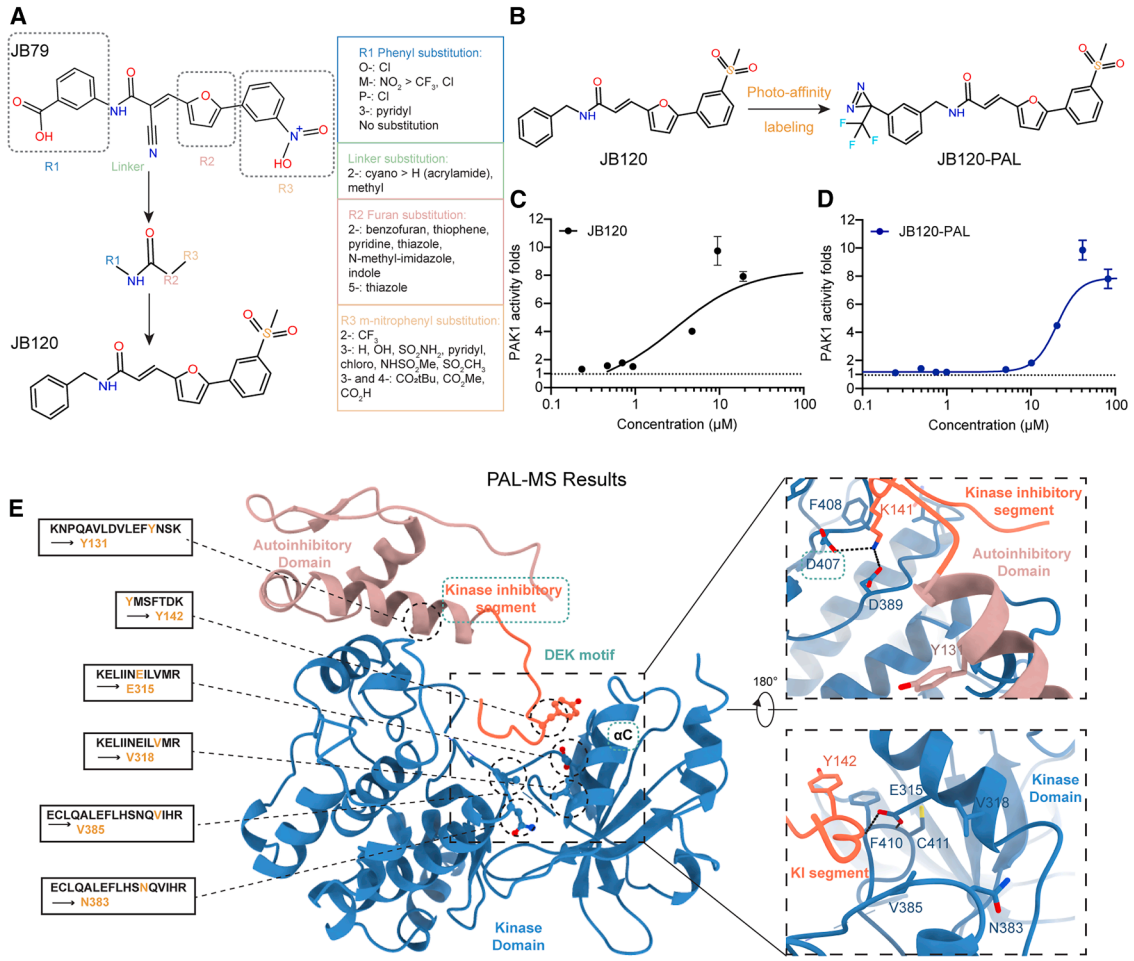

Figure 2. PAL-MS identifies key residues in the autoinhibition-release site for PAK1 activator JB120 binding

(A) Structure-activity relationship study and optimization of JB79. JB120 was derived during the optimization process.

(B) Development of a photo-labeling chemical probe based on JB120 with photocross-linker diazirine groups at the meta ring positions.

(C and D) Dose-response analysis of JB120 (C) and probe JB120-PAL (D) on PAK1 activity. Data are presented as mean ± SEM. $n = 3$.

(E) Identification of key residues involved in JB120 binding to PAK1 through PAL-MS. The key residues are mapped on one of the PAK1 monomer structures (PDB: 1F3M).

See also Figure S2.

displaying a dose-dependent kinase activation and achieving an approximately 3-fold increase in PAK1 activity (JB79, half maximal effective concentration [EC_{50}] = 3.63 ± 0.29 μM) (Figures 1E, 1F, and S1B–S1D). In the presence of Cdc42, a known GTPase that interacts with and activates PAK1, the effect of these compounds on PAK1 activation was significantly increased (Figures S1C and S1E). In contrast, JB79 failed to activate the isolated PAK1 kinase domain lacking the autoinhibitory domain (Figure S1E), suggesting that JB79's effect on PAK1 activation may depend on its interaction with the autoinhibitory domain (Figure S1E). Consistently, binding predictions showed that JB79 occupies the autoinhibition-release site through hydrophobic interactions involving Lys141, Glu315, and Asp407 (Figure S1F).

To define the relationship between the chemical structure of JB79 and its biological activity, we performed structure-activity relationship (SAR) studies. These analyses identified three key moieties in PAK1 activators: the R1 group (*m-carboxyphenyl*), the R2 group (*furan*), the R3 group (*m-nitrophenyl*), and a linker connecting these groups. We observed that the choice of the R1 moiety plays a crucial role in modulating the compound's effect on PAK1 activity. Substitution of the R1 carboxylic acid with a halogen (JB81) abolished the effect on activating PAK1 despite close structural similarity to JB79 (Figures 1E–1G). Furthermore, these three moieties were modified and substituted with a diversity of chemical moieties to expand the SAR (Figure 2A). Among 63 synthesized analogs from the SAR analysis, 21 exhibited a stimulatory effect on PAK1 activity. Notably, JB120 exhibited a 10-fold increase in activity in the presence of Cdc42 (EC_{50} 5 μM), demonstrating higher functional potency than JB79 (Figure 2C).

To investigate the binding mode of JB120, we conducted co-crystallization studies using the kinase domain^{K299R} together with the autoinhibitory domain. In the presence of DMSO, the

structure adopted a dimeric conformation (Figure S2A), closely resembling the previously reported autoinhibited PAK1 structure (PDB: 1F3M).[16] Co-crystallization trials with JB120 resulted in previously unreported *cis*-autoinhibited PAK1 monomer crystals, adopting an Asp-Phe-Gly (DFG)-in and αC-in conformation, where the A-loop folds back, inhibiting substrate binding (Figure S2B). However, no electron density corresponding to JB120 was detected. The JB120-soaked crystals revealed the absence of the kinase inhibitory segment and an outward shift of the autoinhibitory domain from the kinase domain (Figure S2C); we speculate that this disruption of the kinase inhibitory segment may hinder the formation of a fully enclosed binding pocket necessary for JB120 binding.

To investigate the binding site of JB120, PAL-MS was applied.[33,34] The new insights from SAR studies led to the design of a photocrosslinking chemical probe (JB120-PAL), where JB120 was labeled with a photo-affinity diazirine group, which facilitated structural proteomics analysis to identify the ligand-binding sites (Figures 2B, 2D, and S2D–S2G). Key residues crosslinked with the photo-affinity reporter are located at the interface between the kinase domain and autoinhibitory domain, where autoinhibition of PAK1 activity is regulated. Among these key residues, Tyr131, Tyr142, Glu315, Asn383, Val318, and Val385 were identified as crucial contributors to the binding of JB120-PAL to PAK1 (Figure 2E). These residues define a regulatory region encompassing the DFG motif, Glu315 of the αC helix, and the kinase inhibitory segment, which we term the "DEK" motif. Collectively, these data support a model in which JB120 activates PAK1 by disrupting autoinhibitory regulation through interference with the kinase inhibitory segment.

Targeting the autoinhibition-release site for identification of allosteric PAK1 activators

The JB compounds served as valuable chemical tools in identifying and characterizing the autoinhibition-release site, providing insights into the regulation of PAK1 activity. This allosteric mechanism of kinase activation presents promising opportunities for further identification of pharmacological PAK1 activators for therapeutic applications. Building on PAL-MS results, we identified the more localized and refined DEK motif for activator binding. Leveraging this refined binding site, we performed another virtual screening, using FRED docking,[35] which included U.S. Food and Drug Administration (FDA)-approved drugs (1,615 ligands) from the ZINC[15] database and experimental compounds (6,252 ligands) from DrugBank, as a proof of concept to determine whether a more accurate pocket could facilitate the discovery of improved activators.[36] Given that PAL-MS results indicated PAK1 activators function by releasing autoinhibition mediated by the kinase inhibitory segment, and considering that this segment occupies the active site within the PAK1 kinase domain, we removed the kinase inhibitory segment from the PAK1 monomer to prevent interference from the segment during virtual screening. Subsequently, we conducted RapidFire-MS-based physical screening of the top 25 ranked compounds and identified 5 hits that demonstrated a stimulatory effect on PAK1 (Figure S3A). Among these, PAK1-A1 (Eltrombapag, a thrombopoietin (TPO) receptor agonist[37]; EC_{50} = 1.6 ± 0.23 μM) and PAK1-A2 (TPO agonist 1[38]; EC_{50} of 2.575 ± 0.094 μM) (Figures 3A and 3B) emerged as the most effective and potent activators (Figures 3A and 3B). These compounds, identified through the DEK-site-focused screening, demonstrated improved binding potency and PAK1 stimulation compared with initial hits such as JB79, underscoring the enhanced precision and accuracy of the screening pocket following the PAL-MS insights. Due to its substantial stimulatory effects and favorable potency, PAK1-A1 was selected as a chemical probe for investigating the PAK1 activators' action mechanism. As a control, NVS-PAK1-1 (half maximal inhibitory concentration [IC_{50}] = 0.089 ± 0.018 μM) (Figure 3C), a previously reported selective allosteric PAK1 inhibitor,[39] was included to gain further insights into the conformational changes and molecular mechanisms underlying PAK1 regulation.

To investigate direct binding of activators to full-length PAK1, we performed native MS analysis.[40] Apo full-length PAK1 displayed a charge state series corresponding predominantly to a monomeric form of PAK1 with multiple phosphorylation states, indicating its intrinsic autophosphorylation activity, with a minor dimeric population (~1%) (Figure S3B). Upon pre-incubation with PAK1-A1 (1:30 molar ratio), additional peaks corresponding to the PAK1-PAK1-A1 complex were detected, supporting direct ligand binding. In the presence of PAK1-A1, only monomeric PAK1 was observed, and the binding of PAK1-A1 occurred across all phosphorylation states of PAK1, including the non-phosphorylated and mono-/multi-phosphorylated forms (Figure 3D).

To characterize the interactions of PAK1 with these small-molecule modulators, we carried out co-crystallization studies using PAK1-kinase domain^{K299R} in the apo state and in the presence of PAK1-A1 and NVS-PAK1-1. Obtaining the co-crystal structure of PAK1-kinase domain^{K299R} complexed with PAK1-A1 proved challenging, one possible reason could be the open and flexible conformation of PAK1 induced by activators. Nevertheless, we conducted structural analyses to investigate potential conformational changes induced by binding. Structures of the kinase domain^{K299R} in the apo state and in complex with PAK1-A1 or NVS-PAK1-1 revealed an asymmetric dimer in all conditions (Figures S3C–S3F).

Structural superposition showed that monomer A adopts a closed conformation, with the N- and C-lobes rotated inward by ~20° and the αC helix shifted toward the active site, relative to monomer B (Figure S3D). This asymmetric kinase domain dimer resembles an authentic "enzyme-substrate" complex,[41] where the activation loop of monomer A is inserted into the active site of the "enzymatic" monomer B (Figure S3C). In the PAK1-kinase domain^{K299R} + NVS-PAK1-1 complex, the inhibitor only binds to one monomer at an allosteric DFG-out site composed of the gatekeeper methionine (Met344), αC helix (Glu315), and the DFG motif (Asp407 and Phe408) (Figure 3E; Table S1). NVS-PAK1-1 binding induced a rotational movement of the small lobe with an outward shift of the αC helix and a 180° flip of the DFG motif, adopting an inactive DFG-out conformation (Figure 3G). However, PAK1-kinase domain^{K299R} crystals obtained in the presence of PAK1-A1 showed no detectable ligand density or evident conformational changes, where the kinase remained in a DFG-in state with only minor αC helix movement relative to the apo structure (Figure 3H).

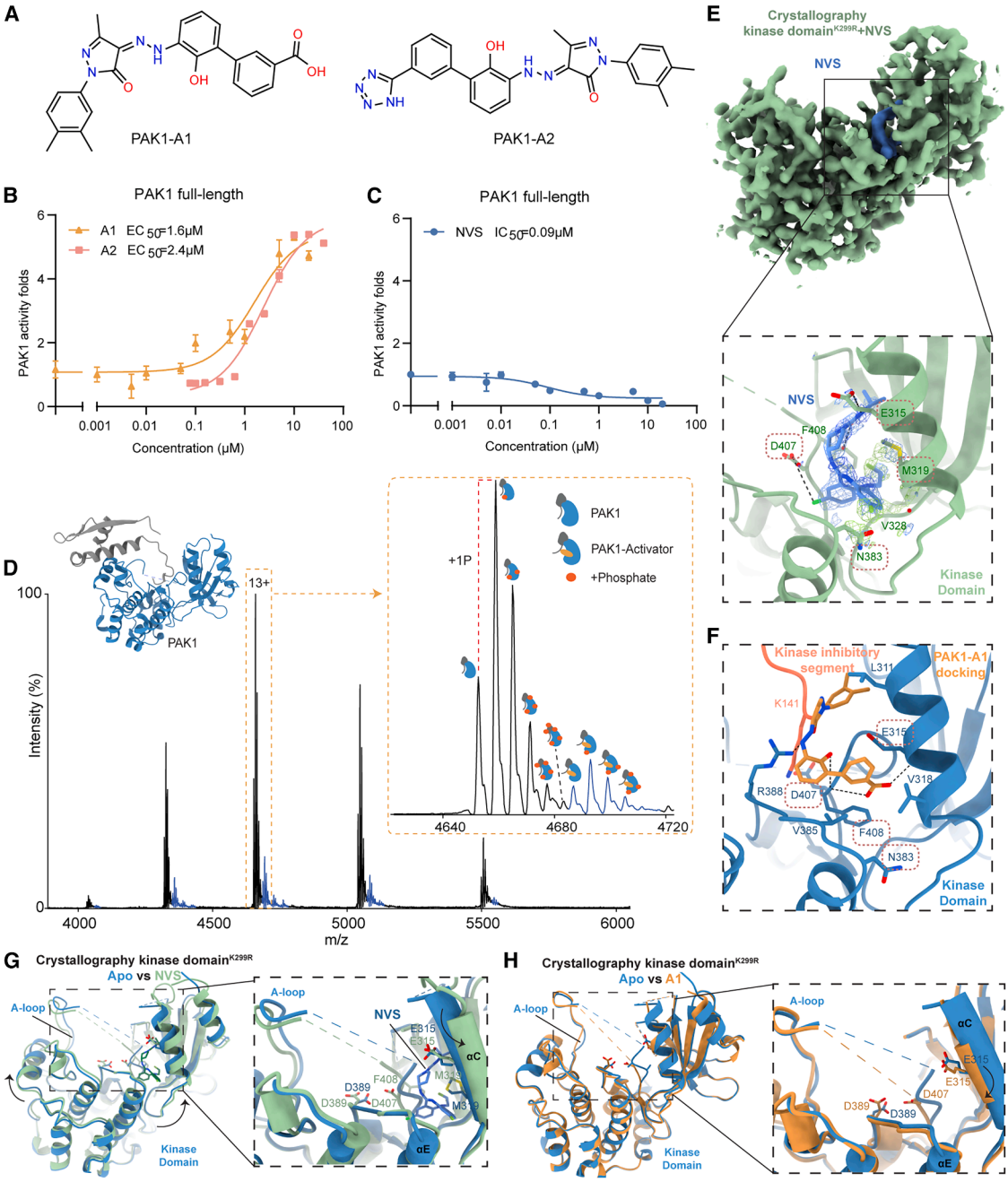

Figure 3. Targeting the autoinhibition-release site for the discovery of allosteric PAK1 activators

(A) Chemical structures of PAK1 activator PAK1-A1 and PAK1-A2.

(B and C) Dose-response curves for PAK1 activators (B) and a negative control NVS-PAK1-1 inhibitor (C) on PAK1 activity. Data are presented as mean ± SEM. $n = 3$.

(D) The native mass spectrum of PAK1-A1 binding to full-length PAK1 reveals peaks corresponding to the apo monomer of full-length PAK1 (and its various phosphorylated states [black]) and PAK1-A1 binding [blue]). PAK1-A1 was found binding to all forms of PAK1, including the non-phosphorylated and different phosphorylated states. The inset provides a zoomed-in view of the 13+ charge state, further illustrating the interaction between PAK1-A1 and PAK1.

(E) Co-crystal structure of the PAK1 kinase domain^{K299R} in complex with NVS-PAK1-1. Overview of the electron density map (top) and detailed interaction (bottom) of NVS-PAK1-1 with residues in the DFG-out binding site. NVS-PAK1-1 is shown in blue in the omit map and PAK1 kinase domain^{K299R} in green atomic structure.

(F) Predicted interaction of PAK-A1 with residues in the autoinhibition-release site. Residues involved in both NVS-PAK1-1 and PAK1-A1 binding sites are highlighted in red.

(G) Structural comparison of apo PAK1 kinase domain^{K299R} monomer A (dark blue) and co-crystal complex with NVS-PAK1-1 (green).

(H) Structural comparison of apo PAK1 kinase domain^{K299R} monomer A (dark blue) and structures soaked with PAK1-A1 (orange) to examine the conformational changes.

See also Figure S3.

To further define the binding mode of PAK1 activators, molecular docking using full-length PAK1 (PDB: 1F3M) predicted that PAK1-A1 binds within the DEK site via hydrophobic interactions with Lys141, Glu315, Arg388, and Phe408 (Figure 3F). PAK1-A2, an analog of PAK1-A1, exhibited a similar interaction within this allosteric DEK site, forming hydrogen bonds with Glu315, Arg388, and Asp407 (Figure S3G). The observed comparable binding modes may explain the nearly equivalent activation effects of both compounds on PAK1 (Figure 3B). Furthermore, structural and molecular dynamics analyses revealed partial overlap between the DEK binding site of PAK1-A1 and the DFG binding site of NVS-PAK1-1, involving Glu315, Asn383, Asp407, and Phe408 (Figures 3E, 3F, S3H, S5C, and S5D). Based on these observations, we propose a "piano-finger-like" mechanism, in which small-molecule engagement of shared regulatory residues drives distinct conformational outcomes, resulting in either kinase activation or inhibition. This finding highlights the dynamic nature of kinase regulation and provides insights into the design of modulators that can selectively target specific kinase states.

The PAK1 activator induces conformational changes in PAK1

To further investigate the interaction between small-molecule activators and PAK1, particularly at the autoinhibitory domain, we performed molecular dynamics simulations.[16] Three independent 400-ns simulations of the complex, as well as free-energy calculations using the molecular mechanics with generalized Born and surface area solvation (MM/GBSA) protocol (see STAR Methods), were performed. The estimated decomposition of free energy confirmed the localization of PAK1-A1 at the DEK autoinhibition-release site, where it interacts with the kinase inhibitory segment, αC helix, and DFG motif, as indicated by their close distance (Figures 4A and 4C). This is consistent with the binding site identified by PAL-MS (Figure 2E). Moreover, PAK1-A1 adopted an ensemble of conformations around the position originally occupied by the kinase inhibitory segment, which remains tightly bound to the DEK site (1.6 Å) (Figure S4A). In contrast, NVS-PAK1-1 binding to PAK1 exhibited a strong conformational interaction (~1 Å) with the DFG motif (Figures 4B, 4D, and S4B), consistent with its inhibitory effect on kinase activity. These findings support a mechanism in which PAK1-A1 counteracts autoinhibition and stabilizes the kinase in an active state. To experimentally evaluate the interaction between PAK1-A1 and full-length PAK1, we performed SPR analysis (Figures 4E and 4F). Full-length PAK1 was immobilized on a CM5 sensor chip, and compounds were injected at increasing concentrations in the running buffer. SPR analysis revealed dose-dependent binding of both PAK1-A1 and NVS-PAK1-1 to full-length PAK1. However, for small-molecule analytes, precise determination of equilibrium dissociation constants was challenging due to rapid association and dissociation kinetics and low response amplitudes inherent to these interactions. Therefore, binding affinities were estimated from steady-state analysis, indicating apparent K_D values in the low-micromolar range, broadly consistent with the corresponding EC_{50}/IC_{50} values obtained from kinase activity assays. To probe ligand-induced conformational changes in PAK1, Förster resonance energy transfer (FRET) experiments were employed (Figure S4C). The presence of NVS-PAK1-1 resulted in low FRET ratios (Figure 4I), suggesting an "open," inactive kinase conformation as expected for type III inhibitors. The amplitude of the FRET ratios remained constant through the concentrations (500 nM to 20 μM), despite a dose-dependent enhancement in the kinetics (Figure 4I). Conversely, PAK1-A1 induced a significant increase in FRET ratios (max. amplitude Δ13.8%), indicating that activator binding induces greater conformational changes than those of the inhibitor (Figure 4G).

To validate that these conformational changes and subsequent activation of PAK1 arise from ligand engagement at the DEK site, we generated PAK1 mutants targeting key ligand-interacting residues identified by PAL-MS and molecular dynamic simulations (Figures 2E and S6A). Mutations were introduced at Y131K, K141D, Y142K, E315A, V318D, N383L, V385D, and D407K to interrupt the ligand-protein interactions. Kinase activity assessment using ADP-Glo kinase assay showed that although some mutants, such as V318D and K141D, exhibited reduced activity relative to wild-type (WT), these differences were not statistically significant (Figure S4D). Mutants Y131K, K141D, and E315A were either not expressed or caused cell death in Chinese hamster ovary (CHO) cells. For the remaining constructs, baseline FRET measurements revealed altered FRET ratios relative to WT, suggesting mutation-induced conformational changes in PAK1 (Figure S4E). To evaluate ligand-induced dynamic FRET changes, we normalized the baseline FRET ratio to 1, allowing us to monitor relative changes upon compound addition. Upon treatment with PAK1-A1, mutants K141D, V318D, N383L, V385D, and D407K exhibited significant reductions in both FRET changes and ligand-binding kinetics, indicating that these residues are critical for PAK1-A1's binding to PAK1 (Figure 4H). The K141D mutation also attenuated the PAK1 conformational changes induced by NVS-PAK1-1 (Figure 4J), suggesting a crucial regulatory role for this residue in the autoinhibition mechanism and in the structural modulation of PAK1 by both activators and inhibitors.

Autoinhibited PAK1 has been traditionally considered dimeric based on early crystal structures.[16,41] However, subsequent biophysical measurements demonstrated that PAK1 exists predominantly as a monomer both before and after activation in solution.[42] Our gel filtration and mass photometry data revealed only minor peaks (2%) corresponding to dimeric PAK1 full-length proteins (Figures S4F and S4G). The active PAK1 kinase domain was also predominantly monomeric (Figure S4H), whereas the inactive kinase domain^{K299R} displayed both dimers and monomers (Figure S4I). Despite PAK1-A1 not having an activating effect on the PAK1 kinase domain^{K299R} (Figure 5F), the binding of activators still induced global conformational changes that caused dimer dissociation compared with the DMSO control (Figures S4J and S4L). On the other hand, treatment with NVS-PAK1-1 demonstrated no significant impact on dimerization (Figures S4K and S4L). These findings collectively demonstrate that PAK1 activators can induce global conformational rearrangements that facilitate the transition from an autoinhibited to an active monomeric state.

Mechanisms underpinning PAK1 activators

To further investigate the action mechanism of small-molecule activators, we analyzed native contact maps and observed

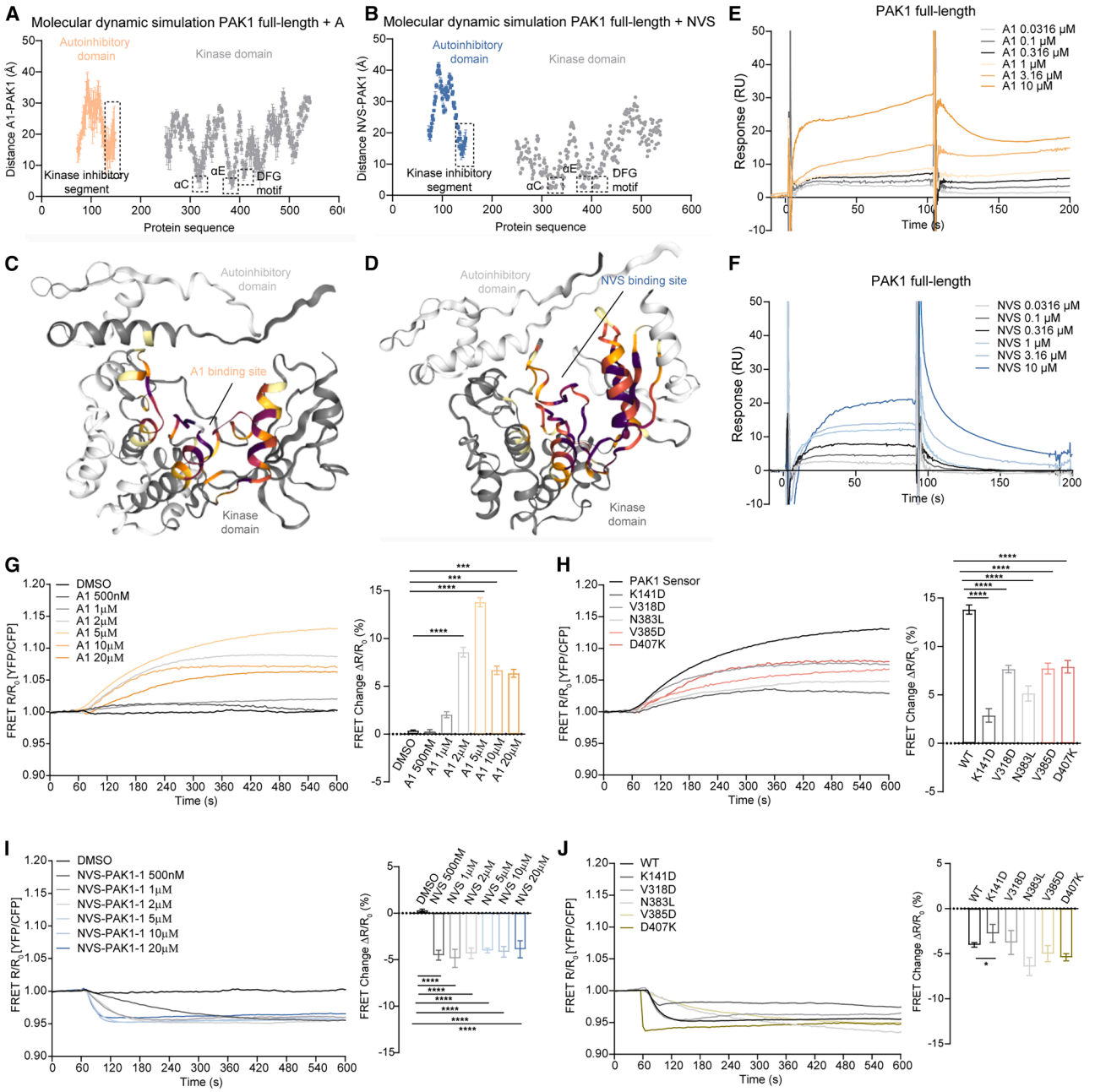

Figure 4. Activators and inhibitors induce distinct conformational changes in PAK1

(A and B) Geometrical calculations (top) reveal the distance between PAK-A1 (A) and NVS-PAK1-1 (B) and individual residues within PAK1.

(C and D) Key residues involved in ligand binding to full-length PAK1 are color-coded by their equilibrium distance to the ligand. Diagrams are presented.

(E and F) Representative surface plasmon resonance (SPR) sensorgrams from three independent experiments showing the binding of the small-molecule compounds PAK1-A1 (E) and NVS-PAK1-1 (F) to full-length PAK1 at the indicated concentrations. Binding was observed as concentration-dependent increases in resonance units (RUs) relative to baseline. Apparent binding affinities were estimated by steady-state (equilibrium) analysis and fall within the low-micromolar range (approximately 1–4 µM for PAK1-A1 and 0.2–0.8 µM for NVS-PAK1-1), as described in the STAR Methods.

(G and I) Small-molecule modulators induce PAK1 conformational changes. Left: normalized time courses of changes in FRET ratio of CHO cells expressing the PAK1-FRET biosensor following the treatment of PAK1-A1 (G) and NVS-PAK1-1 (I). Right: normalized, PAK1-A1 (G) and NVS-PAK1-1 (I) induced FRET ratio changes pooled from cells measured as on the left. FRET ratio changes are normalized to baseline (set to 0%).

(H and J) Mutagenesis supports the binding site of small-molecule modulators. Left: normalized time courses of changes in FRET ratio of CHO cells expressing wild-type (WT) PAK1-FRET biosensor and mutated biosensors, following the treatment of PAK1-A1 (5 µM) (H) and NVS-PAK1-1 (5 µM) (J). Right: normalized, PAK1-A1 and NVS-PAK1-1 induced FRET ratio changes pooled from cells measured as on the left. Data are presented as mean ± SEM. $n = 3$. ****$p < 0.0001$, ***$p < 0.001$, **$p < 0.01$, *$p < 0.05$, ns, not significantly different according to one-way ANOVA with Tukey's post hoc test.

See also Figure S4.

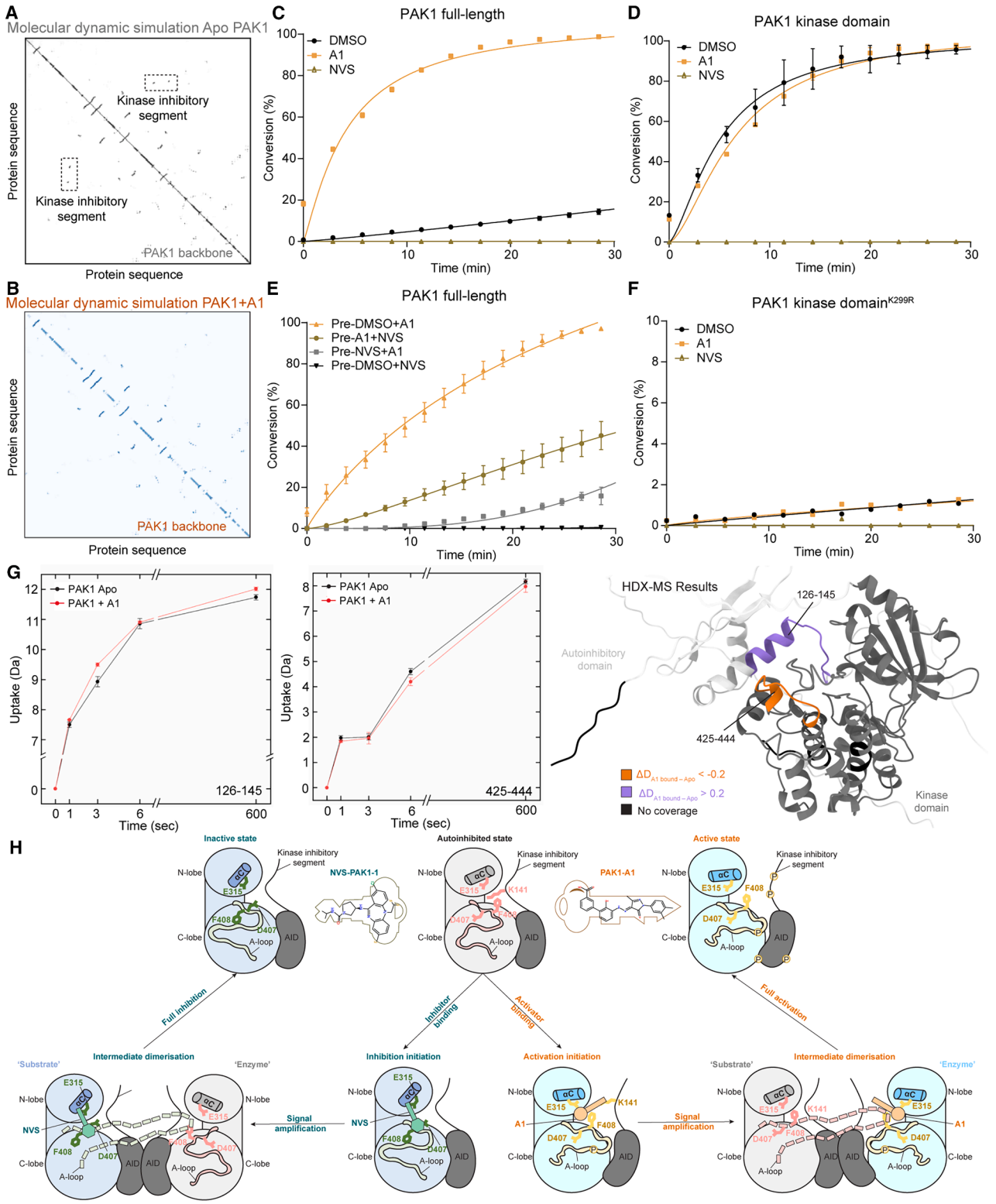

Figure 5. PAK1 activators interfere with the autoinhibition mechanism

(A and B) Contact map of apo full-length PAK1 (A) and PAK1-A1-bound PAK1 (B) shows the correlation of the PAK1-A1-derived kinase inhibitory segment shift from the ground autoinhibited state (apo).

(C) Kinetic study of PAK1-A1 (orange) and NVS-PAK1-1 (olive) on full-length PAK1 activity using RapidFire-MS.

(legend continued on next page)

significant conformational changes upon PAK1-A1 binding. In apo full-length PAK1, the kinase inhibitory segment remains closely associated with the PAK1 backbone. Upon PAK1-A1 binding, this kinase inhibitory segment is displaced away from the kinase domain, suggesting a disruption of autoinhibitory interactions that facilitates kinase activation (Figures 5A and 5B). This mechanism was also validated by kinase kinetic assays for PAK1-A1 and NVS-PAK1-1. In the autoinhibited full-length state and kinase-dead K299R mutant, PAK1 exhibited weak autophosphorylation activity (Figures 5C and 5F). In contrast, the isolated PAK1 kinase domain, which lacks interference from the autoinhibitory domain, remained constitutively active (Figure 5D). PAK1-A1 induced an activity profile comparable to that of the isolated kinase domain (Figures 5C and 5D). Consistent with previous findings using JB79 (Figure S1E), removal of the autoinhibitory domain abolished the activation effect of PAK1-A1, whereas NVS-PAK1-1 retained its inhibitory activity (Figures 5C and 5D). We next performed competitive binding assays to evaluate functional interplay between activators and inhibitors (Figure 5E). Addition of PAK1-A1 to NVS-PAK1-1-pretreated PAK1 initially preserved inhibition but subsequently restored kinase activity, whereas pre-incubation with PAK1-A1 followed by NVS-PAK1-1 slowed reaction kinetics. These results support the proposed piano-finger-like mechanism, in which activators and inhibitors modulate overlapping but distinct regulatory elements.

To further define the PAK1-A1 binding site and associated conformational changes, we employed HDX-MS (Figures 5G and S5B; Table S2). Significant differences in deuterium uptake were defined using a threshold of Da difference > 0.2 Da with p value < 0.05. PAK1-A1 incubation resulted in markedly reduced hydrogen-deuterium exchange within residues 425–444 of the kinase domain, indicating increased protection upon ligand binding and suggesting this region as a likely binding site of PAK1-A1. Within the αC helix of the DEK site, the reduction in hydrogen-deuterium exchange ($\Delta D \approx -0.19$ Da) fell just below the statistical threshold (Figure S5A). In contrast, significantly increased solvent exchange was observed in the autoinhibitory domain, particularly within the kinase inhibitory segment (residues 126–145), suggesting increased conformational flexibility or displacement in the region upon ligand binding (Figure 5G). These HDX-MS results aligned with the binding interface predicted by molecular dynamics simulations (Figure 4C) and partially overlapped with PAL-MS-identified sites. Differences likely reflect compound-specific binding modes, as HDX-MS was performed with PAK1-A1, whereas PAL-MS employed JB120. Collectively, these findings localize the activator binding site to the interface between the autoinhibitory and kinase domains (Figure S5B) and the observed changes within the kinase inhibitory segment support a mechanism in which PAK1-A1 activates PAK1 by displacing the kinase inhibitory segment and relieving autoinhibitory regulation.

Furthermore, we simulated ligand-induced dynamic conformational changes in PAK1 by monitoring distances and torsion angles within the DFG motif. In the ground and active state, PAK1 displayed DFG-in conformation with stable dihedral angles and a Glu315-Phe408 distance of 5Å (Figures S5E and S5H). In contrast, NVS-PAK1-1 stabilized an inactive DFG-out conformation, stabilized with a Glu315-Phe408 distance of 14 Å (Figures S5G and S5J).[43,44] Upon PAK1-A1 binding, we noticed a minor change in both the ψ angle of Phe408 and the Glu315-Phe408 distance. However, these changes quickly equilibrated to the baseline level (Figures S5F and S5I). Overall, these data indicate that PAK1 exists predominantly as a monomer in both autoinhibited and active states but may transiently populate intermediate dimeric conformations during activation process. We propose a "key-and-lock" model for PAK1 modulation (Figure 5H), in which the DFG motif functions as a lock cylinder. Activators occupy a sub-pocket that prevents re-entry of the kinase inhibitory segment into kinase domain, thereby unlocking kinase activity, whereas inhibitors engage an adjacent subpocket toward the β sheet of the small lobe to block ATP entry and lock the kinase in an inactive state. This model underscores the intricate process and precision required to target autoinhibitory regulation, as a slight mismatch in the "keys" can shift PAK1 toward activation or inhibition.

PAK1 activators induce PAK1 signaling *in vitro*

To assess the effects of PAK1-A1 on cellular PAK1 signaling, we performed phosphoproteomic profiling in serum-starved H9C2 cells treated with PAK1-A1 (10 μM) or DMSO for 1 h. Phosphosites showing >2-fold change relative to DMSO and adjusted $p < 0.05$ were considered significantly regulated. In total, 2,609 proteins and 8,864 phosphosites were quantified. Compared with DMSO, PAK1-A1 induced significant changes in 260 phosphosites, of which 80 were upregulated and 180 were

(D) Kinetic study of PAK1-A1 (orange) and NVS-PAK1-1 (olive) on PAK1 activity using the active kinase domain only.
(E) Competitive kinetic study of PAK1-A1 and NVS-PAK1-1 to assess their competitive binding to full-length PAK1.
(F) Kinetic study of PAK1-A1 (orange) and NVS-PAK1-1 (olive) on PAK1 activity using kinase domain with kinase-dead mutation K299R. Data are presented as mean ± SD. $n = 2$.
(G) Right: structural changes induced by PAK1-A1 as assessed by HDX-MS in full-length PAK1, highlighted on the AlphaFold2-predicted structural model of PAK1. Selection threshold for significant peptides: Da difference > 0.2, $p < 0.05$ (unpaired t test). The uptake was corrected for an average back exchange of 30%. $\Delta D_{A1\ bound\text{-}apo} < -0.2$ are highlighted in orange, and $\Delta D_{A1\ bound\text{-}apo} > 0.2$ are highlighted in purple. Left: selected peptide uptake from HDX-MS (peptides 126–145 from the autoinhibitory domain and 425–444 from the kinase domain) exhibiting significant differences in solvent exchange rates upon addition of PAK1-A1 (holo-PAK1, red) or in its absence (apo-PAK1, black). Four labeling time points were measured with up to five replicates acquired for each.
(H) Proposed conformation ensembles of PAK1 in the course of NVS-PAK1-1-induced inhibition and PAK1-A1-induced activation. In a ground state, PAK1 adopts the autoinhibited conformation. Upon activation, activator binds to the autoinhibition-release site to neutralize its autoinhibitory mechanism, leading to conformational changes. Transient dimers adopt an "enzyme-substrate complex" for signal amplification, followed by phosphorylation on multiple sites for full activation. Upon the binding of inhibitors, PAK1 adopts an inactive state due to the ATP entry block.
See also Figure S5.

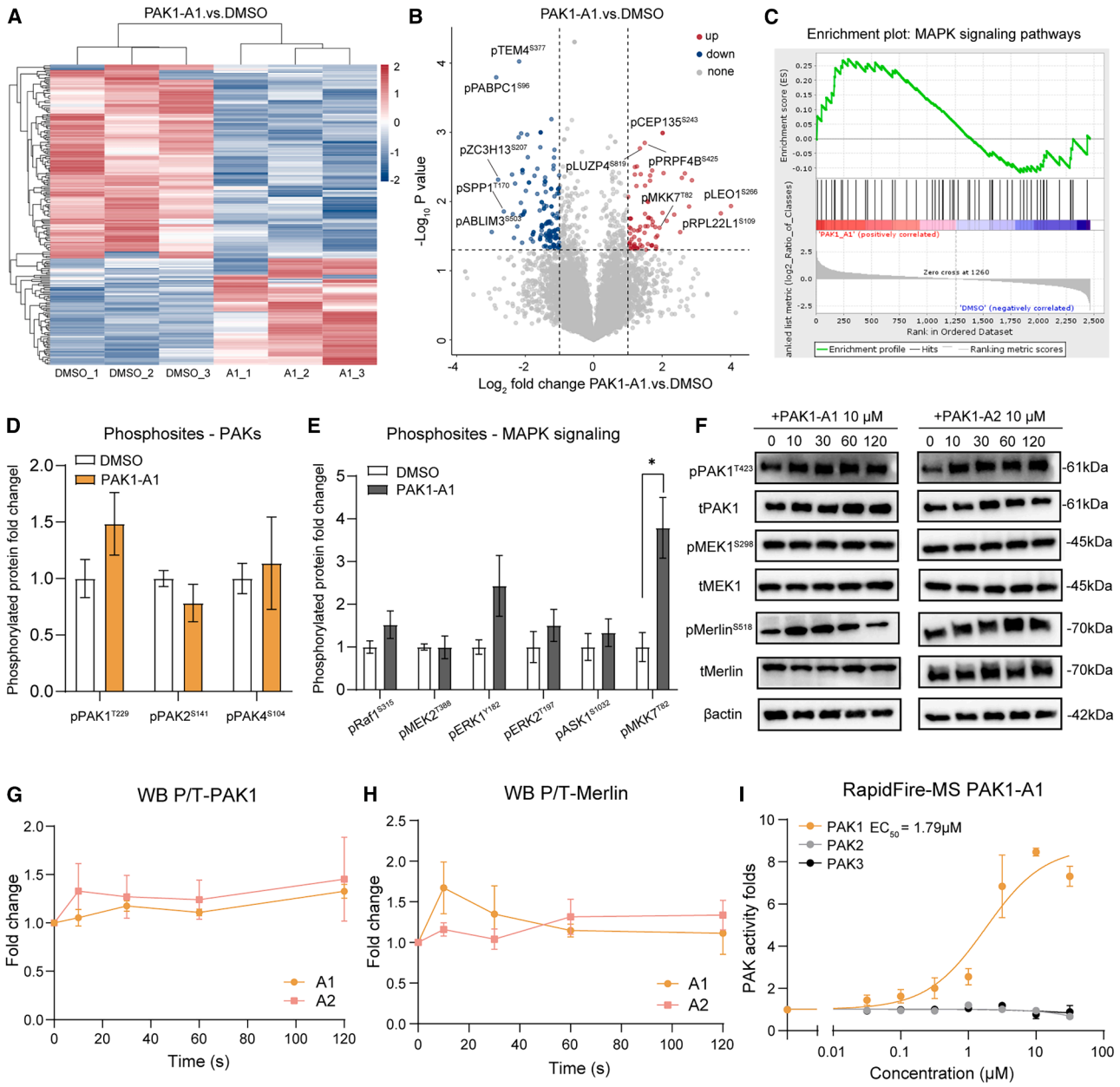

Figure 6. PAK1 activators stimulate PAK1-dependent signaling in cells

(A–E) Phosphoproteomic profiling of serum-starved H9C2 cells treated with PAK1-A1 (10 μM) or DMSO for 1 h (n = 3 independent experiments). Phosphosites exhibiting >2-fold change relative to DMSO with adjusted $p < 0.05$ were considered significantly regulated.

(A) Heatmap depicting significantly altered phosphosites following PAK1-A1 treatment. Red indicates upregulated and blue indicates downregulated phosphosites.

(B) Volcano plot showing significantly regulated phosphosites in PAK1-A1-treated cells compared with DMSO controls.

(C) Gene set enrichment analysis (KEGG) demonstrating enrichment of MAPK signaling. The upper panel shows the enrichment score (ES) curve, with larger absolute ES indicating stronger enrichment. Positive ES values indicate enrichment among upregulated proteins, whereas negative values indicate enrichment among downregulated proteins. The middle panel shows the positions of the function set members in the expression set list, with black vertical lines representing the members, and the lower panel shows $\log_2$ fold-change values.

(D) Phosphorylation changes in PAK1, PAK2, and PAK4 from the phosphoproteomic dataset.

(E) Phosphorylation changes in MAPK-pathway components, including RAF-MEK-ERK and MKK7 signaling nodes detected in the phosphoproteomic dataset ($p < 0.05$).

(F) Representative immunoblots of H9C2 cells treated with PAK1-A1 (10 μM) or PAK1-A2 (10 μM) for 0, 10, 30, 60, or 120 min.

(G and H) Quantification of phosphorylated Thr423-PAK1/total PAK1 (G) and phosphorylated Ser518-Merlin/total Merlin (H) in cells treated with PAK1-A1 or PAK1-A2 (n = 4 independent experiments).

(I) Dose-response curves demonstrating selective activation of full-length PAK1 relative to PAK2 and PAK3 by PAK1-A1 (n = 3). Data are mean ± SEM.

See also Figure S6.

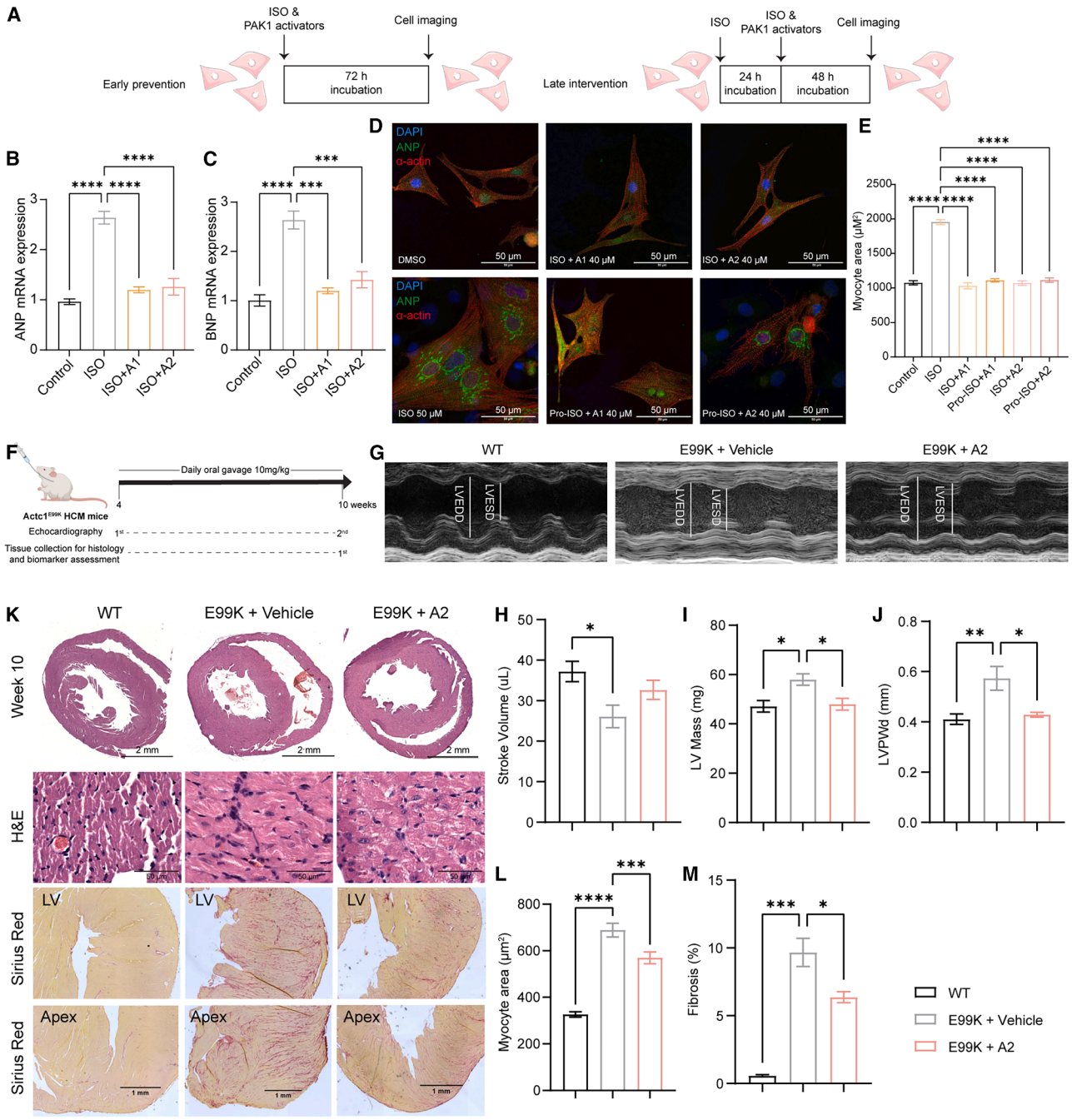

Figure 7. Therapeutic validation of PAK1 activators *in vitro* and *in vivo*

(A) An experimental scheme of cardiomyocyte treatment. To investigate early prevention, neonatal rat cardiomyocytes were subjected to treatment with isoprenaline (ISO, 50 μM), both with and without the presence of PAK1 activators (40 μM). To assess the effect of late intervention with PAK1 activators, PAK1-A1 and PAK1-A2 were introduced 24 h post-ISO treatment.

(B and C) Quantification of the mRNA expression levels of hypertrophic markers ANP (B) and BNP (C) measured by reverse transcription-quantitative polymerase chain reaction (RT-qPCR) after the treatment of 50 μM ISO with or without the presence of 40 μM PAK1 activators, PAK1-A1 and PAK1-A2. Data are presented as mean ± SEM. n = 3–4.

(D and E) Representative images (D) and quantification of cardiomyocyte area (E) evaluated after α-actin immunostaining. Scale bar, 50 μm. Data are presented as mean ± SEM. n = 200–300.

(F) An experimental scheme of mice oral gavage with PAK1 activator. Mice were gavaged daily with the dose of 10 mg/kg of PAK1-A2 and underwent echocardiographic analysis before being sacrificed.

(legend continued on next page)

downregulated (Figures 6A and 6B). Among PAK family proteins available in the panel, phosphorylation of PAK1-T229 increased by ~1.5-fold, consistent with enhanced PAK1 activation, whereas phosphorylation of PAK2-S141 and PAK4-S104 did not show appreciable changes (Figure 6D).

Several cytoskeletal and adhesion-associated phosphoproteins, including ARHGEF17 (TEM4), ABLIM3, and SPP1, together with RNA stability and methylation regulators PABPC1 and ZC3H13, were downregulated, suggesting suppression of structural remodeling and pro-fibrotic/inflammatory signaling. In contrast, we observed significant increases in phosphorylation of proteins involved in RNA processing, translation, and structural regulation, including LEO1, PRPF4B, RPL22L1, LUZP4, and CEP135, indicating enhanced gene-expression control and cytoskeletal support (Figure 6B). Although PAK1 is known to regulate cytoskeletal organization, adhesion, and cell-cycle control,[45,46] these specific phosphosites have not previously been linked to PAK1 signaling, highlighting the utility of PAK1-A1 for revealing potential new downstream pathways. Gene set enrichment analysis on the Kyoto Encyclopedia of Genes and Genomes (KEGG) pathway showed that mitogen-activated protein kinase (MAPK) signaling was prominently enriched following PAK1-A1 treatment (Figure 6C). Consistent with prior reports implicating PAK1 in MAPK regulation,[47,48] closer analysis of the phosphoproteomic data revealed increased phosphorylation within the rapidly accelerated fibrosarcoma kinase (RAF)-mitogen-activated protein kinase kinase (MEK)-extracellular signal-regulated kinase (ERK) cascade, with ERK1 phosphorylation increasing ~2.5-fold, although not reaching statistical significance. Notably, phosphorylation of mitogen-activated protein kinase kinase 7 (MKK7) was significantly increased by around 3.8-fold (Figure 6E). MKK7 is a kinase within the c-Jun N-terminal kinase (JNK) branch of the MAPK pathway and has been identified as a downstream effector of cardiac PAK1.[49] Previous studies indicate that PAK1 activation engages the MKK7-JNK stress-protective cascade, contributing to anti-hypertrophic effects in the heart.

To further characterize the temporal dynamics of PAK1 signaling, we examined time-dependent phosphorylation responses by western blotting in H9C2 cells treated with PAK1-A1 or PAK1-A2. Both compounds increased PAK1 phosphorylation over time, reaching ~1.5-fold elevation at 2 h (Figures 6F and 6G), consistent with the phosphoproteomic findings (Figure 6D). Although MEK1 has been reported to directly interact with PAK1, we did not detect substantial changes in MEK1 phosphorylation (Figure S6A). In contrast, phosphorylation of Merlin transiently increased after 10 min of PAK1-A1 treatment and then returned to baseline, while PAK1-A2 produced a modest increase at later time points (Figures 6F and 6H). These observations suggest that the activators may preferentially engage specific downstream branches of PAK1 signaling.

In addition, as group I PAKs (PAK1, PAK2, and PAK3) share high sequence similarity and a conserved activation mechanism, in which autoinhibited kinases are activated by Rac/Cdc42 binding, we next determined whether the observed signaling changes were specifically attributable to PAK1. To assess selectivity, we performed RapidFire-MS-based activity assays. Both PAK1-A1 and PAK1-A2 selectively activated PAK1 with no detectable activity toward PAK2 or PAK3 (Figures 6I and S6C). Selectivity was further validated using an independent radiometric assay measuring the transfer of ^{33}P-labeled phosphate to kinase substrates (Figure S6B). Although the PAK1 dose-response curve in this assay was less pronounced, likely reflecting differences in assay sensitivity, PAK1-A1 again selectively activated PAK1 without detectable effects on PAK2 or PAK3. Taken together, these findings indicate that PAK1-A1 functions as a selective PAK1 activator capable of engaging PAK1-dependent signaling pathways *in vitro*.

PAK1 activators provide cardioprotective effects

To evaluate the therapeutic potential of PAK1 activation, we examined the effects of PAK1 activators in both cellular and *in vivo* models of cardiac hypertrophy. Prolonged isoprenaline (ISO) treatment in mouse hearts can induce β-adrenergic stimulation and lead to adaptive responses, ultimately resulting in pathological cardiac hypertrophy.[50] In neonatal mouse cardiomyocytes, ISO treatment induced pathological hypertrophy, as evidenced by increased cellular size and expression of the hypertrophic markers atrial natriuretic peptide (ANP) and b-type natriuretic peptide (BNP). Co-treatment with either PAK1-A1 or PAK1-A2 significantly attenuated ISO-induced hypertrophy and reduced ANP and BNP expression (Figures 7A–7E), suggesting the potential of PAK1 activators for treating cellular hypertrophy. One of the clinical hallmarks in cardiovascular medicine is reversing pre-existing pathological cardiac hypertrophy. Unfortunately, due to its complex and challenging reversible nature, limited research has explored the development of small-molecule drugs that can reverse the pathological progression.[51] Notably, both compounds not only prevented hypertrophy but also regressed pre-existing cellular hypertrophy when administered 24 h after ISO treatment, as reflected by reduced cardiomyocyte size (Figures 7A, 7D, and 7E). Despite inducing a more moderate (~1.5-fold) increase in cellular PAK1 activity compared with their effect on the purified protein, both activators produced substantial anti-hypertrophic effects, suggesting that even a modest enhancement of PAK1 activity in cells may be sufficient to elicit meaningful cardioprotective effects.

To assess the therapeutic potential of PAK1 activation *in vivo*, it is worthwhile to evaluate the therapeutic effects of both the peptide and the small-molecule activators. To induce cardiac hypertrophy and cardiac remodeling *in vivo*, mice were treated with a cardiac stress inducer, angiotensin II (Ang II).[28]

(G–J) Representative images of echocardiography (G) and quantification of key parameters, including stroke volume (H), LV mass (I), and LV posterior wall (LVPW) thickness (J), for WT and HCM mice orally treated with vehicle and PAK1-A2 (10 mg/kg). $n = 5$.
(K) Representative histology staining images for HCM mice treated with vehicle and PAK1-A2.
(L and M) Quantification of myocyte cell size (L) and fibrosis area (M) evaluated after histology staining as shown in (K). Data are presented as mean ± SEM. $^{****}p < 0.0001$, $^{***}p < 0.001$, $^{**}p < 0.01$, $^{*}p < 0.05$, ns, not significantly different according to one-way ANOVA with Tukey's post hoc test.
See also Figure S7.

Co-administration of PAP showed a significant reduction of Ang II-induced hypertrophy as demonstrated by reduced fibrotic area, left ventricle (LV) mass, and wall thickness (Figures S7A and S7B). These protective effects of PAP were completely abolished in PAK1 knockout mice ($PAK1^{cko}$), in which chronic Ang II infusion led to exacerbated cardiac hypertrophy (Figures S7A and S7B). These results emphasize that the observed cardioprotective effects associated with PAP are specifically mediated by the activation of PAK1.

We next tested the small-molecule activator JB79 in a transverse aortic constriction (TAC) model of pressure overload-induced hypertrophy. Mice subjected to TAC and receiving a 2-week treatment of JB79 (10 mg/kg/day) via intraperitoneal injection exhibited significantly reduced cardiac hypertrophy and fibrosis compared with mice receiving vehicle treatment (Figures S7H–S7K). JB79 treatment also significantly reduced interventricular septum thickness at end-diastole (IVSd), left ventricular posterior wall thickness in diastole (LVPWd), and LV mass, while preserving ejection fraction and fractional shortening in TAC mice group (Figures S7D–S7G), which indicates that JB79-mediated activation of PAK1 can significantly alleviate TAC-induced cardiac hypertrophy.

In addition to acquired cardiac hypertrophy, we also evaluated the therapeutic effects of PAK1 activation in inherited HCM, a condition of great clinical relevance. Despite significant advances in understanding the genetic and molecular underpinnings of HCM, effective and specific treatments to prevent its progression remain limited. Here, we demonstrated that modulation of PAK1 activity by a PAK1 activator leads to notable enhancements in cardiac function within a transgenic HCM mouse model expressing the mutation $Actc1^{E99K}$.[52] Although JB79 and JB120 demonstrated efficacy in acquired hypertrophy models, their suboptimal physicochemical properties required intravenous administration, making them unsuitable for long-term treatment in this model. Therefore, we selected PAK1-A2 for chronic oral treatment in E99K HCM model due to its substantial effect in activating PAK1, improved solubility, minimal cytotoxicity, and favorable *in vivo* drug metabolism and pharmacokinetic profile. (Solubility—PAK1-A1: 18.83 mM in DMSO, while PAK1-A2 $\geq$ 77.17 mM in DMSO. The MTT assay, used to assess cell viability following pre-incubation with PAK1 activators, determined IC_{50} values of 221.4 μM for PAK1-A1 and 253 μM for PAK1-A2. Measurements in mouse liver microsomes found that PAK1-A2 exhibited an intrinsic clearance [CL_{int}] of 18.5 μL/min/mg and a half-life of 74.8 min).

Baseline analyses revealed that $Actc1^{E99K}$ mice exhibited early-onset cardiac hypertrophy by 4 weeks of age. Oral gavage treatment with PAK1-A2 (10 mg/kg/day) for 6 weeks significantly improved cardiac function in $Actc1^{E99K}$ mice, as demonstrated by increased stroke volume, ejection fraction, and cardiac output (Figures 7F–7H and S7N–S7P). Cardiac hypertrophy and structural remodeling were also markedly attenuated, with reductions in left ventricular mass, wall thickness, heart/body weight ratio, cardiomyocyte cross-sectional area, and interstitial fibrosis compared with vehicle-treated controls (Figures 7I–7M, S7L, S7M, and S7Q). These findings indicate that pharmacological activation of PAK1 can serve as a promising approach for managing hypertrophy and fibrosis progression in inherited HCM. Furthermore, the pathogenesis of HCM from a single mutation to comprehensive myocardial remodeling, responsible for the disease onset and progression, has not yet been well elucidated. Baseline results of the E99K HCM model demonstrated alterations in endoplasmic reticulum (ER) stress signaling, which is likely another important pathogenic element that underlies disease progression in HCM but is still poorly characterized. Under pathological conditions, ER protein homeostasis is disordered; prolonged activation of the unfolded protein response may initiate apoptotic cell death via the upregulation of C/EBP homologous protein (CHOP), which plays an important role in ER stress-induced apoptosis.[53] Mechanistically, PAK1-A2 treatment increased PAK1 phosphorylation in HCM hearts and alleviated ER stress. Specifically, levels of activating transcription factor 6 (ATF6) and CHOP were reduced, indicating suppression of ER stress-induced apoptotic signaling. In contrast, phosphorylation of inositol-requiring enzyme 1 (IRE-1) was enhanced, accompanied by increased activation of the transcription factor X-box binding protein 1 (XBP1), a key mediator of adaptive unfolded protein response signaling[54] (Figure S7R). These results uncover a previously unrecognized cardioprotective mechanism of PAK1 activation in HCM through alleviation of the ER stress response.

Collectively, our findings highlight the therapeutic potential of PAK1 activation, using both PAP and small-molecule activators, for treating cardiac hypertrophy and alleviating fibrosis.

Identification of PKA-activating peptides and small molecules

Our PAK1 activator discovery began with a peptide-guided screening strategy, where PAP was used to identify the autoinhibition-release site and guide subsequent small-molecule discovery. This hierarchical approach enabled the identification of improved PAK1 activators with therapeutic potential and may hold promise as a valuable strategy for the early-stage discovery of other autoinhibited kinase activators.

As a proof of concept, we applied this strategy to PKA, a critical regulator of cardiac function that is structurally mediated by an autoinhibitory regulatory subunit.[55,56] We designed three PKA-modulating peptides targeting the inhibitory segment and/or C-linker region of the RIα regulatory subunit to interfere with autoinhibitory regulation (Figure S6D). All three peptides increased cellular PKA activity, with the inhibitory-segment-derived peptide Pα2 producing the strongest activation (~1.5-fold) (Figure S6F). To confirm whether this activation was a direct effect, we utilized a RapidFire-MS assay (Figure S6E). The catalytic subunit alone showed constitutive activity, effectively phosphorylating its substrate without RIα's inhibitory effect. In the presence of the RIα regulatory subunit, PKA showed weak activity, which was restored by the positive control cyclic AMP (cAMP) or by treatment with all three peptides. Consistent with cellular data, Pα2 produced the strongest effect, increasing PKA activity by approximately 5-fold (Figure S6E). A control peptide derived from the RIIβ inhibitory segment activated cellular PKA but failed to overcome RIα-mediated inhibition *in vitro*, indicating regulatory-subunit specificity. We also tested a peptide derived from the inhibitory segment of the RIIβ regulatory subunit, which activated cellular PKA activity but failed to overcome

RIα's inhibition or restore catalytic subunit activity in the protein kinase assay (Figures S6E and S6F), suggesting the peptide's specificity.

Structural modeling suggested that PKA-activating peptides bind at the interface between the regulatory and catalytic subunits, interfering with autoinhibitory interactions rather than fully displacing the inhibitory segment (Figure S6D). Based on this identified autoinhibition-release site, we conducted a virtual screen of an FDA-approved drug library (1,615 ligands) and validated the top 20 hits on PKA activity using both a RapidFire-MS kinase assay and a FRET-based cellular PKA activity reporter (AKAR4).[57] Two compounds, Cpd1 (conivaptan,[58] EC_{50} = 1.53 μM) and Cpd2 (bemcentinib,[59] EC_{50} = 6.43 μM), showed dose-dependent activation of PKA activity in the presence of both the RIα regulatory subunit and the catalytic subunit (Figure S6G). Additionally, these compounds significantly increased cellular FRET ratios in AKAR4-transfected cells upon treatment (Figures S6K–S6M). Consistent with the PAK1 activation mechanism, without the inhibitory effect of the regulatory subunit, the PKA catalytic domain alone can almost fully phosphorylate the substrate peptide. Similar to PAK1 activators, the removal of the regulatory subunit nullified the activation effect of these PKA activators, indicating their ability to abolish the inhibitory influence of the regulatory subunit (Figure S6H). Docking analysis supported binding to an allosteric site at the interface between the RIα regulatory and catalytic subunits (Figures S6I and S6J). Together, these findings demonstrate that autoinhibition-release sites similar to that of PAK1 exist in other kinases and underscore the potential of this peptide-guided screening strategy in facilitating the initial discovery of other kinase activators.

DISCUSSION

In the context of kinase activator discovery, high-throughput screening remains the predominant method for identifying small molecules that modulate kinase activity. However, the hit rates observed for small-molecule activators identified through high-throughput screening tend to be significantly lower than those for identifying novel kinase inhibitors.[3] Consequently, employing rational targeted approaches and focused screening techniques for kinase activators would be more efficacious. Here, we developed a rationally designed strategy initiated by a bioactive guided peptide derived from the autoinhibitory domain. Using this peptide as a guide, we identified an unreported autoinhibition-release site, leading to the successful identification of a series of direct allosteric PAK1 activators with therapeutic potential for treating cardiac hypertrophy. This study highlights the potential of peptide-guided screening targeting autoinhibitory mechanisms as a rational strategy for discovering kinase activators, especially in the early stages of drug discovery.

Identification of potential peptides capable of regulating kinase activity requires an understanding of the conformational ensembles adopted by kinases, as these underlie diverse regulatory mechanisms.[60] In this study, we propose a model describing alternate conformational states of PAK1 during this regulatory process (Figure 5H). In the ground state, PAK1 is *cis*-autoinhibited, where the autoinhibitory domain obstructs the active site, preventing substrate binding. Binding of small-molecule activators to the autoinhibition-release site induces conformational changes, causing the withdrawal of the kinase inhibitory segment from the kinase domain cleft, releasing the activation loop, and enabling autophosphorylation of Thr423. Transient dimer interactions further facilitate *trans*-autophosphorylation. To sustain a prolonged active state, PAK1 undergoes subsequent phosphorylation at multiple serine and threonine sites within the autoinhibitory domain, including the kinase inhibitory segment, such as Ser21, Ser57, Ser144, Ser149, Ser198, and Thr212,[61,62] which have been shown to prevent re-dimerization and reversion to the inactive state.[16]

Beyond *cis*-autoinhibition, PAK1 activation involves a complex regulatory mechanism, as this is also regulated by a *trans*-autoinhibitory mechanism involving dimerization motifs that partially overlap with the autoinhibitory domain. The N-terminal p21-binding domain (PBD; aa 70–113), which contains the Cdc42/Rac-interactive binding (CRIB; aa 75–90) motif, contributes to inactive dimer formation by engaging paired β strands, while the kinase inhibitory segment interacts with the kinase domain.[16] Several residues are critical for this regulation and PAK1 activity. For instance, Leu107 reinforces the hydrophobic interface between the autoinhibitory domain and kinase domain, and the L107F mutation disrupts autoinhibition, leading to constitutive activation of PAK1.[16,63] Additionally, Tyr131, highlighted in our PAL-MS study, has been reported to contribute to PAK1 homodimerization, with the Y131C mutation enhancing phosphorylation and kinase activity.[64,65] Ser392 and Asp393 are important for the autophosphorylation in the activation loop within the dimeric arrangement of the kinase domain, as their substitution by Ala completely prevents Thr423 autophosphorylation and abolishes kinase activity.[41] It has been proposed that interactions with the kinase domain are sufficient to stabilize the autoinhibitory domain fold of PAK1. In turn, the autoinhibitory domain stabilizes the pairing of the dimerization segments. This folded domain functions as an inhibitory switch in three key ways: it positions the kinase inhibitory segment at the active site, prevents Cdc42 binding, and reinforces the dimer contact.[16] We believe that in addition to peptides derived from the kinase inhibitory segment, it may be worthwhile to explore peptides derived from the PBD region to enhance Cdc42 binding or disrupt homodimer formation for identifying other potential allosteric sites.

Autoinhibition plays critical roles in regulating kinase activity by maintaining enzymes in an inactive state until appropriate activating signals are present.[66] In some kinases, including PAK1, autoinhibition operates by suppressing catalytic activity and preventing essential autophosphorylation events. Binding of Rac/Cdc42 or stimulation by small-molecule PAK1 activators disrupts these inhibitory contacts, enabling autophosphorylation and full activation of PAK1. In other kinases, autoinhibition is mediated primarily through conformational restraints imposed by associated regulatory subunits rather than by blocking autophosphorylation. PI3Ks exemplify this mechanism; their autoinhibited state reflects restricted conformational flexibility driven by regulatory-subunit interactions. Activation, whether driven by receptor-tyrosine kinase signaling or by small-molecule activators such as compound 1938,[12] functions mainly by relieving these inhibitory interactions rather than promoting

autophosphorylation. Subsequent HDX-MS and crystallography studies revealed that 1938 activates PI3Kα by disrupting inhibitory contacts between the p85α regulatory and p110α catalytic domains. Similarly, AMPK activators, PT1 and OSU-53, also act through disrupting the interaction between the autoinhibitory domain and the catalytic domain.[67,68] Although these examples underscore the importance of autoinhibitory mechanisms in kinase regulation, systematic strategies for targeting such mechanisms remain underdeveloped. To explore the potential application of this rationally designed peptide-guided screening strategy beyond PAK1, we identified a PKA-activating peptide derived from the inhibitory segment of the RIα subunit. By targeting the autoinhibition-release site identified by this peptide, we discovered cAMP-independent PKA activators that can alleviate the inhibitory effect of the RIα subunit on the catalytic subunit, leading to PKA activation (Figure S6). Although these activators were less potent and effective than PAK1 activators, they provide proof of concept and a foundation for further refined screening and chemical optimization. Given the central role of PKA in numerous cellular processes, such activators may serve as valuable tools for probing PKA signaling dynamics in diverse physiological contexts. As many kinases contain intrinsic autoinhibitory elements, targeting autoinhibition-release sites may represent a potential strategy for the initial steps of the discovery of kinase activators as therapeutic drugs.[13,66,69,70] Moreover, given the distinct organizations of autoinhibited states among protein kinases,[71] the application of similar strategies to target other kinases with autoinhibitory mechanisms may hold promise for achieving enhanced specificity.

Our findings also demonstrate the therapeutic potential of kinase activation. Our previously published evidence demonstrated both genetic and pharmacological PAK1 activation as potential therapeutic treatments for cardiovascular diseases.[8,72] In this study, small-molecule PAK1 activators provided both prophylactic and therapeutic benefits in models of cardiovascular disease, including HCM (Figure 7). Currently, effective and specific treatments for slowing HCM progression remain limited, particularly for early-disease-stage interventions, when fibrosis first emerges and for patients with polygenic traits.[73–75] Sarcomere-targeting pharmacological interventions may also lack therapeutic benefits in these patients.[76] Earlier studies reported the effect of the sphingosine-1P receptor agonist FTY-720 in reducing the progression of established hypertrophy in HCM models.[22,77] The mechanism of reduced hypertrophy by FTY-720 may potentially be due to indirect PAK1 stimulation.[22] In our study, PAK1 activator treatment targets the early disease stage of HCM, characterized by increased LV wall thickness and the presence of fibrosis at the apex. Our treatment results demonstrated that PAK1 activators effectively decelerated the advancement of pre-existing hypertrophy and fibrosis. Additionally, in mice expressing the E99K mutation, which mimics a mutation observed in human HCM patients, PAK1 activators were able to reverse maladaptive ER stress signaling and reduce hypertrophic effects (Figure S7). The demonstrated therapeutic effects of enhancing PAK1 activity highlight the potential of kinase activators as promising therapeutic agents for the treatment of various diseases. Interestingly, PAK1-A2 displays a relatively slow metabolic rate, whereas we have identified other compounds that induce lower levels of PAK1 activation but undergo faster metabolism (data not shown). These compounds also demonstrated significant protective effects against cardiac hypertrophy, suggesting that even transient PAK1 activation may be sufficient to trigger endogenous cardioprotective signaling pathways, which differ from the sustained impact induced by constitutively activated mutations.[65,78] Further investigations into the time-dependent efficacy of PAK1 will be important for optimizing therapeutic strategies in both acute and chronic disease settings.

Taken together, our study demonstrates that targeting the autoinhibition-release site presents a viable approach for developing protein kinase activators. Given the conserved mechanism of autoinhibition among protein kinases,[71] the DEK analog pocket of other protein kinases may be identified by rationally designed specific peptide guides for the initial kinase activator screening process. The exploration of the action mechanism from peptide to small-molecule activators provides a potential conceptual framework for the development of innovative kinase-based therapies across a broad range of disease conditions.

Limitations of the study

One limitation of this study is the challenge of obtaining co-crystal structures of the activators bound to PAK1. This may be attributed to the dynamic or active conformation induced by the activators, as well as the disorder of the kinase inhibitory segment, which could hinder the formation of a fully enclosed binding pocket for PAK1 activators. Future efforts could explore stabilizing mutations within PAK1 to facilitate structural characterization of activator-bound states.

Although the compounds effectively activate PAK1, their potency and pharmacological properties can be further optimized, highlighting the need for additional SAR studies to identify higher-affinity compounds suitable for structural investigation. Peptides derived from other regions of the PAK1 autoinhibitory domain may also modulate kinase activity and could uncover additional allosteric binding pockets. In this study, while we evaluated the therapeutic potential of PAK1 activators in an early-disease-stage mouse model of HCM, future studies examining later-stage disease models and conducting comprehensive analyses assessing both on-target and off-target effects of these compounds would enhance clinical relevance.

In addition, although our approach may be applicable to other kinases with similar autoinhibitory mechanisms, as demonstrated by our proof-of-concept study in PKA, the structural diversity and distinct autoinhibitory mechanisms of kinases make rational peptide design inherently challenging. A detailed understanding of kinase structure and regulatory dynamics is therefore essential for developing effective peptide-guided screening strategies, and the applicability of this approach to other kinase families will require further experimental testing. In many cases, multiple or overlapping autoinhibitory interactions may exist, necessitating evaluation of several peptide variants derived from the AID before a functional candidate can be identified. Perhaps the rapid advancements in AI could aid in the identification of potential peptides.

RESOURCE AVAILABILITY

Lead contact

Requests for further information and resources should be directed to and will be fulfilled by the lead contact, Ming Lei (ming.lei@pharm.ox.ac.uk).

Materials availability

This study did not generate new unique reagents.

All chemical compounds generated in this study are available from the lead contact with a completed materials transfer agreement.

Data and code availability

The MS proteomics data have been deposited in the ProteomeXchange Consortium via the PRIDE partner repository under the dataset identifier ProteomeXchange: PXD074239.

Crystallography data have been deposited in the PDB under the following identifier: PDB: 28OQ (PAK1 kinase domain^{K299R} + NVS-PAK1-1 complex).

This paper does not report original code.

Any additional information required to reanalyze the data reported in this paper is available from the lead contact upon request.

ACKNOWLEDGMENTS

We thank the Evotec team (114 Innovation Drive, Milton Park, Abingdon, Oxfordshire OX14 4RZ, UK) for their support with medicinal chemistry and the PAL-MS study. We thank Dr. Andreas Griessner and Dr. Krapp Stephan from Proteros (Biostructures GmbH, Bunsenstraße 7 a, 82152 Planegg-Martinsried, Germany) for their help with PAK1 protein purification and crystallization. We thank Peter J. Harrison (The Rosalind Franklin Institute – Diamond Light Source, Harwell Science & Innovation Campus, Didcot, UK) for his assistance in attempting the cryo-EM experiments. We thank Prof. Maria Carla Parrini (Institut Curie, Centre de Recherche and INSERM U830, Paris F-75248, France) for providing the PAK1 FRET biosensor construct (Pakabi). We thank the Micron Advanced Bioimaging Unit at the Department of Biochemistry (University of Oxford) for providing support and assistance with imaging work. We thank the Advanced Research Computing (ARC) service at the University of Oxford for providing high-performance computing (HPC) resource for the data processing and analysis. We thank the OpenEye Free Academic Licensing Program for providing a free academic license for their chemistry toolkit. This work was supported by the British Heart Foundation, UK PG/22/11217 (M.L. and X.W.), PG/11/59/29004 (M.L.), PG/14/80/31106 (M.L.), PG/16/67/32340 (M.L.), PG/21/10512 (M.L.), and PG23/11479 (M.L., H.W., Y.-J.W., and X.W.); FS/PhD/20/29053 (M.L.); BHF Oxford Centre for Excellence (RE/18/3/34214); Medical Research Council UK G100647 (M.L.); Lab282 partnership award (OUI 13454-EVT07453, M.L. and J.S.H.B.); an EPSRC fellowship (EP/W522582/1) and the Eric and Wendy Schmidt AI in Science Postdoctoral Fellowship (C.O.); a MAESTRO grant from the National Science Center, Poland (2017/26/a/nz1/01098, M.N. and E.N.); National Institutes of Health grant P01 HL 062426 (R.J.S.); The National Natural Science Foundation of China (no. 82270334, X.T.; no. 82470323, X.T., no. 81700308, X.T., and no. 31871181, X.T. and M.L.); the Outstanding Youth Foundation of Sichuan Province, China (no. 20JDJQ0047, X.T.); and the Royal Society (no. URF\R1\211567, J.R.B.).

AUTHOR CONTRIBUTIONS

Conceptualization, M.L., J.S.H.B., and Y.H.; supervision, M.L. and J.S.H.B.; *in silico* screening, J.S.H.B., Y.H., and A.G.-R.; high-throughput physical screening, J.S.H.B., Y.H., and A.T.; co-crystallization, M.N. and E.N.; HDX-MS, D.P.O. and A.P.; molecular dynamics simulations, C.M.D., C.O., and D.A.N.; RapidFire-mass spectrometry methods and resources, C.J.S., A.T., G.B., E.S., J.S.H.B., and Y.H.; FRET experiment, M.Z., A.K., and Y.H.; native MS, J.R.B. and Y.W.; PAK1 protein purification, S.K. and S.M.; PAP in Ang II model, Y.K. and R.J.S.; JB79 in TAC model, X.T. and T.C.; PAK1-MEK1/Merlin and ER stress evaluation, X.W., W.H., and H.Z.; HCM *in vivo* evaluation, Y.H., Y.-J.W., and H.W.; compound synthesis, T.Y. and C.X.; mass photometry, P.K., S.T., and Y.H.; mutagenesis construct design, L.Y.; medicinal chemistry, G.C.C. and T.L.-H.; data interpretation and figure preparation, Y.H. and J.S.H.B.; writing, M.L., J.S.H.B., and Y.H.; review and editing, M.L., J.S.H.B., and Y.H., with assistance from all authors.

DECLARATION OF INTERESTS

A patent application, PCT/GB2025/051827, with relevance to this work has been filed by Oxford University Innovation Ltd covering "PAK1 and/or PAK2 activators and their use in the prevention and/or treatment of diseases or conditions" that lists M.L., J.S.H.B., and Y.H. as inventors.

STAR★METHODS

Detailed methods are provided in the online version of this paper and include the following:

- KEY RESOURCES TABLE
- EXPERIMENTAL MODEL AND STUDY PARTICIPANT DETAILS
  - Cell lines
  - Mice
- METHOD DETAILS
  - Peptide synthesis
  - AlphaFold2 modelling of protein-peptide pairs
  - In silico screening
  - Kinase activity screening with RapidFire- Mass Spectrometry
  - PAK1 kinase kinetic assay
  - PAK1 protein expression and purification
  - Structure-activity relationship and compound optimization
  - Photoaffinity labelling in PAK1 activator binding-site identification
  - LC-MS/MS Analysis of PAK1 and PAK1+Cdc42 Peptides
  - In vitro competitive photoaffinity labelling and MS-Analysis
  - Crystallization and X-Ray Data Collection for PAK1 autoinhibitory domain + kinase domain K299R structure
  - Crystallization of PAK1 kinase domain K299R–compound complexes
  - Structure Modelling and Refinement
  - Molecular dynamics simulations
  - Free energy calculations
  - Native mass spectrometry
  - Surface plasmon resonance (SPR)
  - HDX-MS Sample Preparation
  - HDX-MS Data Acquisition
  - HDX-MS Data Analysis
  - Generation of PAK1 biosensor
  - Cell culture
  - Transient transfection of WT, mutant PAK-FRET, and AKAR4 constructs in CHO cells
  - Single-cell Foerster Resonance Energy Transfer (FRET) imaging
  - Immunoprecipitation and ADP-Glo™ Kinase Assay
  - PAK1 dimerisation analysis by mass photometry
  - Phosphoproteomics
  - Analysis of phosphoproteomics data
  - Wheat germ agglutinin (WGA) staining
  - RNA isolation and RT-qPCR for ANP and BNP
  - Generation of PAK1^{CKO} Mice
  - Ang II-Induced Cardiac Hypertrophy and PAP treatment
  - Murine model of TAC and treatment of JB79
  - E99K hypertrophic cardiomyopathy (HCM) and PAK1-A2 treatment
  - Histological analysis
  - Echocardiography and Analysis
  - Immunoblot analyses
- QUANTIFICATION AND STATISTICAL ANALYSIS

SUPPLEMENTAL INFORMATION

Supplemental information can be found online at https://doi.org/10.1016/j.cell.2026.03.008.

Received: January 27, 2024
Revised: May 22, 2025
Accepted: March 6, 2026
Published: March 31, 2026

REFERENCES

1. Manning, G., Whyte, D.B., Martinez, R., Hunter, T., and Sudarsanam, S. (2002). The protein kinase complement of the human genome. Science *298*, 1912–1934. https://doi.org/10.1126/science.1075762.
2. Attwood, M.M., Fabbro, D., Sokolov, A.V., Knapp, S., and Schiöth, H.B. (2021). Trends in kinase drug discovery: targets, indications and inhibitor design. Nat. Rev. Drug Discov. *20*, 839–861. https://doi.org/10.1038/s41573-021-00252-y.
3. Zorn, J.A., and Wells, J.A. (2010). Turning enzymes ON with small molecules. Nat. Chem. Biol. *6*, 179–188. https://doi.org/10.1038/nchembio.318.
4. Cowan-Jacob, S.W., Jahnke, W., and Knapp, S. (2014). Novel approaches for targeting kinases: allosteric inhibition, allosteric activation and pseudokinases. Future Med. Chem. *6*, 541–561. https://doi.org/10.4155/fmc.13.216.
5. Fang, Z., Grütter, C., and Rauh, D. (2013). Strategies for the selective regulation of kinases with allosteric modulators: exploiting exclusive structural features. ACS Chem. Biol. *8*, 58–70. https://doi.org/10.1021/cb300663j.
6. Arter, C., Trask, L., Ward, S., Yeoh, S., and Bayliss, R. (2022). Structural features of the protein kinase domain and targeted binding by small-molecule inhibitors. J. Biol. Chem. *298*, 102247. https://doi.org/10.1016/j.jbc.2022.102247.
7. Simpson, G.L., Hughes, J.A., Washio, Y., and Bertrand, S.M. (2009). Direct small-molecule kinase activation: Novel approaches for a new era of drug discovery. Curr. Opin. Drug Discov. Devel. *12*, 585–596.
8. Wang, Y.W., Wang, S.Y., Lei, M., Boyett, M., Tsui, H., Liu, W., and Wang, X. (2018). The p21-activated kinase 1 (Pak1) signalling pathway in cardiac disease: from mechanistic study to therapeutic exploration. Br. J. Pharmacol. *175*, 1362–1374. https://doi.org/10.1111/bph.13872.
9. Gélinas, R., Mailleux, F., Dontaine, J., Bultot, L., Demeulder, B., Ginion, A., Daskalopoulos, E.P., Esfahani, H., Dubois-Deruy, E., Lauzier, B., et al. (2018). AMPK activation counteracts cardiac hypertrophy by reducing O-GlcNAcylation. Nat. Commun. *9*, 374. https://doi.org/10.1038/s41467-017-02795-4.
10. Cool, B., Zinker, B., Chiou, W., Kifle, L., Cao, N., Perham, M., Dickinson, R., Adler, A., Gagne, G., Iyengar, R., et al. (2006). Identification and characterization of a small molecule AMPK activator that treats key components of type 2 diabetes and the metabolic syndrome. Cell Metab. *3*, 403–416. https://doi.org/10.1016/j.cmet.2006.05.005.
11. Steinberg, G.R., and Carling, D. (2019). AMP-activated protein kinase: the current landscape for drug development. Nat. Rev. Drug Discov. *18*, 527–551. https://doi.org/10.1038/s41573-019-0019-2.
12. Gong, G.Q., Bilanges, B., Allsop, B., Masson, G.R., Roberton, V., Askwith, T., Oxenford, S., Madsen, R.R., Conduit, S.E., Bellini, D., et al. (2023). A small-molecule PI3Kalpha activator for cardioprotection and neuroregeneration. Nature *618*, 159–168. https://doi.org/10.1038/s41586-023-05972-2.
13. Astl, L., Tse, A., and Verkhivker, G.M. (2019). Interrogating Regulatory Mechanisms in Signaling Proteins by Allosteric Inhibitors and Activators: A Dynamic View Through the Lens of Residue Interaction Networks. Adv. Exp. Med. Biol. *1163*, 187–223. https://doi.org/10.1007/978-981-13-8719-7_9.
14. Mobitz, H., Jahnke, W., and Cowan-Jacob, S.W. (2017). Expanding the Opportunities for Modulating Kinase Targets with Allosteric Approaches. Curr. Top. Med. Chem. *17*, 59–70. https://doi.org/10.2174/1568026616666160719165314.
15. Xu, H., Wang, D., Ramponi, C., Wang, X., and Zhang, H. (2022). The P21-Activated Kinase 1 and 2 As Potential Therapeutic Targets for the Management of Cardiovascular Disease. Int. J. Drug Discov. Pharm. *1*, 5. https://doi.org/10.53941/ijddp.v1i1.179.
16. Lei, M., Lu, W., Meng, W., Parrini, M.C., Eck, M.J., Mayer, B.J., and Harrison, S.C. (2000). Structure of PAK1 in an autoinhibited conformation reveals a multistage activation switch. Cell *102*, 387–397. https://doi.org/10.1016/s0092-8674(00)00043-x.
17. Parrini, M.C., Lei, M., Harrison, S.C., and Mayer, B.J. (2002). Pak1 kinase homodimers are autoinhibited in trans and dissociated upon activation by Cdc42 and Rac1. Mol. Cell *9*, 73–83. https://doi.org/10.1016/S1097-2765(01)00428-2.
18. Ke, Y., Lei, M., Collins, T.P., Rakovic, S., Mattick, P.A.D., Yamasaki, M., Brodie, M.S., Terrar, D.A., and Solaro, R.J. (2007). Regulation of L-Type Calcium Channel and Delayed Rectifier Potassium Channel Activity by p21-Activated Kinase-1 in Guinea Pig Sinoatrial Node Pacemaker Cells. Circ. Res. *100*, 1317–1327. https://doi.org/10.1161/01.RES.0000266742.51389.a4.
19. Egom, E.E.A., Ke, Y., Solaro, R.J., and Lei, M. (2010). Cardioprotection in ischemia/reperfusion injury: Spotlight on sphingosine-1-phosphate and bradykinin signalling. Prog. Biophys. Mol. Biol. *103*, 142–147. https://doi.org/10.1016/j.pbiomolbio.2010.01.001.
20. Egom, E.E.A., Mohamed, T.M.A., Mamas, M.A., Shi, Y., Liu, W., Chirico, D., Stringer, S.E., Ke, Y., Shaheen, M., Wang, T., et al. (2011). Activation of Pak1/Akt/eNOS signaling following sphingosine-1-phosphate release as part of a mechanism protecting cardiomyocytes against ischemic cell injury. Am. J. Physiol., Heart Circ. Physiol. *301*, H1487–H1495. https://doi.org/10.1152/ajpheart.01003.2010.
21. DeSantiago, J., Bare, D.J., Ke, Y., Sheehan, K.A., Solaro, R.J., and Banach, K. (2013). Functional integrity of the T-tubular system in cardiomyocytes depends on p21-activated kinase 1. J. Mol. Cell. Cardiol. *60*, 121–128. https://doi.org/10.1016/j.yjmcc.2013.04.014.
22. Liu, W., Zi, M., Tsui, H., Chowdhury, S.K., Zeef, L., Meng, Q.-J., Travis, M., Prehar, S., Berry, A., Hanley, N.A., et al. (2013). A Novel Immunomodulator, FTY-720 Reverses Existing Cardiac Hypertrophy and Fibrosis From Pressure Overload by Targeting NFAT (Nuclear Factor of Activated T-cells) Signaling and Periostin. Circ., Heart Fail. *6*, 833–844. https://doi.org/10.1161/circheartfailure.112.000123.
23. Li, T., Liu, T., Wang, Y., Li, Y., Liu, L., Bae, J., He, Y., Luo, X., Liu, Z., Chen, T., et al. (2025). P21-Activated Kinase 2 as a Novel Target for Ventricular Tachyarrhythmias Associated with Cardiac Adrenergic Stress and Hypertrophy. Adv. Sci. (Weinh) *12*, e2411987. https://doi.org/10.1002/advs.202411987.
24. He, Y., and Lei, M. (2023). p21-Activated Kinases Present a New Drug Target for Hypertrophic Cardiomyopathy. Int. J. Drug Discov. Pharmacol. *2*, 79–86. https://doi.org/10.53941/ijddp.2023.100006.
25. Ke, Y., Wang, L., Pyle, W.G., de Tombe, P.P., and Solaro, R.J. (2004). Intracellular Localization and Functional Effects of P21-Activated Kinase-1 (Pak1) in Cardiac Myocytes. Circ. Res. *94*, 194–200. https://doi.org/10.1161/01.RES.0000111522.02730.56.
26. Tsui, H., Zi, M., Wang, S., Chowdhury, S.K., Prehar, S., Liang, Q., Cartwright, E.J., Lei, M., Liu, W., and Wang, X. (2015). Smad3 Couples Pak1 With the Antihypertrophic Pathway Through the E3 Ubiquitin Ligase, Fbxo32. Hypertension *66*, 1176–1183. https://doi.org/10.1161/hypertensionaha.115.06068.
27. Wang, Y., Tsui, H., Ke, Y., Shi, Y., Li, Y., Davies, L., Cartwright, E.J., Venetucci, L., Zhang, H., Terrar, D., et al. (2014). Pak1 is required to maintain ventricular Ca^{2+} homeostasis and electrophysiological stability through SERCA2a regulation in mice. Circ. Arrhythm. Electrophysiol. *7*, 938–948. https://doi.org/10.1161/CIRCEP.113.001198.
28. Wang, R., Wang, Y., Lin, W.K., Zhang, Y., Liu, W., Huang, K., Terrar, D.A., Solaro, R.J., Wang, X., Ke, Y., et al. (2014). Inhibition of angiotensin II-induced cardiac hypertrophy and associated ventricular arrhythmias by

a p21 activated kinase 1 bioactive peptide. PLoS One *9*, e101974. https://doi.org/10.1371/journal.pone.0101974.

29. Jumper, J., Evans, R., Pritzel, A., Green, T., Figurnov, M., Ronneberger, O., Tunyasuvunakool, K., Bates, R., Žídek, A., Potapenko, A., et al. (2021). Highly accurate protein structure prediction with AlphaFold. Nature *596*, 583–589. https://doi.org/10.1038/s41586-021-03819-2.

30. Trott, O., and Olson, A.J. (2010). AutoDock Vina: improving the speed and accuracy of docking with a new scoring function, efficient optimization, and multithreading. J. Comput. Chem. *31*, 455–461. https://doi.org/10.1002/jcc.21334.

31. Khan, M.T.H., Fuskevåg, O.M., and Sylte, I. (2009). Discovery of potent thermolysin inhibitors using structure based virtual screening and binding assays. J. Med. Chem. *52*, 48–61. https://doi.org/10.1021/jm8008019.

32. Leveridge, M., Collier, L., Edge, C., Hardwicke, P., Leavens, B., Ratcliffe, S., Rees, M., Stasi, L.P., Nadin, A., and Reith, A.D. (2016). A High-Throughput Screen to Identify LRRK2 Kinase Inhibitors for the Treatment of Parkinson's Disease Using RapidFire Mass Spectrometry. J. Biomol. Screen. *21*, 145–155. https://doi.org/10.1177/1087057115606707.

33. Hatanaka, Y., and Sadakane, Y. (2002). Photoaffinity labeling in drug discovery and developments: chemical gateway for entering proteomic frontier. Curr. Top. Med. Chem. *2*, 271–288. https://doi.org/10.2174/1568026023394182.

34. Lanyon-Hogg, T., Ritzefeld, M., Zhang, L., Andrei, S.A., Pogranyi, B., Mondal, M., Sefer, L., Johnston, C.D., Coupland, C.E., Greenfield, J.L., et al. (2021). Photochemical Probe Identification of a Small-Molecule Inhibitor Binding Site in Hedgehog Acyltransferase (HHAT). Angew. Chem. Weinheim Bergstr Ger. *133*, 13654–13659. https://doi.org/10.1002/ange.202014457.

35. McGann, M. (2011). FRED pose prediction and virtual screening accuracy. J. Chem. Inf. Model. *51*, 578–596. https://doi.org/10.1021/ci100436p.

36. Sterling, T., and Irwin, J.J. (2015). ZINC 15–Ligand Discovery for Everyone. J. Chem. Inf. Model. *55*, 2324–2337. https://doi.org/10.1021/acs.jcim.5b00559.

37. Kurokawa, T., Murata, S., Zheng, Y.W., Iwasaki, K., Kohno, K., Fukunaga, K., and Ohkohchi, N. (2015). The Eltrombopag antitumor effect on hepatocellular carcinoma. Int. J. Oncol. *47*, 1696–1702. https://doi.org/10.3892/ijo.2015.3180.

38. Siegal, D., Crowther, M., and Cuker, A. (2013). Thrombopoietin receptor agonists in primary immune thrombocytopenia. Semin. Hematol. *50*, S18–S21. https://doi.org/10.1053/j.seminhematol.2013.03.005.

39. Karpov, A.S., Amiri, P., Bellamacina, C., Bellance, M.H., Breitenstein, W., Daniel, D., Denay, R., Fabbro, D., Fernandez, C., Galuba, I., et al. (2015). Optimization of a Dibenzodiazepine Hit to a Potent and Selective Allosteric PAK1 Inhibitor. ACS Med. Chem. Lett. *6*, 776–781. https://doi.org/10.1021/acsmedchemlett.5b00102.

40. Oluwole, A.O., Hernández-Rocamora, V.M., Cao, Y., Li, X., Vollmer, W., Robinson, C.V., and Bolla, J.R. (2024). Real-Time Biosynthetic Reaction Monitoring Informs the Mechanism of Action of Antibiotics. J. Am. Chem. Soc. *146*, 7007–7017. https://doi.org/10.1021/jacs.4c00081.

41. Wang, J., Wu, J.W., and Wang, Z.X. (2011). Structural Insights into the Autoactivation Mechanism of p21-Activated Protein Kinase. Structure *19*, 1752–1761. https://doi.org/10.1016/j.str.2011.10.013.

42. Sorrell, F.J., Kilian, L.M., and Elkins, J.M. (2019). Solution structures and biophysical analysis of full-length group A PAKs reveal they are monomeric and auto-inhibited in cis. Biochem. J. *476*, 1037–1051. https://doi.org/10.1042/Bcj20180867.

43. Vijayan, R.S., He, P., Modi, V., Duong-Ly, K.C., Ma, H., Peterson, J.R., Dunbrack, R.L., Jr., and Levy, R.M. (2015). Conformational analysis of the DFG-out kinase motif and biochemical profiling of structurally validated type II inhibitors. J. Med. Chem. *58*, 466–479. https://doi.org/10.1021/jm501603h.

44. Shan, Y., Seeliger, M.A., Eastwood, M.P., Frank, F., Xu, H., Jensen, M.Ø., Dror, R.O., Kuriyan, J., and Shaw, D.E. (2009). A conserved protonation-dependent switch controls drug binding in the Abl kinase. Proc. Natl. Acad. Sci. USA *106*, 139–144. https://doi.org/10.1073/pnas.0811223106.

45. Sells, M.A., Knaus, U.G., Bagrodia, S., Ambrose, D.M., Bokoch, G.M., and Chernoff, J. (1997). Human p21-activated kinase (Pak1) regulates actin organization in mammalian cells. Curr. Biol. *7*, 202–210. https://doi.org/10.1016/s0960-9822(97)70091-5.

46. Delorme-Walker, V.D., Peterson, J.R., Chernoff, J., Waterman, C.M., Danuser, G., DerMardirossian, C., and Bokoch, G.M. (2011). Pak1 regulates focal adhesion strength, myosin IIA distribution, and actin dynamics to optimize cell migration. J. Cell Biol. *193*, 1289–1303. https://doi.org/10.1083/jcb.201010059.

47. Somanath, P.R., Vijai, J., Kichina, J.V., Byzova, T., and Kandel, E.S. (2009). The role of PAK-1 in activation of MAP kinase cascade and oncogenic transformation by Akt. Oncogene *28*, 2365–2369. https://doi.org/10.1038/onc.2009.114.

48. Coles, L.C., and Shaw, P.E. (2002). PAK1 primes MEK1 for phosphorylation by Raf-1 kinase during cross-cascade activation of the ERK pathway. Oncogene *21*, 2236–2244. https://doi.org/10.1038/sj.onc.1205302.

49. Liu, W., Zi, M., Naumann, R., Ulm, S., Jin, J.W., Taglieri, D.M., Prehar, S., Gui, J.H., Tsui, H., Xiao, R.P., et al. (2011). Pak1 as a Novel Therapeutic Target for Antihypertrophic Treatment in the Heart. Circulation *124*, 2702–2715. https://doi.org/10.1161/Circulationaha.111.048785.

50. Ke, Y., Lei, M., Wang, X., and Solaro, R.J. (2012). Novel roles of PAK1 in the heart. Cell. Logist. *2*, 89–94. https://doi.org/10.4161/cl.21497.

51. McKinsey, T.A., and Kass, D.A. (2007). Small-molecule therapies for cardiac hypertrophy: moving beneath the cell surface. Nat. Rev. Drug Discov. *6*, 617–635. https://doi.org/10.1038/nrd2193.

52. Song, W., Dyer, E., Stuckey, D.J., Copeland, O., Leung, M.C., Bayliss, C., Messer, A., Wilkinson, R., Tremoleda, J.L., Schneider, M.D., et al. (2011). Molecular mechanism of the E99K mutation in cardiac actin (ACTC Gene) that causes apical hypertrophy in man and mouse. J. Biol. Chem. *286*, 27582–27593. https://doi.org/10.1074/jbc.M111.252320.

53. Kim, I., Xu, W., and Reed, J.C. (2008). Cell death and endoplasmic reticulum stress: disease relevance and therapeutic opportunities. Nat. Rev. Drug Discov. *7*, 1013–1030. https://doi.org/10.1038/nrd2755.

54. Thuerauf, D.J., Marcinko, M., Gude, N., Rubio, M., Sussman, M.A., and Glembotski, C.C. (2006). Activation of the unfolded protein response in infarcted mouse heart and hypoxic cultured cardiac myocytes. Circ. Res. *99*, 275–282. https://doi.org/10.1161/01.Res.0000233317.70421.03.

55. Liu, Y., Chen, J., Fontes, S.K., Bautista, E.N., and Cheng, Z. (2022). Physiological and pathological roles of protein kinase A in the heart. Cardiovasc. Res. *118*, 386–398. https://doi.org/10.1093/cvr/cvab008.

56. Kim, C., Cheng, C.Y., Saldanha, S.A., and Taylor, S.S. (2007). PKA-I holoenzyme structure reveals a mechanism for cAMP-dependent activation. Cell *130*, 1032–1043. https://doi.org/10.1016/j.cell.2007.07.018.

57. Depry, C., Allen, M.D., and Zhang, J. (2011). Visualization of PKA activity in plasma membrane microdomains. Mol. Biosyst. *7*, 52–58. https://doi.org/10.1039/c0mb00079e.

58. Wada, K., Fujimori, A., Matsukawa, U., Arai, Y., Sudoh, K., Yatsu, T., Sasamata, M., and Miyata, K. (2005). Intravenous administration of conivaptan hydrochloride improves cardiac hemodynamics in rats with myocardial infarction-induced congestive heart failure. Eur. J. Pharmacol. *507*, 145–151. https://doi.org/10.1016/j.ejphar.2004.11.022.

59. Sensi, M., Catani, M., Castellano, G., Nicolini, G., Alciato, F., Tragni, G., De Santis, G., Bersani, I., Avanzi, G., Tomassetti, A., et al. (2011). Human cutaneous melanomas lacking MITF and melanocyte differentiation antigens express a functional Axl receptor kinase. J. Investig. Dermatol. *131*, 2448–2457. https://doi.org/10.1038/jid.2011.218.

60. Xie, T., Saleh, T., Rossi, P., and Kalodimos, C.G. (2020). Conformational states dynamically populated by a kinase determine its function. Science *370*, eabc2754. https://doi.org/10.1126/science.abc2754.

61. Sheehan, K.A., Ke, Y., and Solaro, R.J. (2007). p21-Activated kinase-1 and its role in integrated regulation of cardiac contractility. Am. J. Physiol. Regul. Integr. Comp. Physiol. *293*, R963–R973. https://doi.org/10.1152/ajpregu.00253.2007.

62. Manser, E., Huang, H.Y., Loo, T.H., Chen, X.Q., Dong, J.M., Leung, T., and Lim, L. (1997). Expression of constitutively active alpha-PAK reveals effects of the kinase on actin and focal complexes. Mol. Cell. Biol. *17*, 1129–1143. https://doi.org/10.1128/MCB.17.3.1129.

63. Frost, J.A., Khokhlatchev, A., Stippec, S., White, M.A., and Cobb, M.H. (1998). Differential effects of PAK1-activating mutations reveal activity-dependent and -independent effects on cytoskeletal regulation. J. Biol. Chem. *273*, 28191–28198. https://doi.org/10.1074/jbc.273.43.28191.

64. Renkema, G.H., Pulkkinen, K., and Saksela, K. (2002). Cdc42/Rac1-mediated activation primes PAK2 for superactivation by tyrosine phosphorylation. Mol. Cell. Biol. *22*, 6719–6725. https://doi.org/10.1128/MCB.22.19.6719-6725.2002.

65. Harms, F.L., Kloth, K., Bley, A., Denecke, J., Santer, R., Lessel, D., Hempel, M., and Kutsche, K. (2018). Activating Mutations in PAK1, Encoding p21-Activated Kinase 1, Cause a Neurodevelopmental Disorder. Am. J. Hum. Genet. *103*, 579–591. https://doi.org/10.1016/j.ajhg.2018.09.005.

66. Bayliss, R., Haq, T., and Yeoh, S. (2015). The Ys and wherefores of protein kinase autoinhibition. Biochim. Biophys. Acta *1854*, 1586–1594. https://doi.org/10.1016/j.bbapap.2015.04.025.

67. Pang, T., Zhang, Z.S., Gu, M., Qiu, B.Y., Yu, L.F., Cao, P.R., Shao, W., Su, M.B., Li, J.Y., Nan, F.J., et al. (2008). Small molecule antagonizes autoinhibition and activates AMP-activated protein kinase in cells. J. Biol. Chem. *283*, 16051–16060. https://doi.org/10.1074/jbc.M710114200.

68. Lee, K.H., Hsu, E.C., Guh, J.H., Yang, H.C., Wang, D.S., Kulp, S.K., Shapiro, C.L., and Chen, C.S. (2011). Targeting Energy Metabolic and Oncogenic Signaling Pathways in Triple-negative Breast Cancer by a Novel Adenosine Monophosphate-activated Protein Kinase (AMPK) Activator. J. Biol. Chem. *286*, 39247–39258. https://doi.org/10.1074/jbc.M111.264598.

69. Reinhardt, R., Hirzel, K., Link, G., Eisler, S.A., Hägele, T., Parson, M.A.H., Burke, J.E., Hausser, A., and Leonard, T.A. (2023). PKD autoinhibition in trans regulates activation loop autophosphorylation in cis. Proc. Natl. Acad. Sci. USA *120*, e2212909120. https://doi.org/10.1073/pnas.2212909120.

70. Zhang, M.Z., Jang, H., and Nussinov, R. (2020). Structural Features that Distinguish Inactive and Active PI3K Lipid Kinases. J. Mol. Biol. *432*, 5849–5859. https://doi.org/10.1016/j.jmb.2020.09.002.

71. Nussinov, R., Zhang, M., Tsai, C.J., Liao, T.J., Fushman, D., and Jang, H. (2018). Autoinhibition in Ras effectors Raf, PI3Kα, and RASSF5: a comprehensive review underscoring the challenges in pharmacological intervention. Biophys. Rev. *10*, 1263–1282. https://doi.org/10.1007/s12551-018-0461-0.

72. He, Y., Grassam-Rowe, A., Lei, M., and Bae, J.S.H. (2023). Targeting p21-activated kinase 1 for development of a novel anti-arrhythmic drug class. Philos. Trans. R. Soc. Lond. B Biol. Sci. *378*, 20220285. https://doi.org/10.1098/rstb.2022.0285.

73. Walsh, R., Thomson, K.L., Ware, J.S., Funke, B.H., Woodley, J., McGuire, K.J., Mazzarotto, F., Blair, E., Seller, A., Taylor, J.C., et al. (2017). Reassessment of Mendelian gene pathogenicity using 7,855 cardiomyopathy cases and 60,706 reference samples. Genet. Med. *19*, 192–203. https://doi.org/10.1038/gim.2016.90.

74. Maron, B.J., Desai, M.Y., Nishimura, R.A., Spirito, P., Rakowski, H., Towbin, J.A., Rowin, E.J., Maron, M.S., and Sherrid, M.V. (2022). Diagnosis and Evaluation of Hypertrophic Cardiomyopathy: JACC State-of-the-Art Review. J. Am. Coll. Cardiol. *79*, 372–389. https://doi.org/10.1016/j.jacc.2021.12.002.

75. Ho, C.Y., Day, S.M., Axelsson, A., Russell, M.W., Zahka, K., Lever, H.M., Pereira, A.C., Colan, S.D., Margossian, R., Murphy, A.M., et al. (2021). Valsartan in early-stage hypertrophic cardiomyopathy: a randomized phase 2 trial. Nat. Med. *27*, 1818–1824. https://doi.org/10.1038/s41591-021-01505-4.

76. Ranjbarvaziri, S., Kooiker, K.B., Ellenberger, M., Fajardo, G., Zhao, M., Vander Roest, A.S., Woldeyes, R.A., Koyano, T.T., Fong, R., Ma, N., et al. (2021). Altered Cardiac Energetics and Mitochondrial Dysfunction in Hypertrophic Cardiomyopathy. Circulation *144*, 1714–1731. https://doi.org/10.1161/CIRCULATIONAHA.121.053575.

77. Ryba, D.M., Warren, C.M., Karam, C.N., Davis, R.T., 3rd, Chowdhury, S.A.K., Alvarez, M.G., McCann, M., Liew, C.W., Wieczorek, D.F., Varga, P., et al. (2019). Sphingosine-1-Phosphate Receptor Modulator, FTY720, Improves Diastolic Dysfunction and Partially Reverses Atrial Remodeling in a Tm-E180G Mouse Model Linked to Hypertrophic Cardiomyopathy. Circ., Heart Fail. *12*, e005835. https://doi.org/10.1161/CIRCHEARTFAILURE.118.005835.

78. Lei, M., Robinson, M.A., and Harrison, S.C. (2005). The active conformation of the PAK1 kinase domain. Structure *13*, 769–778. https://doi.org/10.1016/j.str.2005.03.007.

79. Parrini, M.C., Camonis, J., Matsuda, M., and de Gunzburg, J. (2009). Dissecting Activation of the PAK1 Kinase at Protrusions in Living Cells. J. Biol. Chem. *284*, 24133–24143. https://doi.org/10.1074/jbc.M109.015271.

80. Pettersen, E.F., Goddard, T.D., Huang, C.C., Meng, E.C., Couch, G.S., Croll, T.I., Morris, J.H., and Ferrin, T.E. (2021). UCSF ChimeraX: Structure visualization for researchers, educators, and developers. Protein Sci. *30*, 70–82. https://doi.org/10.1002/pro.3943.

81. Neves, M.A.C., Totrov, M., and Abagyan, R. (2012). Docking and scoring with ICM: the benchmarking results and strategies for improvement. J. Comput. Aid. Mol. Des. *26*, 675–686. https://doi.org/10.1007/s10822-012-9547-0.

82. Knox, C., Wilson, M., Klinger, C.M., Franklin, M., Oler, E., Wilson, A., Pon, A., Cox, J., Chin, N.E.L., Strawbridge, S.A., et al. (2024). DrugBank 6.0: the DrugBank Knowledgebase for 2024. Nucleic Acids Res. *52*, D1265–D1275. https://doi.org/10.1093/nar/gkad976.

83. Hawkins, P.C.D., Skillman, A.G., Warren, G.L., Ellingson, B.A., and Stahl, M.T. (2010). Conformer generation with OMEGA: algorithm and validation using high quality structures from the Protein Databank and Cambridge Structural Database. J. Chem. Inf. Model. *50*, 572–584. https://doi.org/10.1021/ci100031x.

84. McGann, M. (2012). FRED and HYBRID docking performance on standardized datasets. J. Comput. Aid. Mol. Des. *26*, 897–906. https://doi.org/10.1007/s10822-012-9584-8.

85. Lowe, D.M., Gee, M., Haslam, C., Leavens, B., Christodoulou, E., Hissey, P., Hardwicke, P., Argyrou, A., Webster, S.P., Mole, D.J., et al. (2014). Lead discovery for human kynurenine 3-monooxygenase by high-throughput RapidFire mass spectrometry. J. Biomol. Screen. *19*, 508–515. https://doi.org/10.1177/1087057113518069.

86. Robinette, D., Neamati, N., Tomer, K.B., and Borchers, C.H. (2006). Photoaffinity labeling combined with mass spectrometric approaches as a tool for structural proteomics. Expert Rev. Proteom. *3*, 399–408. https://doi.org/10.1586/14789450.3.4.399.

87. Gao, J., Mfuh, A., Amako, Y., and Woo, C.M. (2018). Small Molecule Interactome Mapping by Photoaffinity Labeling Reveals Binding Site Hotspots for the NSAIDs. J. Am. Chem. Soc. *140*, 4259–4268. https://doi.org/10.1021/jacs.7b11639.

88. Krug, M., Weiss, M.S., Heinemann, U., and Mueller, U. (2012). XDSAPP: a graphical user interface for the convenient processing of diffraction data using XDS. J. Appl. Crystallogr. *45*, 568–572. https://doi.org/10.1107/S0021889812011715.

89. Mccoy, A.J., Grosse-Kunstleve, R.W., Adams, P.D., Winn, M.D., Storoni, L.C., and Read, R.J. (2007). Phaser crystallographic software. J. Appl. Crystallogr. *40*, 658–674. https://doi.org/10.1107/S0021889807021206.

90. Adams, P.D., Afonine, P.V., Bunkóczi, G., Chen, V.B., Davis, I.W., Echols, N., Headd, J.J., Hung, L.W., Kapral, G.J., Grosse-Kunstleve, R.W., et al. (2010). PHENIX: a comprehensive Python-based system for macromolecular structure solution. Acta Crystallogr. D Biol. Crystallogr. *66*, 213–221. https://doi.org/10.1107/S0907444909052925.

91. Emsley, P., Lohkamp, B., Scott, W.G., and Cowtan, K. (2010). Features and development of Coot. Acta Crystallogr. D Biol. Crystallogr. *66*, 486–501. https://doi.org/10.1107/S0907444910007493.

92. Halgren, T.A. (1996). Merck molecular force field. I. Basis, form, scope, parameterization, and performance of MMFF94. J. Comput. Chem. *17*, 490–519. https://doi.org/10.1002/(Sici)1096-987x(199604)17:5/6<490::Aid-Jcc1>3.0.Co;2-P.

93. Hanwell, M.D., Curtis, D.E., Lonie, D.C., Vandermeersch, T., Zurek, E., and Hutchison, G.R. (2012). Avogadro: an advanced semantic chemical editor, visualization, and analysis platform. J. Cheminform. *4*, 17. https://doi.org/10.1186/1758-2946-4-17.

94. Schreiner, E., Trabuco, L.G., Freddolino, P.L., and Schulten, K. (2011). Stereochemical errors and their implications for molecular dynamics simulations. BMC Bioinformatics *12*, 190. https://doi.org/10.1186/1471-2105-12-190.

95. Humphrey, W., Dalke, A., and Schulten, K. (1996). VMD: visual molecular dynamics. J. Mol. Graph. *14*, 33–38. https://doi.org/10.1016/0263-7855(96)00018-5.

96. Gordon, J.C., Myers, J.B., Folta, T., Shoja, V., Heath, L.S., and Onufriev, A. (2005). H++: a server for estimating pKas and adding missing hydrogens to macromolecules. Nucleic Acids Res. *33*, W368–W371. https://doi.org/10.1093/nar/gki464.

97. Machado, M.R., and Pantano, S. (2020). Split the Charge Difference in Two! A Rule of Thumb for Adding Proper Amounts of Ions in MD Simulations. J. Chem. Theor. Comput. *16*, 1367–1372. https://doi.org/10.1021/acs.jctc.9b00953.

98. Maier, J.A., Martinez, C., Kasavajhala, K., Wickstrom, L., Hauser, K.E., and Simmerling, C. (2015). ff14SB: Improving the Accuracy of Protein Side Chain and Backbone Parameters from ff99SB. J. Chem. Theor. Comput. *11*, 3696–3713. https://doi.org/10.1021/acs.jctc.5b00255.

99. Jorgensen, W.L., Chandrasekhar, J., Madura, J.D., Impey, R.W., and Klein, M.L. (1983). Comparison of Simple Potential Functions for Simulating Liquid Water. J. Chem. Phys. *79*, 926–935. https://doi.org/10.1063/1.445869.

100. Wang, J., Wolf, R.M., Caldwell, J.W., Kollman, P.A., and Case, D.A. (2004). Development and testing of a general amber force field. J. Comput. Chem. *25*, 1157–1174. https://doi.org/10.1002/jcc.20035.

101. Wang, J., Wang, W., Kollman, P.A., and Case, D.A. (2006). Automatic atom type and bond type perception in molecular mechanical calculations. J. Mol. Graph. Model. *25*, 247–260. https://doi.org/10.1016/j.jmgm.2005.12.005.

102. Eastman, P., Swails, J., Chodera, J.D., McGibbon, R.T., Zhao, Y., Beauchamp, K.A., Wang, L.P., Simmonett, A.C., Harrigan, M.P., Stern, C.D., et al. (2017). OpenMM 7: Rapid development of high performance algorithms for molecular dynamics. PLoS Comput. Biol. *13*, e1005659. https://doi.org/10.1371/journal.pcbi.1005659.

103. Ylilauri, M., and Pentikäinen, O.T. (2013). MMGBSA As a Tool To Understand the Binding Affinities of Filamin-Peptide Interactions. J. Chem. Inf. Model. *53*, 2626–2633. https://doi.org/10.1021/ci4002475.

104. Miller, B.R., 3rd, McGee, T.D., Jr., Swails, J.M., Homeyer, N., Gohlke, H., and Roitberg, A.E. (2012). MMPBSA.py: An Efficient Program for End-State Free Energy Calculations. J. Chem. Theor. Comput. *8*, 3314–3321. https://doi.org/10.1021/ct300418h.

105. Jones, H.B.L., Draganov, S.D., Huamán, S.S., Wing, P.A.C., Nguyen, C., Liang, Z., Dörner, J., Lithgow, J., Murphy, E., Beard, A., et al. (2025). ob ABPP-HT*: a Precision-Engineered Activity Proteomics Pipeline for the Streamlined Discovery of Deubiquitinase Inhibitors. Preprint at bioRxiv. https://doi.org/10.1101/2025.05.27.656269.

106. Surdo, N.C., Berrera, M., Koschinski, A., Brescia, M., Machado, M.R., Carr, C., Wright, P., Gorelik, J., Morotti, S., Grandi, E., et al. (2017). FRET biosensor uncovers cAMP nano-domains at beta-adrenergic targets that dictate precise tuning of cardiac contractility. Nat. Commun. *8*, 15031. https://doi.org/10.1038/ncomms15031.

107. Soltermann, F., Foley, E.D.B., Pagnoni, V., Galpin, M., Benesch, J.L.P., Kukura, P., and Struwe, W.B. (2020). Quantifying Protein-Protein Interactions by Molecular Counting with Mass Photometry. Angew. Chem. Int. Ed. *59*, 10774–10779. https://doi.org/10.1002/anie.202001578.

108. Smith, S.D., Jaffer, Z.M., Chernoff, J., and Ridley, A.J. (2008). PAK1-mediated activation of ERK1/2 regulates lamellipodial dynamics. J. Cell Sci. *121*, 3729–3736. https://doi.org/10.1242/jcs.027680.

109. Taglieri, D.M., Monasky, M.M., Knezevic, I., Sheehan, K.A., Lei, M., Wang, X., Chernoff, J., Wolska, B.M., Ke, Y., and Solaro, R.J. (2011). Ablation of p21-activated kinase-1 in mice promotes isoproterenol-induced cardiac hypertrophy in association with activation of Erk1/2 and inhibition of protein phosphatase 2A. J. Mol. Cell. Cardiol. *51*, 988–996. https://doi.org/10.1016/j.yjmcc.2011.09.016.

STAR★METHODS

KEY RESOURCES TABLE

REAGENT or RESOURCE	SOURCE	IDENTIFIER
Antibodies		
Yellow fluorescent protein antibody	Abcam	Cat# ab286192
PAK1 Antibody	Cell Signaling Technology	Cat# 2602; RRID:AB_330222
Phospho-PAK1 (Thr423)/PAK2 (Thr402) Antibody	Cell Signaling Technology	Cat# 2601; RRID:AB_330220
Phospho-MEK1 (Ser298) Rabbit Monoclonal Antibody	Cell Signaling Technology	Cat# 98195; RRID:AB_2800299
MEK1 Antibody	Cell Signaling Technology	Cat# 9124; RRID:AB_330804
Phospho-Merlin (Ser518) Antibody	Cell Signaling Technology	Cat# 9163; RRID:AB_2149793
Merlin Rabbit Monoclonal Antibody	Cell Signaling Technology	Cat# 6995; RRID:AB_10828709
Natriuretic peptides A antibody	Abcam	Cat# ab180649; RRID:AB_2858196
Phospho-p44/42 MAPK (Erk1/2) (Thr202/Tyr204) Rabbit Monoclonal Antibody	Cell Signaling Technology	Cat# 4370; RRID:AB_2315112
p44/42 MAPK (Erk1/2) Rabbit Monoclonal Antibody	Cell Signaling Technology	Cat# 4695; RRID:AB_390779
Phospho-SAPK/JNK (Thr183/Tyr185) Antibody	Cell Signaling Technology	Cat# 9251; RRID:AB_331659
SAPK/JNK Antibody	Cell Signaling Technology	Cat# 9252; RRID:AB_2250373
MKK7 Antibody	Cell Signaling Technology	Cat# 4172; RRID:AB_330914
Phospho-MKK7 (Ser271/Thr275) Antibody	Cell Signaling Technology	Cat# 4171; RRID:AB_2250408
Phospho-SEK1/MKK4 (Thr261) Antibody	Cell Signaling Technology	Cat# 9151; RRID:AB_330889
SEK1/MKK4 Antibody	Cell Signaling Technology	Cat# 9152; RRID:AB_330905
GAPDH Antibody	Santa Cruz Biotechnology	Cat# sc-32233; RRID:AB_627679
Phospho-PERK (Thr980) Rabbit Monoclonal Antibody	Cell Signaling Technology	Cat# 3179; RRID:AB_2095853
PERK Rabbit Monoclonal Antibody	Cell Signaling Technology	Cat# 3192; RRID:AB_2095847
BiP Antibody	Cell Signaling Technology	Cat# 3183; RRID:AB_10695864
CHOP Mouse Monoclonal Antibody	Cell Signaling Technology	Cat# 2895; RRID:AB_2089254
XBP-1s Rabbit Monoclonal Antibody	Cell Signaling Technology	Cat# 40435; RRID:AB_2891025
ATF6 antibody	Abcam	Cat# ab37149; RRID:AB_725571
ATF-4 antibody	Abcam	Cat# ab85049; RRID:AB_1861369
IRE1 (phospho S724) antibody	Abcam	Cat# ab48187; RRID:AB_873899
IRE1 antibody	Abcam	Cat# ab37073; RRID:AB_775780
Phospho-(Ser/Thr) PKA Substrate Antibody	Cell Signaling Technology	Cat# 9621; RRID:AB_330304
Wheat Germ Agglutinin (WGA) Alexa Fluor 488	Thermo Fisher Scientific	Cat# W11261; RRID: AB_2861250
beta-Actin Antibody	Cell Signaling Technology	Cat# 4967; RRID:AB_33028
GAPDH Rabbit Monoclonal Antibody	Cell Signaling Technology	Cat# 92310; RRID:AB_2799343
Goat anti-Mouse IgG (H+L) Secondary Antibody	Thermo Fisher Scientific	Cat# 31430; RRID:AB_228307
Goat anti-Rabbit IgG (H+L) Secondary Antibody	Thermo Fisher Scientific	Cat# 32460; RRID:AB_1185567
Chemicals, peptides, and recombinant proteins		
Dimethyl sulfoxide	Sigma-Aldrich	Cat# 34869
Kinase Assay Buffer I	Abcam	Cat# ab189135
PAKtide	SignalChem	Cat# E3104-6

(*Continued on next page*)

Continued

REAGENT or RESOURCE	SOURCE	IDENTIFIER
Adenosine 5'-triphosphate disodium salt hydrate	Sigma-Aldrich	Cat# A7699
Kemptide (PKA) Peptide Substrate	Promega	Cat# V5601
DMEM	Gibco™	Cat# 11965092
Penicillin-Streptomycin	Gibco™	Cat# 15140122
Glucose Solution	Gibco™	Cat# A2494001
Sodium chloride	Sigma-Aldrich	Cat# S9625
HEPES	Sigma-Aldrich	Cat# H3375
Magnesium Chloride	Sigma-Aldrich	Cat# 208337
N-hydroxysuccinimide (NHS)	Thermo Fisher Scientific	Cat# 24500
ethyl 3-(3-dimethylaminopropyl) carbodiimide (EDC)	Thermo Fisher Scientific	Cat# PG82079
Ethanolamine HCl	Bio-Rad	Cat# 1762450
Tris	Invitrogen™	Cat# 10259194
EDTA	Thermo Fisher Scientific	Cat# 17892
Fetal Bovine Serum	Thermo Fisher Scientific	Cat# A5256701
Isoprenaline hydrochloride	Merck Millipore	Cat# I5627
Angiotensin II	Merck Millipore	Cat# A9525
Potassium chloride	Sigma-Aldrich	Cat# P3911
Calcium Chloride	Abcam	Cat# ab285384
DPBS	Gibco™	Cat# 14190144
Hematoxylin and Eosin	Abcam	Cat# ab245880
Masson's Trichrome	Abcam	Cat# ab150686
Picro-Sirius Red staining	Abcam	Cat# ab245887
JB01	This study	N/A
JB79	This study	N/A
JB81	This study	N/A
JB120	This study	N/A
JB120-PAL	This study	N/A
PAK1-A1	MedChem Express	Cat# 496775-61-2
PAK1-A2	MedChem Express	Cat# 1033040-23-1
NVS-PAK1-1	MedChem Express	Cat# 1783816-74-9
PKA-A1	MedChem Express	Cat# 210101-16-9
PKA-A2	MedChem Express	Cat# 1037624-75-1
PAK1 activating peptide	This study	N/A
PKA activating pepfide	This study	N/A
PAK1 full-length protein	This study	N/A
PAK1 kinase domain protein	This study	N/A
PAK1 AID protein	This study	N/A
PAK1 kinase domain K299R protein	This study	N/A
Recombinant Human PRKAR1A protein	Abcam	Cat# ab125532
cAMP-Dependent Protein Kinase, Catalytic Subunit protein	Promega	Cat# V5161
PAK2 protein	Merck Millipore	Cat# 14-481
PAK3 protein	Merck Millipore	Cat# 14-683
Cdc42 protein	This study	N/A
Critical commercial assays		
Immunoprecipitation kit	Abcam	Cat# ab206996
Pierce™ Bradford Protein Assay Kit	Thermo Fisher Scientific	Cat# 23200

(*Continued on next page*)

Continued

REAGENT or RESOURCE	SOURCE	IDENTIFIER
ADP-Glo™ Kinase Assay	Promega	Cat# V6930
Phosphoproteomics	HaploX-Innovating Research	N/A
Deposited data		
PAK1 Hydrogen-Deuterium Exchange Mass Spectrometry	This study	ProteomeXchange: PXD074239
Crystal structure of PAK1+NVS-PAK1-1 complex	This study	PDB: 28OQ
Experimental models: Cell lines		
H9C2 cells	N/A	N/A
CHO cells	N/A	N/A
Experimental models: Organisms/strains		
C57BL/6J	Jackson Laboratory	000664
Actc1^{E99K} HCM mouse	Song et al.[52]	N/A
PAK1^{cko} mouse	This study	N/A
Recombinant DNA		
PAK1-FRET plasmid	Parrini et al.[79]	N/A
AKAR4 plasmid	Depry et al.[57]	N/A
PAK1-FRET-V385D plasmid	This study	N/A
PAK1-FRET-N383L plasmid	This study	N/A
PAK1-FRET- V318D plasmid	This study	N/A
PAK1-FRET- E315A plasmid	This study	N/A
PAK1-Y142K plasmid	This study	N/A
PAK1-K141D plasmid	This study	N/A
PAK1-Y131K plasmid	This study	N/A
Software and algorithms		
GraphPad Prism 9 and 10	GraphPad Software	https://www.graphpad.com/
ImageJ	Fiji	https://imagej.net/software/fiji/
AutoDock Vina	Trott and Olson[30]	https://autodock-vina.readthedocs.io/en/latest/index.html
ICM-VLS	Molsoft L.L.C.	https://molsoft.com/vls.html
OEDocking	OpenEye Scientific	https://www.eyesopen.com/
Pymol	Schrödinger, Inc.	https://www.pymol.org/
ChimeraX	Pettersen et al.[80]	https://www.cgl.ucsf.edu/chimerax/
Vevo F2 Software	Fujifilm VisualSonics	https://www.visualsonics.com/product/software/vevo-lab
MassHunter	Agilent Technologies	https://www.agilent.com/en/promotions/masshunter-mass-spec?srsltid=AfmBOoqvRxYvHA2q-le-SkBLPCKbce1vMl5L9EkqZcOF0L9Nof3NbV2V
HDExaminer version 3.4.2	Trajan Scientific and Medical	https://chronect.trajanscimed.com/hdexaminer-pro
MetaFluor 7.1	Molecular Devices	https://www.moleculardevices.com/products/cellular-imaging-systems/high-content-analysis/metamorph-microscopy
REFMAC5	MRC Laboratory of Molecular Biology	https://www2.mrc-lmb.cam.ac.uk/groups/murshudov/content/refmac/refmac.html
Coot	MRC Laboratory of Molecular Biology	https://www2.mrc-lmb.cam.ac.uk/personal/pemsley/coot/
Biacore S200 Evaluation Software	Cytiva	https://www.cytivalifesciences.com/en/us/support/software/biacore-downloads

EXPERIMENTAL MODEL AND STUDY PARTICIPANT DETAILS

Cell lines

H9C2 rat embryonic cardiomyoblast cell line (gift from T. Lanyon-Hogg.) and Chinese hamster ovary (CHO) cell line (gift from M. Zaccolo) were utilized in this study. H9C2 cells were maintained in DMEM (Dulbecco's Modified Eagle Medium, GlutaMAX; Gibco™) supplemented with 10% fetal bovine serum (FBS; Gibco™) and 1% penicillin-streptomycin (Gibco™). CHO cells were cultured in Ham's F-12 (GlutaMAX; Gibco™) containing 10% FBS and 1% penicillin–streptomycin. All cultures were maintained at 37 °C in a humidified incubator with 5% CO_2 and routinely passaged two to three times per week.

Mice

All littermate wild-type (WT) and heterozygous mice were housed and bred under specific pathogen-free conditions. For Actc1^{E99K} mouse studies involving PAK1-A2 treatment, all maintenance and experimental procedures were reviewed and approved by the local Animal Welfare and Ethical Review Body and conducted under project licenses authorized by the UK Home Office. The Actc1^{E99K} model (gift from H. Watkins), originally generated on a C57BL10xCBA/Ca background, was backcrossed onto a C57BL/6 (mixed 6N and 6J) background for more than 10 generations. Only heterozygous Actc1^{E99K} and Actc1^{NTG} littermates were used in the study (no homozygous E99K). Treatment was initiated at 4 weeks of age. For each of the three groups (WT, E99K + vehicle, and E99K + PAK1-A2), five mice were used (2 males and 3 females per group).

For the JB79-treated transverse aortic constriction (TAC) model, all animal experiments were performed in accordance with the NIH Guide for the Care and Use of Laboratory Animals and were approved by the Animal Care and Use Committee of Southwest Medical University, Sichuan, China, in compliance with national regulatory guidelines. Adult mice (8-10 weeks old) underwent TAC surgery followed by JB79 treatment, only male mice were included in the study.

For the PAP-treated Ang II-induced cardiac hypertrophy model, all animal procedures were conducted in accordance with the Guide for the Care and Use of Laboratory Animals published by the U.S. National Institutes of Health. Age- and sex-matched littermates were used in all the treatment groups. Adult mice (3-4 months old), with equal representation of males and females, were used for morphometric and biochemical analyses.

METHOD DETAILS

Peptide synthesis

PAK1 activating peptide (PAP) TSNSQKYMSFTDKSA was prepared as previously described.[28] Briefly, PAP derived from the PAK1 autoinhibitory region was linked to the 11-amino acid sequence YGRKKRRQRRR derived from HIV-1 trans-activating regulatory protein. The peptide (YGRKKRRQRRRGTSNSQKYMSFTDKSA) was synthesized in the proteomics core lab in Research Resource Centre at University of Illinois at Chicago (UIC), USA and was confirmed by mass spectrometry.

For PKA modulating peptides, we designed PKA-modulating peptides (Pα1, sequence: KGRRRRGAISAEVYTEEDAA SYVRKVIPKD), derived from the inhibitory segment and its C-linker region within the regulatory subunit RIα. Given the length of the entire inhibitory segment and linker region, we also developed Pα2 (sequence: KGRRRRGAISAEVYT) and Pα3 (sequence: EEDAASYVRKVIPKD). A control peptide derived form the inhibitory segment within the regulatory subunit RIIβ was also developed, Pβ (sequence: INRFTRRASVCAEAYNP). All these four peptides were linked to the 11-amino acid sequence YGRKKRRQRRR derived from HIV-1 trans-activating regulatory protein for cell permeabilization. These four peptides were synthesized by GL Biochem and was confirmed by mass spectrometry.

AlphaFold2 modelling of protein-peptide pairs

For PAK1 protein-PAP pairs, the structure of the PAK1 protein-PAP complex was predicted using AlphaFold2.[29] The AlphaFold2 calculations were executed on Google ColabFold v1.5.2, utilizing the human PAK1 sequence (UniProt: Q13153) and the PAP sequence TSNSQKYMSFTDKSA. To create the input for AlphaFold2, the PAP sequence was appended to the C terminus of the PAK1 sequence. Five structures were generated for each entry using AlphaFold2, and the structure with the highest-ranking based on the LDDT scores was chosen as the representative pose. The predicted structure was further refined by removing terminal modifications and low confidence loops. We validated the predicted AlphaFold 2 structures by running three replicates of 300 ns molecular dynamics simulations using the ff14SB force field and the TIP3P water model, observing that the peptide remained stably bound. All subsequent analyses were conducted using this representative pose.

For PKA protein-peptide pairs, the structure of the PAK1 protein-PAP complex was predicted using AlphaFold2. The AlphaFold2 calculations were executed on Google ColabFold v1.5.2, utilizing PKA RIα (UniProt: P10644) and catalytic subunit (UniProt: P17612) complex, as well as the Pα1 peptide (sequence: KGRRRRGAISAEVYTEEDAASYVRKVIPKD), Pα2 peptide (sequence: KGRRRRGAISAEVYT), and Pα3 peptide (sequence: EEDAASYVRKVIPKD). The initial modeling was conducted for the PKA protein-Pα1 pairs, and Pα1 was found to interact with the inhibitory segment, likely due to the significant length of the original inhibitory segment and the C-linker from RIα, which made displacement challenging. Therefore, for the rest of the modeling process, the inhibitory segment was removed during the modeling process to ensure that the inhibitory segment would not obstruct the potential binding site for Pα2 within the PKA structure. Five structures were generated for each entry using AlphaFold2, and the structure with the

highest-ranking based on the LDDT scores was chosen as the representative pose. For presentation clarity in the manuscript, the sequence preceding the RIα region, including the D/D domain (aa 1-90), has been removed.

In silico screening

A virtual screening workflow was employed for exploring the potential of targeting the autoinhibition release site identified by PAP using small molecule activators. To initiate the screening process, ZINC[15] lead-like compound library (around 2 million ligands) were screened using the ICM-VLS software.[81] PDB ID 1F3M[16] with the asymmetrical monomer removed, was used as the receptor to screen the compound library specifically at the PAP binding site, predicted by AlphaFold2.[29] The top hit compounds (100 in-stock compounds) were extracted from the screening results for further physical screening and evaluation.

The PAL-MS assay identified the key PAK1-activator binding site, but to explore whether a more precise pocket could yield better compounds, we opted for an additional virtual screening approach targeting the refined binding site. For this screening, we utilized the PAK1 structure from PDB 1F3M monomer structure.[16] Considering that the kinase inhibitory segment occupies the active site within the PAK1 kinase domain, and the PAL-MS results confirmed that PAK1 activators function by releasing the autoinhibitory mechanism associated with the kinase inhibitory segment, we proceeded to remove the kinase inhibitory segment from the PAK1 monomer to ensure that the kinase inhibitory segment would not obstruct the active binding site within the PAK1 kinase domain during the virtual screening process. The Make_Receptor tool (OpenEye, Cadence Molecular Sciences) was employed to generate the active binding site, utilizing key structural elements identified through PAL-MS analysis. The ZINC[15] in-stock libraries, including FDA-approved drugs (1615 ligands) and DrugBank[82] experimental compound (6252 ligands) libraries, were acquired, given their favorable physiochemical properties. Ligand preparation involved using Omega2 4.1.2.0 (OpenEye, Cadence Molecular Sciences)[83] to create multi-conformer structure databases, which were subsequently subjected to molecular docking using FRED (OpenEye, Cadence Molecular Sciences).[35,84] The Chemgauss4 scoring method with default settings was applied during the docking process. The top-ranked 30 compounds were extracted for further bioactive screening.

For PKA virtual screening, PKA structure PDB: 2QCS[56] without the inhibitory segment and the C-linker (aa 91-120) was used for the virtual screening process to ensure that the inhibitory segment would not obstruct the active binding site within the PKA structure. The ZINC[15] FDA-approved drugs (1615 ligands) were acquired to fit into the pocket identified by Pα2 peptide. Ligand preparation involved using Omega2 4.1.2.0 (OpenEye, Cadence Molecular Sciences)[83] to create multi-conformer structure databases, which were subsequently subjected to molecular docking using FRED (OpenEye, Cadence Molecular Sciences).[35,84] The Chemgauss4 scoring method with default settings was applied during the docking process. To narrow down the selection, the top compounds, 20 out of a total of 1615 compounds, were extracted for further bioactive screening.

Kinase activity screening with RapidFire- Mass Spectrometry

A high-throughput physical screening was conducted using a RapidFire 365 high-throughput mass spectrometry (MS) (Agilent) based kinase assay as previously described,[32,85] to evaluate the kinase activity of the top-ranked small molecules obtained from virtual screening. The RapidFire kinase assay was performed at room temperature utilizing 96-well plates (Agilent, 174194). The compounds, dissolved in dimethyl sulfoxide (DMSO), were accurately dispensed acoustically into assay-ready plates to achieve final compound concentrations of 5 μM and 10 μM, with a final DMSO concentration of 1%. The reaction mixture consisted of kinase assay buffer (Abcam, ab189134), 50 nM PAK1 enzyme, and 30 μM substrate PAKtide (SignalChem, E3104-6). Compounds were pre-incubated with PAK1 protein for 10 min, and the reaction started upon addition of 100 μM ATP (Sigma-Aldrich, A7699) and 30 μM substrate into each well, followed by incubation for 30 minutes at room temperature. Substrate phosphorylation was measured using RapidFire-MS. PAK1 kinase activity was determined based on the phosphorylated/total substrate PAKtide ratio. Compound responses were normalized to the DMSO control, and compounds exhibiting activity exceeding two times of the DMSO control were subjected to duplicate re-screening using the above assay. Confirmed hits were subsequently subjected to dose-response curves using the RapidFire-MS based kinase assay described above. Dose-response assays for PAK1-A1, PAK1-A2, and NVS-PAK1-1 (all from MedChem Express) were performed using full-length PAK1 protein. Serially diluted compounds were pre-incubated with the protein for 10 minutes, followed by the addition of substrate peptide and ATP to initiate the reaction. After a 30-minute incubation at room temperature, substrate phosphorylation peaks were measured using RapidFire-MS. The MS data analysis was performed using Mass Hunter (Agilent). Each compound underwent three repetitions of the dose-response assay. Further EC_{50} calculation and statistical analysis were performed using GraphPad Prism 9.

As for PKA physical screening, the compounds were dissolved in DMSO, while peptide were dissolved in ddH_2O to achieve final compound concentrations of 10 μM and 20 μM. The reaction mixture consisted of kinase assay buffer (Abcam, ab189134), and 30 μM substrate PAKtide (SignalChem, E3104-6). A 1:1 ratio of 30 nM PKA RIα subunit (Abcam, ab125532) and 30 nM catalytic subunit (Promega, V5161) was added to each well for compound screening. cAMP (Promega, V6421) was applied as a positive control. The reaction commenced upon addition of 100 μM ATP (Sigma-Aldrich, A7699) and 30 μM substrate into each well, followed by incubation for 20 minutes at room temperature. We initially tested both Kemptide (Promega, V5601) and PAKtide peptide substrates to assess PKA activity. Given the significantly higher phosphorylation rate observed with PAKtide compared to Kemptide, we selected PAKtide as the preferred substrate for the remainder of the PKA compound screening assays. Substrate phosphorylation was measured using RapidFire-MS. PKA kinase activity was determined based on the phosphorylated/total substrate PAKtide ratio.

Compound responses were normalized to the DMSO control, and compounds exhibiting activity exceeding two times of the DMSO control were subjected to dose-response test. The MS data analysis was performed using Mass Hunter (Agilent).

For PKA activators, PKA-A1 and PKA-A2, dose-response assays were conducted using a 1:1 ratio of 30 nM PKA RIα subunit and 30 nM catalytic subunit to evaluate their effect on liberating PKA inhibitory regulation. Each compound underwent three repetitions of the dose-response assay. Further EC_{50} calculation and statistical analysis were performed using GraphPad Prism 9.

PAK1 kinase kinetic assay

For the kinetic experiments, we applied the RapidFire-MS based kinase assay described above. Compounds JB01 (20 μM), JB79 (20 μM), and JB81 (20 μM) were tested along with the PAK1 full-length protein (50 nM) and Cdc42 (100 nM). The experiments were conducted by adding the PAK1 and Cdc42 proteins into a kinase buffer. Following this, the compounds of interest were added and the reaction mixtures were pre-incubated for 10 minutes. After the pre-incubation, ATP (100 μM) and the substrate (30 μM) were added simultaneously to initiate the reaction. Continuous recording of the reaction progress was performed for a duration of 80 minutes, ensuring the substrate was fully phosphorylated. The recorded data was then subjected to analysis to determine the rate of substrate phosphorylation and assess the effects of the compounds JB01, JB79, and JB81 on kinase activity.

The kinetic assays involving compound PAK1-A1 (10 μM) and NVS-PAK1-1 (10 μM) were performed as described above. Briefly, the PAK1 full-length (50 nM) and PAK1 kinase domain protein (50 nM) were utilized, respectively without the presence of Cdc42, Continuous recording of the reaction progress was performed for a duration of 30 minutes to reach full phosphorylation of the substrate. The competitive kinase assay involved four parallel experiments to assess the competitive binding between PAK1-A1 and NVS-PAK1-1. In each experiment, the PAK1 full-length protein was subjected to different pre-incubation conditions. Firstly, it was pre-incubated with DMSO for 10 minutes, followed by the addition of PAK1-A1 and substrate to initiate the reaction. Secondly, the PAK1 protein was pre-incubated with DMSO, and then NVS-PAK1-1 and substrate were added to start the reaction. Thirdly, the PAK1 protein was pre-incubated with NVS-PAK1-1 for 10 minutes, and then PAK1-A1 and substrate were added to initiate the reaction. Lastly, the PAK1 protein was pre-incubated with PAK1-A1, and then NVS-PAK1-1 and substrate were added to start the reaction. The reaction progress was continuously recorded for 30 minutes. The kinetic kinase experiments were repeated at least twice to ensure the reliability of the results. Data were fitted using Prism 9 (GraphPad).

PAK1 protein expression and purification

PAK1 protein expression and purification were performed as previously described.[16] PAK1 full-length constructs were cloned into expression vector pNIC28-Bsa4 which adds an N-terminal hexahistidine tag and a TEV protease recognition site for removal of the tag. The constructs were transformed into Escherichia coli strain NB42 along with a plasmid expressing the bacteriophage lambda phosphatase and three rare tRNAs, to ensure production of the unphosphorylated kinases. Cells were grown at 37°C in LB medium to an OD600 of 0.4–0.5 and temperature lowered to 18°C prior to induction of protein expression by the addition of 0.4 mM isopropyl 1-thio-d-galactopyranoside at an OD600 of 0.6. The following morning cells were harvested by centrifugation and resuspended in lysis buffer (50 mM HEPES pH 7.5, 500 mM NaCl, 5% glycerol, 20 mM imidazole, 0.5 mM TCEP, 1:1000 dilution of Merck protease inhibitor cocktail set III). Pellets were stored frozen until required, then gently thawed in lukewarm water and lysed by sonication on ice. After centrifugation, the cleared lysate was applied on His Trap column (GE Healthacare) equilibrated with lysis buffer. Following the washing with the lysis buffer containing 60 mM imidazole, proteins were eluted with same buffer containing 400 mM imidazole. The 6x His tag was cleaved by the addition of recombinant TEV protease during overnight dialysis into the buffer without imidazole. The released 6x His-tag was removed by applying the protein mixture to the His-Trap column again. The PAK1 full-length protein in the flow-through fractions was concentrated and loaded on a Superdex 200 size-exclusion column equilibrated with 125 mM NaCl, 20 mM Tris-HCl, pH 8.0. This procedure typically yielded 15–20 mg PAK1 full-length protein from 2 liters of bacterial culture.

For Cdc42, all purification buffers contained an additional 50μM GDP and 5 mM magnesium chloride. To prepare activated Cdc42, the nucleotide was exchanged by addition of 10 mM EDTA, 1 mM DTT, 100 U of calf intestinal alkaline phosphatase (CIP) and 0.55 mM GppCp (β,γ-methyleneguanosine 5′-triphosphate) with overnight incubation at 4°C, followed by SEC, as before, and substituting 50 μM GppCp for GDP in the SEC buffer.

For PAK1 kinase domain protein purification, the human kinase domain of PAK1 gene (aa 249-545) with mutation K299R was cloned into pET28-6His-SUMO expression vector. The protein was expressed in E. coli BL21-Gold (DE3) cells. For protein expression, bacteria were grown in LB medium with kanamycin at 37°C until they reached OD600=0.8, cooled down to 18°C, induced with 0.4 mM isopropyl β-D-1-thiogalactopyranoside (IPTG) and cultured for 16 h at 18°C. Cells were harvested by centrifugation, and the pellet was washed with 1 x Phosphate Buffered Saline (PBS, 137 mM NaCl, 2.7mM KCl, 10 mM Na2HPO4, 2mM 2 mM KH2PO4, pH 7.4).

Cells from 4 l culture were resuspended in 50 ml buffer 1 (20 mM Tris-HCl pH 8.0, 250 mM, 20 mM imidazole and 5 mM β-mercaptoethanol) and sonicated. Cells lysate was cleared by ultracentrifugation at 40,000 rotation per minute (rpm, Beckmann Coulter, 45Ti rotor). The lysate was applied on a His-Trap column (GE Healthcare) that was equilibrated with buffer 1. The column was washed with buffer 1, followed by a wash with the same buffer supplemented with 60 mM imidazole. Proteins were eluted with buffer 1 containing 400 mM imidazole. To remove the 6xHis-SUMO, the fusion protein was digested overnight with a SUMO protease. Before applying the sample on the second His-Trap column, imidazole was removed by ammonium sulfate precipitation

(1 ml of cold protein solution was precipitated with 0.4 g of (NH4)2SO4.). The cleaved-off SUMO protein was removed on a His-Trap column (GE Healthcare). The flow-through that contained the tagless protein was concentrated and applied to a size exclusion column (HiLoad 16/600 Superdex S200, GE Healthcare) that was equilibrated with storage buffer (20 mM TRIS-HCl pH 8.0, 150 mM NaCl, and 1 mM dithiothreitol [DTT]). Pooled fractions were concentrated using an Amicon Centrifugal Filter Device (Millipore). Purified proteins were characterised using denaturing liquid chromatography–mass spectrometry (LC–MS) and SDS–PAGE, then flash frozen in liquid nitrogen and stored at −80°C until required.

The autoregulatory (AID) fragment (aa 79-149) was cloned into the pET28-6His-SUMO expression vector. The expression and the first step of purification for AID were analogous to those described for the PAK1 protein. The PAK1-AID complex was prepared by mixing the proteins during the purification procedure. The AID protein eluted from the HisTrap column with 6xHis-SUMO tag was mixed with tagless PAK1 protein. The mixture was then incubated on ice in the buffer 1 for two hours. To remove the excess of uncomplexed PAK1 protein, the mixture was loaded onto His-Trap column (Cytivia) equilibrated with buffer 1. The complex was eluted with buffer 1 containing 400 mM imidazole. During an overnight dialysis in buffer 1, the Ulp1 protease digested 6xHis-SUMO tag. The cleaved-off SUMO protein was removed on a HisTrap column (Cytivia). The flow-through fractions that contained the tagless proteins were concentrated and applied to a size exclusion column (HiLoad 16/600 Superdex S200, GE Healthcare) that was equilibrated with storage buffer (20 mM TRIS-HCl pH 8.0, 150 mM NaCl, and 1 mM dithiothreitol [DTT]). The fractions with purified complex were concentrated to 5 mg/ml using Amicon Centrifugal Filter Device with cut-off 3kDA (Millipore), flash frozen in liquid nitrogen and stored for further use.

Structure-activity relationship and compound optimization

The chemical space within the ligand binding site based on the obtained structural activity relationship (SAR) data was explored to achieve further understanding of the molecular recognition site where the ligand binds. JB79 was breakdown into three fragments, branching group R1 (m-carboxyphenyl), another branching group R3 (m-aniline), and a linker between these groups. These three functional groups were specifically modified and substituted by majority of other analogues surrounding the functional groups of the compounds to understand the SAR. Over one hundred new compounds were synthesized and their effect on PAK1 kinase activity were measured using RapidFire-MS kinase assay described above.

On the R1 group, having a strong electron withdrawing group at the para-position was found to provide the highest stimulatory effect on PAK1. Carboxylic acid groups were found to be more activating in comparison to relatively weaker groups, such as the ester COOR. Extending the compound by a methylene also increases the stimulatory effect of the activators. On the R3 group of the compound, the nitro group was found to be not too crucial in conferring the stimulatory effect of PAK1. Halogen substitutions also illustrated that ortho- and para- positions more favorable in producing its efficacy than the meta-positioned groups. As nitro groups were often reported to cause hepatoxicity, replacing the nitro group with another lesser deactivating group was found to be more favorable towards improving the physiochemical profiles of the activators. In addition to changing the surrounding functional groups of compounds, replacement of the core group (R2) was also considered in order to substitute for the acrylonitrile core. Five different core groups were tested while containing similar pharmacophore properties. Based on the Rapidfire-MS Kinase assays, some compounds activity was still retained even after the Knoevenagel core groups were replaced. Amongst these different core groups, the amide core group was shown to confer the highest stimulatory effect in PAK1 activation, while significantly reducing with the MW and TPSA. Removing the nitrile and the carboxylic acid moiety were also shown to lower the melting point and improve its aqueous solubility. Overall, the SAR information obtained from the optimization allowed us to further understand the interaction between the small molecule activators and PAK1.

Compounds which have been tested for kinase activity assay were sent for DMPK studies. After a careful analysis, comparing both of their efficacies and DMPK results, the final chosen lead compound from the optimization process was JB120, which showed significant improvement in their ability to stimulate PAK1 activity. The lipophilicity (cLogD) was measured to have notably increased in comparison to the value from JB79, 0.40. TPSA was also significantly decreased, illustrating potential capability of the compound's permeability to membrane. Finally, both the melting point and the MW of the compounds became substantiality reduced, overall demonstrating characteristics that are more drug-like.

Photoaffinity labelling in PAK1 activator binding-site identification

To refine the binding site of PAK1 activator and to get insight into mechanism of its action, we performed additional photo-affinity labeling (PAL) coupled to mass spectrometry (PAL-MS) as previously described.[86,87] We synthesised several JB120 photoaffinity reporters and used structural proteomics to investigate the ligand binding sites. Based on the preliminary SAR studies that high polar groups at the meta- and para-positions were shown to improve PAK1 stimulation, JB120-PAL and JB120-PAL-2 were designed, which contains a diazirine photocross-linker at the para- and meta-position accordingly. An additional JB120 photoaffinity reporter, JB120-PAL-3, was synthesized to serve as a potential negative control. Three photoaffinity reporters were then evaluated in PAK1 kinase activity assay using Rapidfire-MS to make sure the incorporated photo-activating groups do not significantly alter the binding affinity and functionality of the ligand.

Full-length PAK1 (0.5 μM) was added into kinase buffer, then pre-incubate with JB120-PAL and DMSO control for 3 h. Due to the importance of Cdc42 in potentially increasing the affinity of the compound binding, another condition was added to introduce Cdc42 in addition to the PAK1 full-length alone. A competitive assay using JB120-PAL together with JB120 compound was also conducted

to determine if JB120-PAL and the parent compound JB120 are binding at the same site. After three-hour treatment, the diazine photoaffinity label incorporated to the JB120 allows the covalent modification to occur once the UV radiation treatments were given. After 20 min of UV irradiation at 365 nm, acetone precipitation (1:9) for PAK1 protein were performed, followed by protein digestion and peptide desalting. NanoLC-MS/MS was applied for proteomics measurement and the automatic peptide sequencing was achieved using the MaxQuant Software.

Raw MS data were processed using MaxQuant and the parameters used for detecting peptides with unknown modifications included a DP Score >60 and a mass error tolerance < 6 ppm. Peptide identification was performed using Andromeda search engine integrated into MaxQuant. The dynamic programming (DP) score was used to filter out low-confidence identifications. Quantitative data were normalized and statistically analyzed to identify differentially labelled peptides. The resulting matrix contained intensity information of the unlabeled and labelled variants of each peptide, which were added and compared, normalized to total peptide intensities. Quantitative proteomics analysis revealed that for PAK1 treated with JB120-PAL, there were four modified peptides with five specific residues highly abundant with ΔM mass shift corresponding to JB120-PAL (461.09KDa). Additionally, these peptides were less abundant in the presence of the competitor parent JB120 compound, indicating competitive antagonism to the PAL. These results confirm that the peptide mass shift by the covalent modification is evident with the PAL probe compound.

LC-MS/MS Analysis of PAK1 and PAK1+Cdc42 Peptides

Peptides were analyzed by nanoLC-MS/MS with the Easy nLC 1000 (Thermo Fisher Scientific) coupled online to a Q-Exactive Plus (Thermo Fisher Scientific) with a NanoFlex source (Thermo Fisher Scientific). Analytical column (40 cm long, 75-μm inner diameter) were packed in-house with Reprosil-Pur C18 AQ 1.9-μm reversed phase resin (Dr Maisch GmbH, Germany) with a pulled emitter. To reduce the backpressure at high flow rates and to enhance separation efficiency, the column compartment was kept at 60°C. The peptide mixture (2 μg) was loaded onto the analytical column with 2% solvent B (80% ACN, 5% DMSO, 0.2% FA) in solvent A (5% DMSO, 0,2% FA) at a flow rate of 400nL/min and separated with a linear gradient of 2% to 30% solvent B over 157 min at a flow rate of 250 nl/min. Then the gradient is increased from 30% to 60% solvent B in 19 min and to 90% in 1 min and the column is equilibrated between 5 min at 2%. Due to the loading, lead-in, and washing steps, the total time for an LC-MS/MS run was about 180 min. The Q-Exactive Plus was operated in data-dependent acquisition mode using the following settings: full-scan automatic gain control (AGC) target 3e6 at 70 000 resolution; scan range 300–1,750 m/z; Orbitrap full-scan maximum injection time 45ms; MS2 scan AGC target 3,2e3 at 17,500 resolution; maximum injection 45ms; normalized collision energy 27; dynamic exclusion time 30s; isolation window 2.2 m/z; 10 MS2 scans per full scan.

In vitro competitive photoaffinity labelling and MS-Analysis

Recombinant human PAK1 protein (0.5 μM, 26.2 μg) in 1mL PBS was pre-incubated with 40 μM of the parental compound JB120 or DMSO for 15 min and then treated with 40μM of the JB120-PAL or DMSO for 3h at RT. In parallel, PAK1 protein (0.5 μM, 26.2 μg) and the recombinant human Cdc42 (1 μM, 214 μg) were co-incubated in 1 mL PBS and pre-treated with 40 μM of JB120 or DMSO for 15 min followed by a treatment with 40 μM of JB120-PAL or DMSO for 3h at RT. After incubating in the dark at RT, samples were UV-irradiated (365 nm) for 20 min at 4°C. After photolysis, dry acetone (9 volumes) prechilled to -20°C was added and the cloudy mixture was vortexed thoroughly and incubated at -20°C overnight. After centrifugation (15,000 x g for 10 min at 4°C), the supernatants were poured off and the remaining pellets washed with -20°C acetone. The wash supernatants were removed by centrifugation and the precipitated protein pellets were air-dried for 10 min at RT and resuspended in 90 μL urea 8 M in 50 mM NH4HCO3.

Samples were reduced in 2 mM DTT at RT for 60 min and alkylated with 4mM iodoacetamide for 45 min at RT in the dark. After an 8-fold dilution in 50 mM NH_4HCO_3, proteins were digested using respectively 1 μg for PAK1 and 9 μg for PAK1+Cdc42 in a final enzyme:substrate ratio of 1:25 (w/w) and incubated overnight at 37°C under gentle agitation. Peptide mixtures were further acidified (0.5% TFA final concentration) and desalted using SepPak t-C18 Vac cartridges. First, the cartridges were initially pre-conditioned using 2 mL of 100% acetonitrile and equilibrated with 2mL 0.1% TFA in H20. The trypsin digest was loaded, centrifuged onto the Vac cartridges and washed twice with 1mL 0.1% formic acid (FA) in H20. Elution was performed with 1 mL 80% acetonitrile/0.1% FA, evaporated under vacuum and frozen at -20°C until use. Before LC-MS/MS analyses, peptides were resuspended in 0.1% FA to get a final concentration of 0.5 μg/μl.

Crystallization and X-Ray Data Collection for PAK1 autoinhibitory domain + kinase domain K299R structure

The purified protein was used in crystallization trials employing both, a standard screen with approximately 1200 different conditions, as well as crystallization conditions identified using literature data. Conditions initially obtained have been optimized using standard strategies, systematically varying parameters critically influencing crystallization, such as temperature, protein concentration, protein-well solution volume ratio, and others. These conditions were also refined by systematically varying pH or precipitant concentrations. Crystals have been flash-frozen and measured at a temperature of 100 K. The X-ray diffraction data have been collected from crystals of PAK1 at the SWISS LIGHT SOURCE (SLS, Villigen, Switzerland) using cryogenic conditions. The crystals belong to space group P21. Data were processed using the programs XDS and XSCALE.

Crystallization of PAK1 kinase domain K299R–compound complexes

Crystallization trials were performed using the siting-drop vapor diffusion method at 18°C using the commercially available screens. Prior to crystallization, the protein was mixed with an activator or an inhibitor at a molar ratio 1:3. The final protein concentration was 6 mg/ml. The best diffracting crystals were obtained after optimization using the hanging drop vapor diffusion method in the conditions contained 0.1 M HEPES pH 7.5, 0.2 M (NH4)2SO4 and 24 % (w/v) PEG 3350 initially identified in INDEX screen from Hampton Research.

All of the X-ray diffraction datasets were collected at the BESSY II storage ring, at MX BL14.1 beamline. The crystals belonged to P 21 space group. Data were processed and scaled by XDSAPP GUI.[88] The structure was solved by molecular replacement using the Phaser module[89] in Phenix.[90] The structure of kinase domain of PAK1 PDB ID: 4ZLO was used as a search model.[39] The asymmetric unit contained two protein molecules that formed a dimer. The structure was refined in phenix.refine with manual building in Coot.[91]

Structure Modelling and Refinement

The phase information necessary to determine and analyze the structure was obtained by molecular replacement. A previously solved structure of PAK1 was used as a search model. Subsequent model building and refinement was performed according to standard protocols with the software packages CCP4 and COOT. For the calculation of the free R-factor, a measure to cross-validate the correctness of the final model, about 7.5 % of measured reflections were excluded from the refinement procedure. TLS refinement (using REFMAC5, CCP4) has been carried out, which resulted in lower R-factors and higher quality of the electron density map. The water model was built with the ''Find waters''-algorithm of COOT by putting water molecules in peaks of the Fo-Fc map contoured at 3.0 sigma followed by refinement with REFMAC5 and checking all waters with the validation tool of COOT. The criteria for the list of suspicious waters were: B-factor greater 80 Å2, 2Fo-Fc map less than 1.2 sigma, distance to closest contact less than 2.3 Å or more than 3.5 Å. The suspicious water molecules and those in the ligand binding site (distance to ligand less than 10 Å) were checked manually. The Ramachandran Plot of the final model shows 90.1 % of all residues in the most favored region, 9.5 % in the additionally allowed region, and 0.3 % in the generously allowed region. No residues are found in the disallowed region.

Molecular dynamics simulations

Initial geometries were obtained from the soaked structure of PAK1 kinase domain in complex with NVS-PAK1-1, PDB: 1F3M (apo structure of PAK1 with the autoinhibitory domain)[16] and the docked structure of PAK1-A1. In the case of the PAK1/PAK1-A1 complex, Autodock Vina was applied to dock PAK1-A1 into full-length PAK1 using the PDB structure 1F3M.[30] The structure with the best docking score was used as the initial pose for molecular dynamic simulations. In the case of NVS-PAK1-1, the co-crystal structure of PAK1 kinase domain ^{K299R}-NVS-PAK1-1 complex was used for the simulation. The PAK1 autoinhibitory domain was superposed on PAK1 kinase domain structure, and the structure was minimized using MMFF94 in Avogadro.[92,93] PDBFixer was used to mutate residues in the PDB structures to match the canonical UniProt sequence (UniProtKB: Q13153), and to repair missing loops in the crystal structures. Cis peptide bonds and chiral centers with incorrect stereochemistry within rebuilt sections of protein structures were identified and corrected using the Cispeptide and Chirality plugins of Visual Molecular Dynamics.[94,95] Complexes were then solvated in orthorhombic boxes with a minimum of 1.4 nm between protein atoms and the box edge, and the protonation states were adjusted to pH 7.2 using the H++ server.[96] Counterions of Mg^{2+} and Cl^{-} were added to match the experimental ionic force of 0.1 M using the SPLIT method.[97] All simulations were carried out using the AMBER FF14SB force field for protein atoms,[98] the TIP3P model for rigid water molecules,[99] and the General Amber Force Field (GAFF) for the ligands,[100] using atomic charges calculated from the minimized AM1 structures using ANTECHAMBER.[101]

All simulations were run using OpenMM and NVIDIA Quadro RTX 6000 GPUs.[102] Pressure was fixed to 1 bar using a Monte Carlo barostat, and temperature was set using the Langevin thermostat. Before production simulations were carried out, complexes were minimized and then heated to 298 K at constant volume with protein atoms restrained. These restraints were relaxed over a set of five 100 ps simulations at constant pressure, culminating with 100 ps of unrestrained equilibration. Production runs were then simulated for 400 ns. All systems were run through this protocol in triplicates. Representations of the complex were prepared using PyMOL and ChimeraX.[80]

Free energy calculations

Free energy calculations were carried out using the Molecular Mechanics with Generalized Born and Surface Area solvation (MM/GBSA) method.[103] Each calculation used 30 replicates of 5 ns equilibrium trajectories started from a relaxed and equilibrated structure extracted from long molecular dynamics simulations. Each of the 30 replicates was subject to the same minimization, heating and equilibration procedure described in the section above. Free energies were calculated using the MMPBSA.py program in AmberTools,[104] and 100 frames collected every 40 ps from the final 4 ns of each 5-ns trajectory (i.e., 3,000 frames per complex). Per-residue energy contributions to the binding energy were computed using the MMPBSA.py DECOMP functionality.

Native mass spectrometry

Native MS assay was conducted as previously described.[40] The full-length PAK1 was buffer exchanged into 200 mM ammonium acetate pH 8.0 using a Biospin-6 (BioRad) column. PAK1-A1 was first solubilised in DMSO to 10 mM concertation and then further diluted into ammonium acetate buffer for subsequent binding analyses. The samples were introduced directly into the mass

spectrometer using gold-coated capillary needles (prepared in-house). Data were collected on a Q-Exactive UHMR mass spectrometer (Thermo Fisher Scientific). The instrument parameters were as follows: capillary voltage 1.0 kV, S-lens RF 100%, quadrupole selection from 1,000 to 20,000 m/z range, collisional activation in the HCD cell 20 V, trapping gas pressure setting 7.5, temperature 200 °C, and resolution of the instrument 12,500. The noise level was set at 3 rather than the default value of 4.64. No in-source dissociation was applied. Data were analysed using Xcalibur 4.2 (Thermo Scientific) and UniDec software packages.

Surface plasmon resonance (SPR)

SPR binding experiments were performed on a Biacore S200 instrument (Cytiva) at 25 °C using CM5 sensor chips. The running buffer used for PAP measurement was 20 mM HEPES, 150 mM NaCl, and 10 mM $MgCl_2$ (pH 7.4). For small-molecule measurements, the running buffer additionally contained 1% (v/v) DMSO to ensure compound solubility. Sensor chips were chemically activated for 5 min by injecting 175 μL of a 1:1 mixture of 100 mM N-hydroxysuccinimide (NHS) and 400 mM ethyl 3-(3-dimethylaminopropyl) carbodiimide (EDC) at a flow rate of 10 μL/min. Full-length PAK1 protein (40 μg/mL) was immobilized by amine coupling in 10 mM sodium acetate buffer (pH 5.0) for 5 min at a flow rate of 10 μL/min using a custom surface preparation method in the instrument control software. Remaining activated groups were blocked by injection of 1 M ethanolamine (pH 8.0). PAK1 was immobilized to a level of approximately 10,000–12,000 resonance units (RU) per flow cell.

Following immobilization, two startup cycles of running buffer were performed prior to analyte injections. PAP and small-molecule analytes were injected with an association time of 100 s and a dissociation time of 100 s at a flow rate of 10 μL/min. An eight-point concentration series was used for PAP and each compound. PAP was solubilized in ddH_2O, while small-molecule compounds were prepared as 10 mM stock solutions in 100% DMSO and serially diluted in ddH_2O and DMSO, respectively, prior to further dilution in running buffer, resulting in a final DMSO concentration of 1% (v/v) in all injections. Zero-concentration control injections (running buffer containing ddH_2O for PAP, and running buffer containing 1% DMSO for small molecules) were included at the beginning and end of each dose–response experiment to establish baseline stability and internal reproducibility. To correct for bulk refractive index effects of DMSO, sensorgrams from the zero-concentration control were subtracted from analyte sensorgrams during analysis.

SPR data were processed using Biacore S200 Evaluation Software (Cytiva) with subtraction of the blank reference flow cell (double referencing). Equilibrium binding responses were obtained by averaging the response over the final 5–10 s of the association phase, once binding had reached a stable plateau. The resulting equilibrium responses were exported and plotted against analyte concentration in GraphPad Prism 10. Steady-state binding curves were fitted using a one-site specific binding model ($Y = Bmax*X / (K_D + X)$) to determine equilibrium dissociation constants (K_D). Apparent K_D values for small-molecule analytes were estimated due to limitations in fitting robustness. Final figures were generated using GraphPad Prism 10.

HDX-MS Sample Preparation

Hydrogen Deuterium exchange Mass Spectrometry (HDX-MS) experiments were undertaken to identify the compound interaction interface on the recombinant PAK1 protein. PAK1 stocks (16 μM) were prepared in 50 mM TRIS, 150 mM NaCl, 2 mM DTT, 0.5 mM EDTA, and 20% glycerol. The protein was pre-incubated in both the presence (holo-PAK1) and absence (apo-PAK1) of compound PAK1-A1 for a total of 60 min and at room temperature to facilitate full complex formation. A molar ratio of 1:9 PAK1:PAK1-A1 was prepared. Samples were subsequently diluted to reach a final concentration of 20 pmol PAK1 on column.

HDX-MS Data Acquisition

The experimental HDX-MS workflow was similar to that previously described.[105] Briefly, a labeling buffer mimicking that of the protein stock solution (except in the absence of EDTA and glycerol) was prepared in deuterium oxide D2O (99+ %D, Cambridge Isotope Laboratories, Tewksbury, MA), with the pH adjusted to pD 6.40 (pD=pH+0.4). To achieve and maintain high protein occupancy following complex dilution, the labelling buffer was supplemented with 35 μM compound in 4% DMSO. The labelling buffer for apo-PAK1 contained 4% DMSO only. A quenching buffer containing 0.8% formic acid, pH 2.22 was prepared in H2O. Following initial complex formation and equilibration, samples were diluted in deuterium labeling buffer in a 1:10 ratio to achieve a final excess D2O concentration of 86.5%. Labeling time points of 0.16, 0.20, 1, and 100 min were sampled at 20°C. These corresponded to exchange times corrected to standard HDX conditions (pH 7.5) of 1, 3, 6, and 600 sec. Replicate numbers and statistical significance values are available in Table S2. At the end of each labeling time, samples were quenched upon addition of quench buffer (1:1 ratio), achieving a final pH of 2.55. Samples were then digested on a dual protease column containing a combination of pepsin and protease XIII acidic proteases (2.1 x 3.0 mm; NovaBioAssays, MA) at 8°C for 3 min. Peptides were first trapped and desalted on a 1.0 mm x 5.0 mm, 5.0 μm cartridge (Thermo Scientific™ Acclaim PepMap100) at a flow rate of 150 μL/min. Peptide separation was performed on a Thermo Scientific™ Hypersil Gold™ C18 column (50 x 1 mm, 1.9 μm) using a linear gradient of 2-40% Buffer B (Buffer A: water, 0.1% formic acid; Buffer B: ACN, 0.1% formic acid) at a flow rate of 80 μL/min. After each sample injection, a protease wash of 2 M guanidine, 0.8% formic acid, pH 2.3 in water was performed to limit peptide carry-over. To minimize back-exchange, the LC system was maintained at 1.5°C throughout the experiment. Labeling, quenching, and online digestion were performed with the aid of an automated HDX robot (Trajan Scientific and Medical), with sample acquisition and management controlled by Chronos (version 5.4.1). Labeled samples were analysed in MS1 mode on a Thermo Scientific™ Orbitrap Exploris™ 480 Hybrid™ mass spectrometer.

HDX-MS Data Analysis

Prior to the labeling experiments, a nonspecific digestion database of non-deuterated PAK1 peptides was generated in BioPharma Finder (version 5.2) using a combined data-dependent and targeted HCD-MS2 acquisition workflow. HDX labeling data were processed and manually curated in HDExaminer (version 3.4.2, Trajan Scientific and Medical). For each peptide, the charge state yielding the highest-quality spectra across all replicates and labeling time points was selected for the final analysis. Residual plots and heat maps were used to compare the apo- and holo-states of PAK1. Significant differences at the residue level were used to derive consensus HDX-MS effects (based on overlapping peptides), which were mapped onto the AlphaFold structural model of PAK1.

Generation of PAK1 biosensor

The Foerster Resonance Energy Transfer (FRET) based PAK1 biosensor Pakabi was a kind gift from Dr. Maria Carla Parrini, Institut Curie, Paris, France.[79] Briefly, the cDNA fragment encoding the region 65–545 (C terminus) of the WT PAK1 protein was cloned using PCR-based methods as a Sal1-Not1insert into the Xho1-Not1 sites of vectors from the pRaichu-Ras family, which are derived from the pCAGGS eukaryotic expression plasmid. Pakabi encodes the following chimeric protein: yellow fluorescent protein (YFP) (aa 1–239), a spacer (Leu-Asp-Thr-Met), human PAK1 (aa 65–545), a spacer (Cys-Gly-Arg), and cyan fluorescent protein (CFP) (aa 1–237) to generate the PAK1 –FRET biosensor YFP-PAK1-CFP. In this construction, the enhanced YFP (T65G, V68L, S72A, M153T, V163A, S175G, and T203Y) was used as an acceptor and enhanced CFP (K26R, Y66W, D129G, N146I, M153T, V163A, N164H, and S175G) as a donor. Plasmids were sequenced for verification.

For mutagenesis, biosensors carrying the following PAK1 mutations were used: D407K, V385D, N383L, V318D, E315A, Y142K, K141D, Y131K. The residues picked for mutagenesis is based on the PAL-MS results and those involved in the autoinhibitory regulation of PAK1. The substitution of these amino acids within PAK1 abolishes the interactions between the ligand and protein. All constructs cloning and amplification were conducted by GenScript Biotech.

Cell culture

Chinese hamster ovary (CHO) cell line was used for biosensor plasmid transfection and FRET experiments. CHO cells were cultured in Ham's F-12 GlutaMAX™ Supplement Medium (Gibco™, 31765035) containing 10% Fetal Bovine Serum (FBS) (Gibco™, 15575309), 1% L-Glutamine (Gibco™, 15430614), and 1% penicillin–streptomycin (Gibco™, 11568876) at 37 °C and 5% CO_2. Cells were seeded on 24 mm cover glasses (VWR, 631-1583) over 24 h to adhere before plasmid transfection. Transfected cells were kept in culture for less than 36 h, followed by FRET imaging.

For cellular efficacy study of PAK1-A1 and PAK-A2, H9C2 cell line was applied for the compound and Isoprenaline (ISO) (Sigma-Aldrich, I5627) treatment. H9C2 cells were cultured in DMEM containing 10% FBS, 1% L-Glutamine, and 1% penicillin–streptomycin at 37 °C and 5% CO_2. For hypertrophy induction, cells were starved in serum-free MEM for 4 h prior to addition of 50 μM ISO for 48 h with or without the treatment of 40 μM PAK1 A1 and PAK1-A2. Further immunoblots and staining were performed to assess cellular hypertrophy.

Transient transfection of WT, mutant PAK-FRET, and AKAR4 constructs in CHO cells

PAK1 FRET biosensor-WT and mutant (D407K, V385D, N383L, V318D, E315A, Y142K, K141D, and Y131K) plasmids, as well as AKAR4 construct,[57] were used for transient transfection. CHO cells were seeded at 70–80% confluency on 24 mm cover glasses in 6-well plates at 100,000 cells per well. The next day, CHO cells was transfected using TransFectin™ Lipid Reagent (Bio-Rad, 1703351) as follows: 1.5 μg of DNA plasmid was mixed in serum free MEM medium with 3 μl transfection reagent. After 10 min of incubation, the DNA–lipid complex was added to the cells and incubated for 24 h before FRET imaging.

Single-cell Foerster Resonance Energy Transfer (FRET) imaging

For single-cell FRET imaging experiments, transfected cells were washed once and maintained in FRET buffer (10 mM HEPES, 140 mM NaCl, 5.4 mM KCl, 1 mM MgCl2, 2 mM CaCl2 (pH=7.4)) at room temperature throughout the experiment. Experiments were conducted as previously described,[106] on an inverted (Olympus IX71) microscope with a PlanApoN, 60 ×, oil immersion objective (NA 1.42) (Olympus, UK). Image acquisition and data extraction was performed using MetaFluor 7.1, (Meta Imaging Series, Molecular Devices). Donor excitation occurred at 436 nm for 100 ms every 5 seconds and fluorescent images in the donor and acceptor emission channels (480 nm and 535 nm, respectively) were recorded every 5 seconds. Baseline FRET imaging was recorded for at least one minute before treatment. Cells were treated with different concentrations of PAK1-A1 and NVS-PAK1-1. For the measurement of PKA compounds, CHO cells transfected with AKAR4 sensors were treated with each of the 20 top-scoring compounds from the virtual screening to assess their effects on PKA activity at the cellular level. Raw emission intensities were background-corrected by subtracting the fluorescence intensity of a cell-free region. Further, bleed-through of donor emission into the acceptor channel was subtracted. For all PAK1 and AKAR4 sensors, corrected FRET ratios were calculated as the ratio between background-corrected acceptor emission ($I_{acceptor}$) at 535 nm and background-corrected donor emission (I_{donor}) at 480 nm ($I_{acceptor}$ / I_{donor}). Drift corrected FRET traces were normalized (Δ FRET (%)) to the basal ratio before compound addition (set to 0%). All statistical calculations were performed with Excel and GraphPad Prism 9.

Immunoprecipitation and ADP-Glo™ Kinase Assay

For immunoprecipitation, we followed the protocol provided in the Immunoprecipitation kit (ab206996). Cells transfected with WT-PAK1-FRET biosensors and their variants were washed with PBS. Cold lysis buffer was then added, and the cells were scraped and transferred into a chilled microcentrifuge tube. The suspension was mixed on a rotary mixer for 30 minutes at 4°C, followed by centrifugation at 10,000 x g for 10 minutes at 4°C. The supernatant (cell extract) was transferred to fresh, chilled tubes for antibody binding. Anti-YFP antibody (ab286192) was added at a 1:200 dilution, and the mixture was incubated overnight at 4°C on a rotary mixer. After overnight incubation, 25-40 μL of Protein A/G Sepharose Beads I/Protein A/G Sepharose bead slurry was added to each tube and mixed for 1 hour at 4°C. The beads were then collected via low-speed centrifugation (2000 x g for 2 minutes at 4°C). Beads were washed three times with 1 mL of 1X Wash Buffer before proceeding with the kinase assay.

For the ADP-Glo™ Kinase Assay, we first generated a standard curve for ATP-to-ADP conversion before initiating the kinase reaction. Proteins obtained from the immunoprecipitation were diluted in kinase buffer. The kinase reactions were performed in 96-well plates, with 20 μL of the extracted protein, 30 μM of PAKtide substrate peptide, and 100 μM of ATP in a final reaction volume of 30 μL. The reaction proceeded for 30 minutes, after which 2 μL of ADP-Glo™ Reagent was added to stop the reaction and deplete any unconsumed ATP. Following a 40-minute incubation at room temperature, 10 μL of Kinase Detection Reagent was added to convert ADP back to ATP and introduce luciferase and luciferin to detect ATP levels. The reaction was incubated for an additional 60 minutes, and luminescence was measured using a plate-reading luminometer.

PAK1 dimerisation analysis by mass photometry

PAK1 dimerisation analysis by mass photometry was performed as previously described.[107] Briefly, purified PAK1 proteins (full-length, kinase domain, and kinase domain ^{K299R}) were diluted to 50 nM in DPBS (Corning, 21-031-CV; with or without compound treatment). Proteins treated with 10 μM PAK1-A1, 10 μM NVS-PAK1-1, and DMSO control were incubated on ice for 1 h before measurement. High-precision microscope coverslips (number 1.5H, 24×50 mm, 170±5 μm) were cleaned with repeated alternating washes of Milli-Q water and isopropanol and dried using a clean stream of air. Clean coverslips were assembled with silicone gaskets (CultureWell reusable gasket, 3-mm diameter×1-mm depth, Grace Bio-Labs), and samples were imaged using a Refeyn 2MP mass photometer. The instrument was focused against cold PBS buffer (5 μl). Protein samples (15 μl) were then added to the cold PBS (5 μl), mixed thoroughly and imaged for 60 s at 300 frames per s using the Refeyn AcquireMP (v. 2.4.1) software suite. Reported concentrations reflect sample concentrations in the final 20-μl solution. Mass photometry data were analyzed using the Refeyn DiscoverMP software suite (v.2.4.3). Raw mass photometry contrast values were converted to mass using a standard calibration of bovine serum albumin (Thermo Fisher Scientific, 23209) and thyroglobulin (Millipore, 609310). Data displayed above Gaussian fits represent apex molecular weight, standard deviation and the number of events within the Gaussian fit.

Phosphoproteomics

H9C2 cells were cultured in T25 flasks and serum-starved overnight in DMEM supplemented with 1% penicillin–streptomycin. Cells were then stimulated for 1 h with 10 μM PAK1-A1 or vehicle control (0.1% DMSO; final DMSO concentration 0.1%). The medium was discarded, and cells were washed three times with sterile 1× PBS. After the final wash, 1.5 mL sterile 1× PBS was added and cells were detached by gentle scraping with a cell spatula. The cell suspension was collected into 2 mL microcentrifuge tubes, rapidly frozen in liquid nitrogen for 15 min, and stored immediately at −80 °C. Cell pellets were subsequently shipped on dry ice to HaploX-Innovating Research, Advancing Health (HongKong, China) for MS-based phosphoproteomic analysis.

Briefly, total protein was extracted by lysing frozen cell pellets in DB buffer (6 M urea, 100 mM TEAB, pH 8.5) followed by 5 min of ultrasonication on ice. Lysates were clarified by centrifugation (12,000 × g, 15 min, 4 °C) and the supernatant was added with 1M DTT to react for 1 h (56 °C), and alkylated with iodoacetamide (room temperature, 1 h, dark). Protein quality test was determined using the Bradford protein quantitative kit. Proteins were then digested with sequencing-grade trypsin in 100 mM TEAB at 37 °C for 4 h. Digestion was quenched with formic acid (final pH < 3), and peptides were desalted on C18 cartridges, eluted with 70% acetonitrile/0.1% formic acid, and lyophilized. Phosphopeptides were enriched using TiO_2 columns according to the manufacturer's protocol (PTM Phosphorylation Enrichment Kit), washed, eluted, and dried under vacuum. Enriched peptides were resuspended in loading buffer and analyzed by LC–MS/MS using a Vanquish Neo UHPLC coupled to a Thermo Orbitrap Astral mass spectrometer equipped with an Easy-Spray ion source. Peptides were separated on a C18 analytical column under a standard gradient, and spectra were acquired in data-independent acquisition (DIA) mode. Full MS scans were collected at 240,000 resolution (m/z 380–980), followed by 300 DIA windows with NCE 25%. MS2 spectra were acquired at Astral resolution 80,000 with a maximum injection time of 3 ms.

Analysis of phosphoproteomics data

The raw files were searched and analyzed using the Spectronaut, according to the mouse UniProt database (rattus_norvegicus_uniprot_2024_07_26.fasta, 92,930 sequences) protein database. The library search parameters were set as follows: a mass tolerance of 10 ppm for precursor ions and 0.02 Da for fragment ions. Variable modifications were set such as oxidation of methionine, protein N-terminal acetylation, and phosphorylation of serine, threonine, and tyrosine residues. Carbamidomethylation of cysteine was set as the fixed modification. Two missed cleavage site was allowed at most. To improve the quality of the analytical results, the Spectronaut software further filtered the search results by retaining only credible Peptide Spectrum Matches (PSMs) with a confidence level of 99% or higher. Only credible spectral peptides and proteins were retained, and FDR validation was performed to remove

peptides and proteins with an FDR greater than 1%. A protein with a fold change (FC) greater than or less than a certain value (FC) was defined as a differentially expressed protein (DEP). The Spectronaut software (DirectDIA) was used for raw data deconvolution and species library searching. Retention time correction was performed using iRT added to the samples, and the precursor ion Qvaluecutoff value was set to 0.01. Protein quantification results were statistically analyzed using the T-test, and differentially expressed proteins were defined as those with significant quantitative differences between the experimental and control groups ($p<0.05$, $|\log2FC|>*(FC)$ or $FC<*$(fold change, FC)). Functional annotation of proteins using the InterProScan software for GO and IPR (including Pfam, PRINTS, ProDom, SMART, ProSite, PANTHER databases), and functional protein family and pathway analysis for identified proteins using COG and KEGG. Volcano plot analysis, clustering heatmap analysis, and pathway enrichment analysis of GO, IPR, and KEGG for DEPs, and prediction of potential protein-protein interactions using the STRING DB software.

Wheat germ agglutinin (WGA) staining

Wheat germ agglutinin (WGA) was used extensively to stain cell membrane by binding to N-acetyl-D-glucosamine and sialic acid residues found on the surface of cell membranes. H9C2 cells from each treatment group were fixed with 4% paraformaldehyde (PFA) for 5 minutes and then washed with phosphate-buffered saline (PBS) for 5 minutes for three times. Then, the cells were incubated with WGA (Fluor 488 conjugated wheat germ agglutinin) (5μg/ml) for 1 hour at room temperature in a dark humid chamber. The cells were finally washed with PBS for 10 minutes and mounted with Vectashield mounting medium. The images were taken at 20x magnification, and for each heart, around sizes of 400 cells were quantified by Fuji ImageJ software.

RNA isolation and RT-qPCR for ANP and BNP

Total RNA was extracted from H9C2 cell samples with Trizol. To get rid of any genomic DNA contamination, samples were given a DNAse treatment. Lunascript was used to transform RNA into cDNA. The NanoDrop2000 was used to measure the concentration and purity of RNA and cDNA from each sample. According to the manufacturer's instructions, reverse transcription-quantitative polymerase chain reaction (RT-qPCR) reactions were carried out using SYBR Select PCR Master Mix and specific primers for quantitative real-time polymerase reaction. For qPCR reactants, 10μl of SYBR, 2μl of primer, 7μl of nuclease free H2O, and 1μl of cDNA were used. Relative expression was evaluated by the2-ΔΔCt method. All experiments were performed independently in triplicate.

Generation of PAK1^{CKO} Mice

Mice with PAK1 gene disruption at both alleles were created in SV129 background and have been described previously.[108] PAK1^{CKO} mice were re-derived in FVB background and genotyped to confirm deletion of the PAK1 gene. Adult (3-4-month-old) male or female mice were used for acquisition of morphometric and biochemical analysis. Unless specifically indicated otherwise, age- and gender-matched littermates were used as WT controls. The animal studies were performed in accordance with the Guide for the Care and Use of Laboratory Animals published by the U.S. National Institutes of Health.

Ang II-Induced Cardiac Hypertrophy and PAP treatment

We used micro-osmotic pumps in all the experiments to obtain an infusion rate 0.25 μl per hour, for 7 days. Age and sex matched, 3- to 4-month-old, PAK1^{CKO} and WT mice were randomized in groups to receive seven days continuous subcutaneous administration of 1 μg/g/day Ang II plus, with or without the treatment of 1 μg/g/day PAP, or an equivalent volume of saline (control) in micro-osmotic pump (Model 1002, Alzet, Cupertino, CA). All peptides were dissolved in saline. Mice were initially anesthetized with 3% isoflurane and 100% oxygen inhaled in a closed anesthesia chamber. On day seven of the pump insertion, the animal was anaesthetized with pentobarbital (50-90 mg/kg) and the heart was excised for morphometric and biochemical analysis. A full description of the surgical procedure is reported elsewhere.[109] After the treatment, the heart weight (HW) and body weight (BW) were measured and the HW/BW ratios were calculated to indicate cardiac hypertrophy. Hypertrophic responses at the end of the treatment were analysed by histology and biochemical analysis.

Murine model of TAC and treatment of JB79

Cardiac pressure overload, to cause left ventricular hypertrophy, was induced by TAC in male mice as previously described.[49] A closed-chest transverse aortic constriction model for induction of left ventricular hypertrophy in C57 mice. Mice were anesthetized by 1.5%-2% isoflurane using the gas anesthesia machine (RWD Life Science, Shenzhen, China). In a spontaneously breathing animal following a 3-4 mm upper partial sternotomy, a segment of 6/0 silk suture threaded through between the right common carotid artery and the innominate artery and tied over a 27-gauge needle. Sham animals underwent the same surgical preparation, but without the constriction of the aorta. One day after TAC surgery, JB79 (10 mg/kg/d) or solvent-controlled DMSO was injected intraperitoneally for 14 days (1 mg JB79 + 50 μL DMSO completely dissolved). Hypertrophic responses at the end of the treatment were analyzed by heart weight/tibia length, echocardiography, histological analysis, and biochemical analysis.

E99K hypertrophic cardiomyopathy (HCM) and PAK1-A2 treatment

The transgenic E99K HCM mice were kindly provided by Prof. Hugh Watkins, Division of Cardiovascular Medicine, Radcliffe Department of Medicine, University of Oxford, Oxford, UK. Briefly, The E99K mutation was inserted into the human cardiac actin (ACTC Gene) sequence.[52] Transgene expression was restricted to the heart using an alpha-myosin heavy chain promoter construct.

Transgenic mice were generated by pronuclear microinjection of gel purified transgenic constructs into the pronucleus of fertilised mouse eggs on a C57BL10xCBA/Ca hybrid background as previously described.[52] Treated embryos were returned to a pseudo-pregnant CD-1 foster mother, generated by mating with a vasectomised male mouse, and the resultant pups were identified and genotyped by PCR from ear notch samples. At 4 weeks of age, male and female mice of WT and E99K littermates were echoed at baseline. Mice were genotyped and randomly divided into 3 groups and were treated for 6 weeks by oral administration with PAK1-A2 (10 mg/kg per day) in 0.5% (w/v) methylcellulose (MC) solution, or vehicle (0.5% MC solution). The following groups were generated and studied: WT, E99K-vehicle, and E99K-PAK1-A2. Hypertrophic responses at the end of the treatment were analyzed by heart weight/tibia length, echocardiography, histological analysis, and biochemical analysis.

Histological analysis

Hearts were removed from mice anaesthetized with 3-5% isoflurane and transferred to 4% polyformaldehyde in PBS for fixation for 48 h and processed into paraffin. Heart sections (5 μm) were prepared for light microscopy and stained with Hematoxylin and Eosin (Abcam, ab245880), Masson's Trichrome (Abcam, ab150686), or Picro-Sirius Red staining (Abcam, ab245887) techniques, following the manufacturer's guidance. Images were acquired using Pannoramic SCAN (3DHISTECH Ltd. Hungary) to scan the whole film. Analysis of the fibrotic area of the tissue is expressed as a percentage and the mean cross-sectional area of cardiomyocytes measurement were both calculated by using Fuji ImageJ.

Echocardiography and Analysis

For TAC model and the treatment of JB79, mice were anesthetized with 1%-1.5 % isoflurane. Parasternal short-axis section (PSAX) B-mode and M-mode echocardiographic were recorded using the Vevo3100 micro-ultrasound imaging system (FUJIFLIM VisualSonics Inc., Canada). Three measurements taken at end-systole (s) and end-diastole (d) were averaged to calculate corresponding values of intraventricular septal thickness (IVSs and IVSd), left ventricular posterior wall thickness (LVPWs and LVPWd), and left ventricular diameter end-diastolic (LVIDd) and left ventricular diameter end-systolic (LVIDs). Ejection fraction (EF) and fractional shortening (FS) were also acquired from the recorded measurements.

For E99K model and PAK1-A2 treatment, mice were first anesthetized by placing the mouse in a plexiglas chamber connected to vaporizer providing isoflurane at 2% in 100% O2. Once induced, the mouse was then secured in the supine position on a warming plate, isoflurane concentration was reduced to 1.5-2% and hair removed from the chest using depilating agent. Body temperature was monitored and kept to 37°C throughout the procedure. Transthoracic echocardiography was performed using a Vevo 2100 In Vivo Imaging System (VisualSonics). Anatomical M-Mode images of the left ventricle (LV) were taken from the parasternal long axis view to measure ejection fraction (%), stroke volume (μL), and the LV wall thicknesses. All measurements and calculations were averaged from three consecutive cycles. Data analysis was performed offline with the Vevo 770 Analytic Software (VisualSonics).

Immunoblot analyses

To measure the PAK1 activation induced by PAK1-A1, PAK1-A2, and ISO treatment. Cultured neonatal cardiomyocytes and HH9C2 cells were washed with DEPC-PBS and lysed with lysis buffer. Lysates were collected, vortexed for 30 seconds, placed on ice for 10minutes, and repeated 2-3 times. The prepared samples were centrifuged at 13500 rpm for 15 minutes at 4°C, and the supernatant protein was collected to estimate the protein concentration with BCA reagent. In this research, protein 20μg per well. SDS-PAGE gels of 8% or 12% were used depending on the molecular weight of the target protein. After electrophoresis, the gel was transferred to a polyvinylidene fluoride (PVDF) membrane. The transferred PVDF membrane was blocked with blocking buffer containing 5% nonfat dry milk for one hour. Primary antibodies (p-PAK1, 2601, Cell Signaling Technology; t-PAK1, 2602, Cell Signaling Technology; p-MEK1, 98195, Cell Signaling Technology; t-MEK1, 9124, Cell Signaling Technology; p-Merlin, 9163, Cell Signaling Technology; t-Merlin, 6995, Cell Signaling Technology) were diluted to 1:1000 in 5% dry milk and incubated overnight on a shaker at 4°C. After the membranes were incubated with horseradish peroxidase-linked secondary antibody, they were stained with ECL. Image Pro Plusv6.0 was used to quantify protein bands.

For TAC model treatment immunoblots, 20 μg total protein for each lane was separated using 5% stacking gel and 8-12% separation gel, and transferred to a 0.45 μm PVDF membrane (Millipore, USA). The membrane was incubated in TBST containing 5% non-fat milk for 1 h at room temperature and was incubated with the primary antibody overnight at 4 °C. The primary antibodies for ANP (ab180649, Abcam, 1:500), phosphorylated PAK1 (p-PAK1, 2601, Cell Signaling Technology, 1:300), total-PAK1 (t-PAK1, 2602, Cell Signaling Technology, 1:1000), phosphorylated-ERK (p-ERK, 4370, Cell Signaling Technology, 1:1000), total-ERK (t-ERK, 4695, Cell Signaling Technology, 1:1000), phosphorylated-JNK (p-JNK 9251, Cell Signaling Technology, 1:1000), total-JNK (t-JNK, 9252, Cell Signaling Technology, 1:1000), phosphorylated-MKK7 (p-MKK7, 4171, Cell Signaling Technology, 1:1000), total-MKK7 (t-MKK7, 4172, Cell Signaling Technology, 1:1000), phosphorylated-MKK4 (p-MKK4, 9151, Cell Signaling Technology, 1:1000), total-MKK4 (t-MKK4, 9152, Cell Signaling Technology, 1:1000) and GAPDH (Santa Cruz Biotechnology, 1:1000) as the internal control were used. The membrane was incubated with the secondary antibody (1:1000) Goat anti-mouse IgG HRP (BBI life sciences, China) or Goat anti-rabbit IgG HRP (BBI life sciences, China) for 1 h at room temperature. The immunoreactions were visualized using chemiluminescent HRP Substrate (Millipore, USA), then imaged protein bands with the Universal Hood II System (Bio-Rad, USA).

For E99K mouse model treatment immunoblots, total protein from tissues was obtained with Triton lysis buffer (Tris 20 mM, NaCl 137 mM, EDTA 2 mM, 1% Triton X-100, β-glycerophosphate 25 mM, Na3VO4 1 mM, phenylmethanesulfonylfluoride 1 mM, aprotinin 1.54 μM, leupeptin 21.6 μM, 10% glycerol; pH 7.4). Protein concentration was determined by Bio-Rad protein assay. Protein extracts (30 μg) were subject to immunoblot analyses with antibodies (all antibodies applied in this study were used as 1:1000 dilution) against PAK1 (Cell Signaling, 2602), CHOP (Cell Signaling, 2895), phospho-PAK1 (Cell signaling, 2601), phospho-PERK (Cell Signaling, 3179), ATF6 (Abcam, ab37149), BiP (Cell signaling, 3183), ATF4 (Abcam, ab85049), GADPH (Cell Signaling, 92310). Immune-complexes were detected by enhanced chemiluminescence with anti-mouse, anti-rabbit or anti-goat immunoglobulin-G coupled with horseradish peroxidase.

QUANTIFICATION AND STATISTICAL ANALYSIS

Quantification methods and tools used are described in each relevant section of the methods or figure legends. Regarding the dose response curve, the Non-linear curve fit was performed using a three-parameter equation [agonist vs response] in GraphPad Prism and was shown as mean ± S.E.M unless otherwise stated. Asterisks in the figures indicate the level of statistical significance ($^{*}p < 0.05$, $^{**}p < 0.01$, $^{***}p < 0.001$, and $^{****}p < 0.0001$) as determined using either two-tailed unpaired Student t test or one-way ANOVA test as defined in figure captions. Tests were performed using GraphPad Prism software (Version 9 and 10, GraphPad Software, La Jolla, CA, United States). Data are expressed as Mean ± S.E.M unless otherwise stated.

Supplemental figures

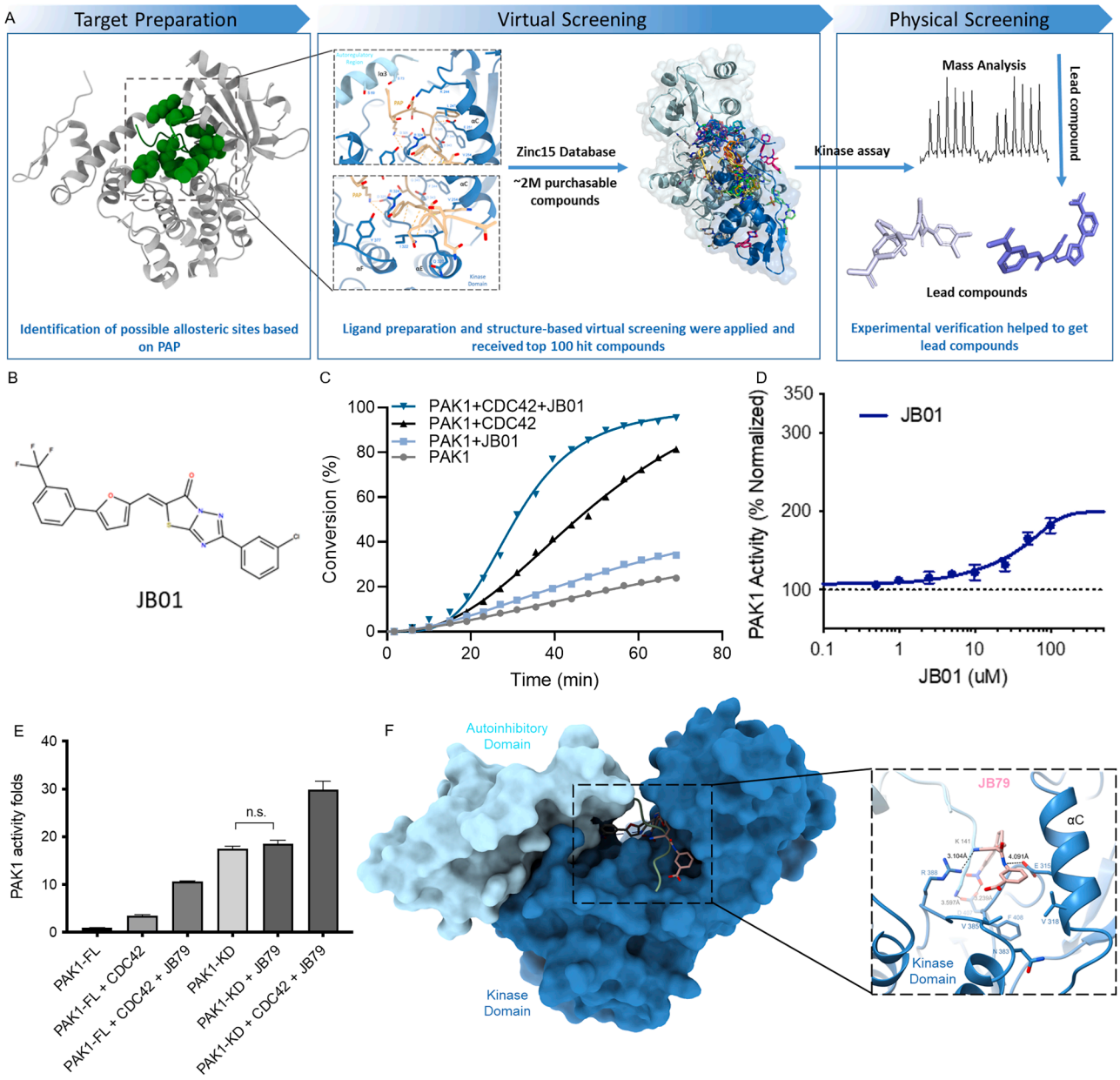

Figure S1. Identification of direct PAK1 activators targeting autoinhibition-release site, related to Figure 1

(A) Summary of a computational and physical protocol for identification of small-molecule modulators of PAK1 activity. The pipeline comprises three major components: a potential allosteric site was identified through PAP binding pose and ICM-VLS program was used to screen the identified pocket against a ZINC[15] lead-like library, followed by a bioactivity physical screening of 100 top-ranking hit compounds using RapidFire-MS based kinase activity assay.

(B) Chemical structures of PAK1 activator JB01.

(C) PAK1 activity with or without the treatment of its upstream modulator, Cdc42, and JB01.

(D) Dose-response curves for JB01 on PAK1 activity in the presence of Cdc42. Data are presented as mean ± SEM. $n = 3$.

(E) PAK1 activity under different conditions, including full-length and kinase domain only, with or without treatment with JB79. Data are presented as mean ± SEM. $n = 3$. $^{*}p < 0.05$, ns, not significantly different according to one-way ANOVA with Tukey's post hoc test.

(F) Predicted interaction of JB79 with residues in the autoinhibition-release site. JB79 is highlighted in pink.

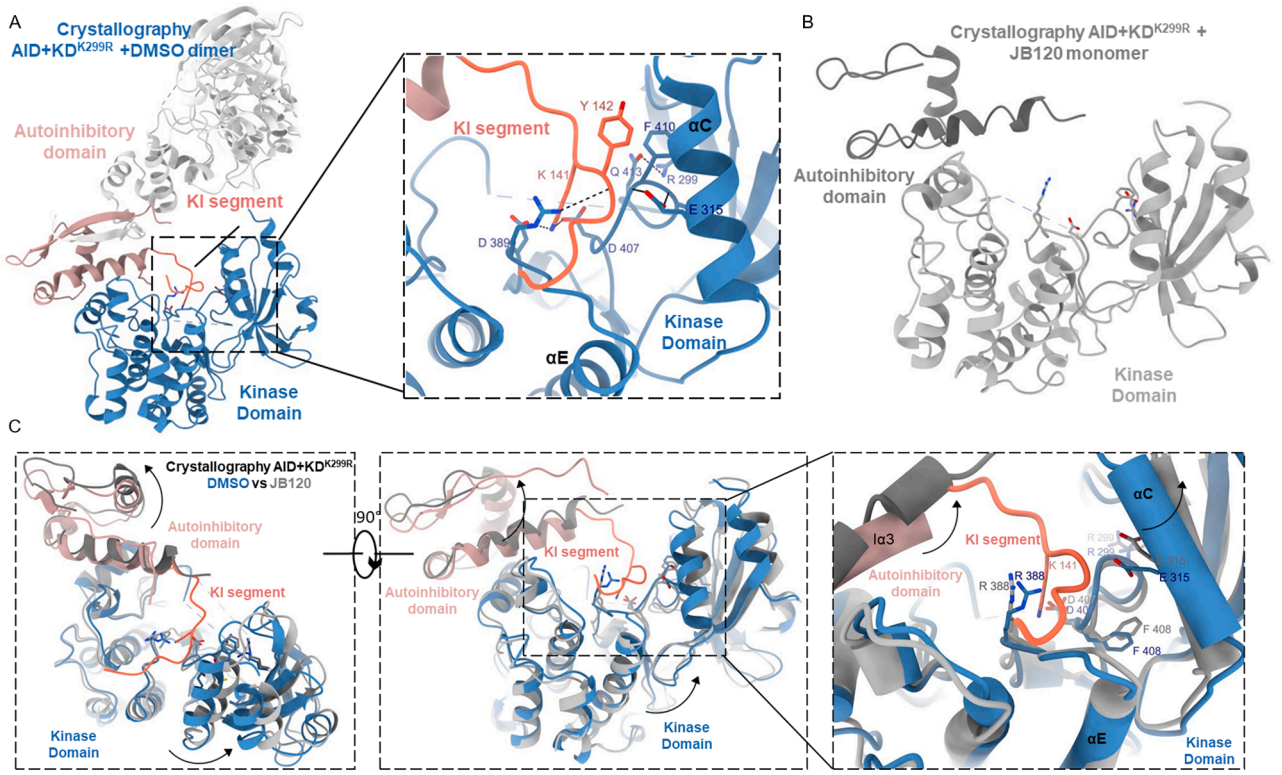

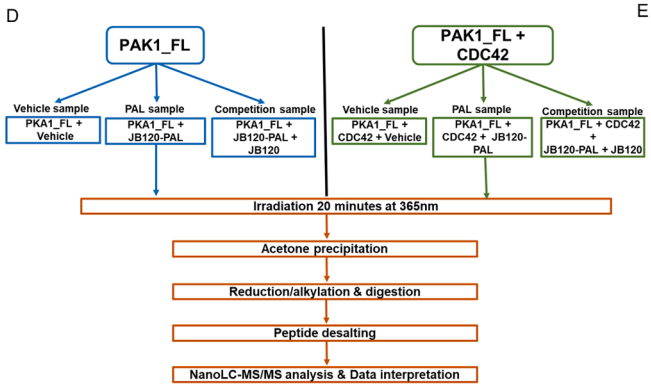

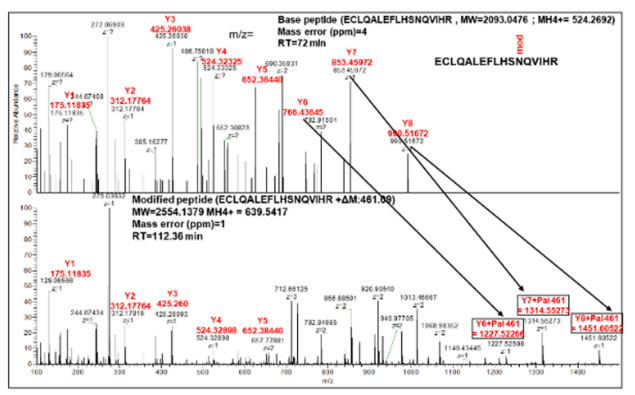

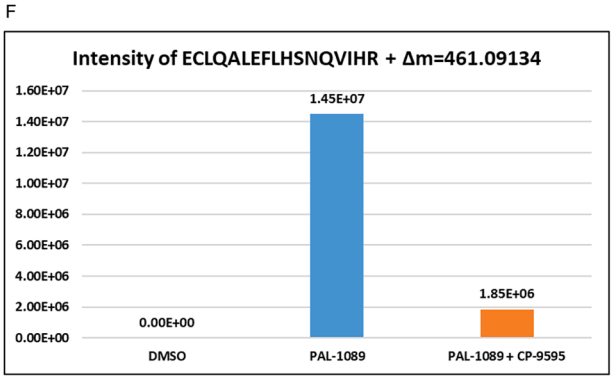

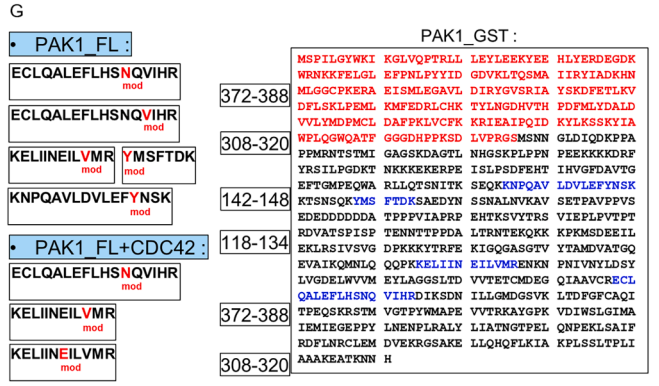

(legend on next page)

Figure S2. Identification of key residues involved in PAK1 activator binding, related to Figure 2

(A) Overview of the crystal structure of PAK1 autoinhibitory domain in complex with kinase domain^{K299R} treated with DMSO showing dimerization within an asymmetric unit. Detailed view shows the inhibited active site of PAK1.

(B) Crystal structure of PAK1 autoinhibitory domain and kinase domain^{K299R} complex soaked with JB120 showing a *cis*-autoinhibited structure.

(C) Crystallographic superimposition overview (left) of PAK1 autoinhibitory domain in complex with kinase domain^{K299R} treated with DMSO (autoinhibitory domain in pink and kinase domain in dark blue) and the structure soaked with JB120 (gray). Detailed view (right) indicates both local and global conformational alterations.

(D) Schematic for PAL-MS assay. JB120-PAL reporter was pre-incubated with PAK1 protein, UV crosslinked, and digested for proteomic analysis. Due to the importance of Cdc42 in potentially increasing the affinity of the compound binding, another condition was added to introduce Cdc42 in addition to the PAK1 full-length alone. Furthermore, a competitive assay was applied using JB120-PAL together with JB120 compound to confirm the binding of PAK1 activator.

(E) Representative mass spectrum shows the mass shift of peptide involved in the binding of JB120-PAL.

(F) Representative quantitative proteomics analysis revealed the ΔM mass shift corresponding to JB120-PAL (461.09 kDa). Significantly reduced mass shift of peptides was observed when the competitive compound JB120 was co-incubated with the JB120-PAL probe.

(G) Mass-shifted peptide alignment with PAK1 sequence. Four peptides highly abundant with mass shift were observed in full-length PAK1 treated with PAL-120, while only two peptides were found to have the mass shift in the presence of Cdc42. Key residues contributing to activator's binding were highlighted in red.

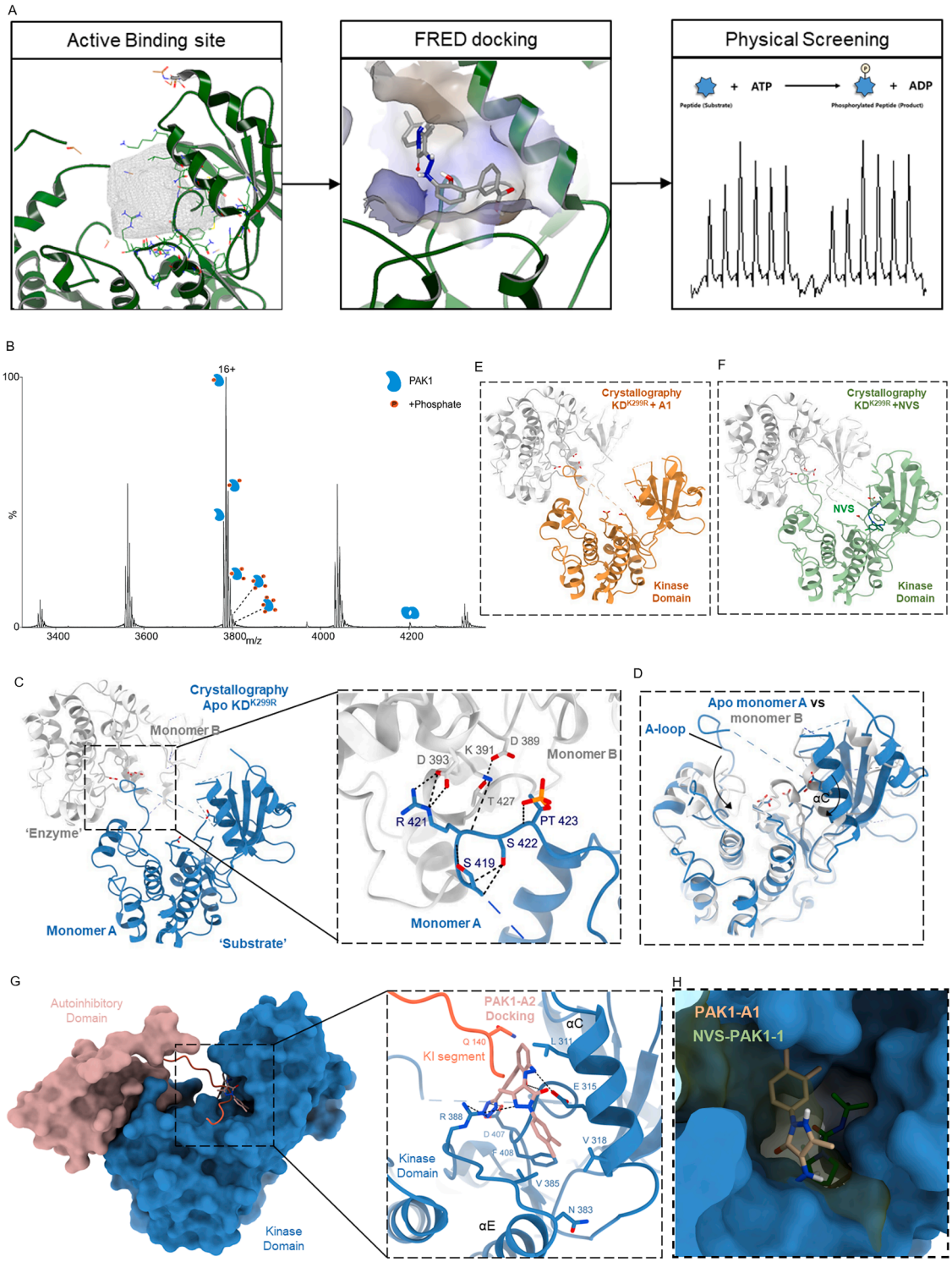

Figure S3. Development of direct small-molecule PAK1 activators, related to Figure 3

(A) Summary of a computational and physical screening protocol for identification of small-molecule modulators of PAK1 activity. Pocket for ligand screening was based on PAL-MS refined site. The make receptor program (left) was applied to generate active binding sites for ligands. FRED docking (middle) was then performed for virtual screening against the ZINC[15] FDA-approved drugs and drug-like compound library, followed by a bioactivity physical screening of the top-ranking hit compounds using RapidFire-MS based kinase activity assay (right).

(legend continued on next page)

(B) The native mass spectrum of full-length PAK1 reveals peaks corresponding to the apo monomer of full-length PAK1 and its various phosphorylated states (black). Multiple (up to five) phosphorylation binding events (red) were observed. The measured masses are 60,471 ± 1, 60,552 ± 1, 60,632 ± 1, 60,713 ± 1, 60,793 ± 1 and 61,193 ± 1 Da.
(C) Overview and detailed view of the crystal structure of apo PAK1 kinase domain^{K299R} showing dimerization within an asymmetric unit.
(D) Superposition of two PAK1-kinase domain^{K299R} monomers. The N lobe of monomer B (gray) undergoes a nearly rigid 200° rotation about the long axis of the kinase domain, and its activation segment (cyan) differs greatly from that of monomer A (blue).
(E and F) Crystal structures of PAK1 kinase domain^{K299R} soaked with PAK1-A1 (E) and in complex with NVS-PAK1-1 (F), showing dimerization within an asymmetric unit.
(G) Overview (left) and predictive detailed interaction (right) of PAK1-A2 with residues in the autoinhibition-release site. PAK1-A2 is shown in pink.
(H) Detailed view of PAK1-A1 (orange) and NVS-PAK1-1 (green) binding to PAK1 reveals their overlapping binding site.

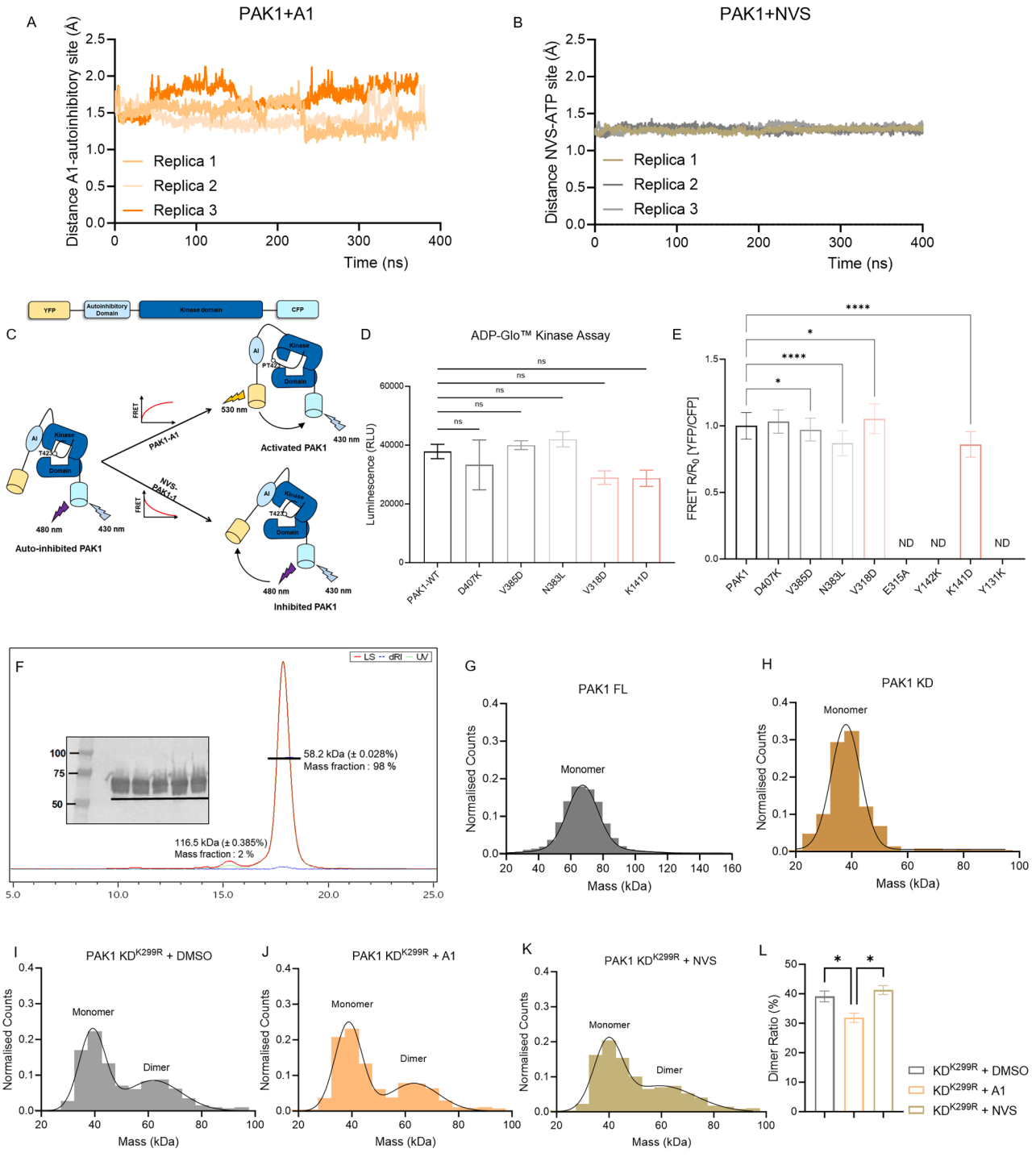

Figure S4. PAK1 global conformational changes regulated by small-molecule modulators, related to Figure 4

(A and B) Results from simulations demonstrate the predictive distance between PAK1-A1 (A) and NV-PAK1-1 (B) to the center of the binding sites. Each trace represents independent simulations, with both PAK1 + PAK1-A1 and PAK1 + NV-PAK1-1 having three replicates.

(C) Schematic for PAK1-FRET biosensor, which was C-terminally fused to donor cyan fluorescent protein (CFP) and N-terminally fused to yellow fluorescent protein (YFP).

(D) Determination of the kinase activity of WT PAK1-FRET biosensor and variants. WT PAK1-FRET and mutated PAK1 constructs were transfected into CHO cells, followed by immunoprecipitation. PAK1 proteins were pulled down using an anti-YFP antibody in conjunction with A/G beads and subjected to ADP-Glo kinase assay to measure kinase activity. *n* = 3, ns represents no statistical significance.

(legend continued on next page)

(E) Normalized static FRET ratio calculations of WT PAK1-FRET biosensor and mutated biosensors after transfection. ND, not expressed in CHO cells or led to cell death. Data are presented as mean ± SEM. $n = 3$. ****$p < 0.0001$, *$p < 0.05$, ns, not significantly different according to one-way ANOVA with Tukey's post hoc test.
(F) Gel filtration peaks and the representative gel blot for full-length PAK1.
(G and H) Mass distributions of PAK1 monomer with full-length PAK1 (G) and active PAK1 kinase domain (H) by mass photometry. $n = 3$.
(I–K) Mass distributions of PAK1 monomer and dimer with the treatment of DMSO (I), PAK1-A1 10 μM (J), and NVS-PAK1-1 10 μM (K) by mass photometry.
(L) Quantification of the dimerization ratio by mass photometry as shown in (I)–(K). Data are presented as mean ± SEM. $n = 3$. *$p < 0.05$ according to one-way ANOVA with Tukey's post hoc test.

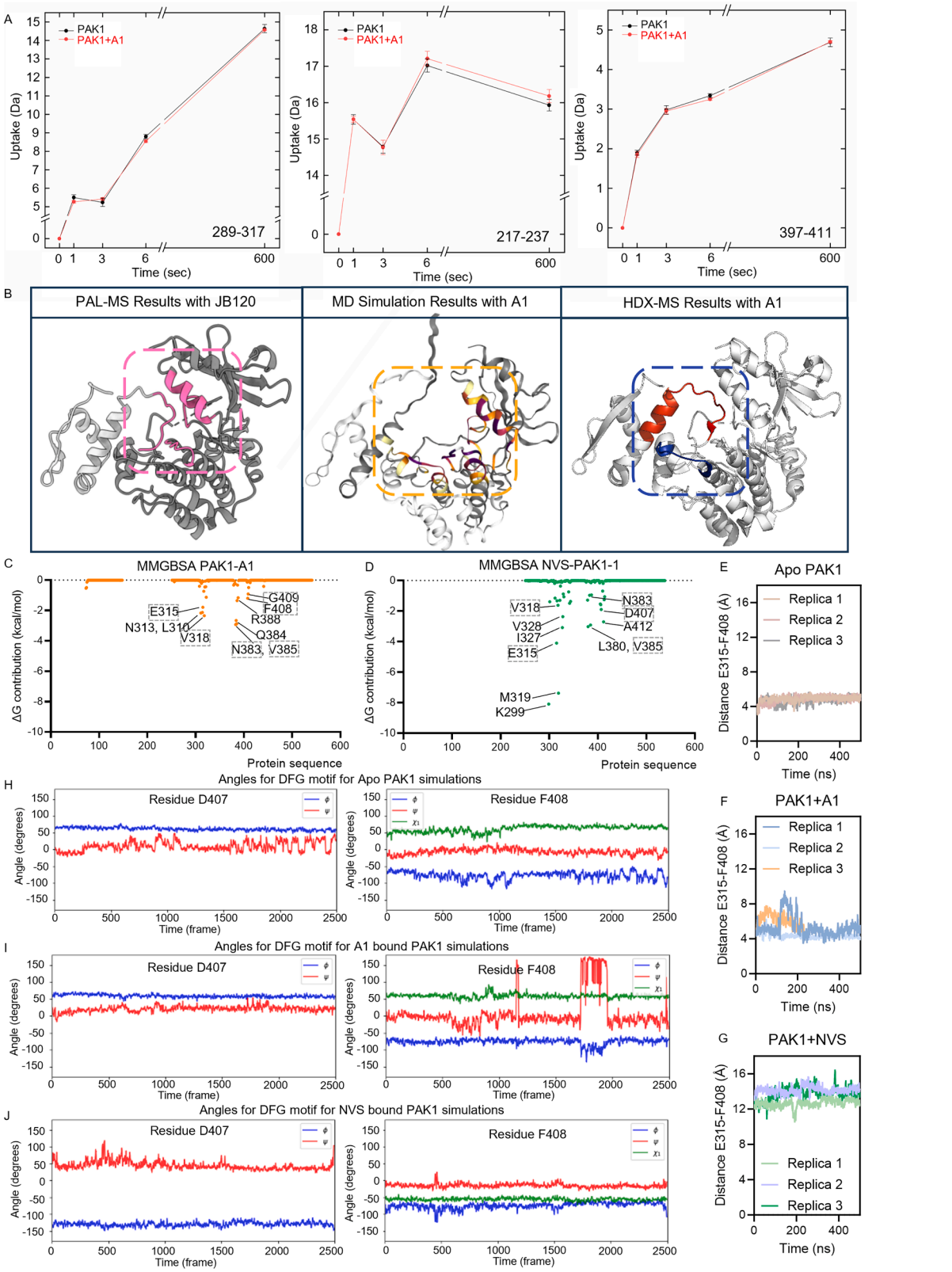

(legend on next page)

Figure S5. HDX-MS and molecular dynamic simulations reveal the binding site and mechanism of action of PAK1-A1, related to Figure 5

(A) Selected peptides uptake from HDX-MS results are shown. Peptide 289–317 within the kinase domain exhibits decreased exchange ($\Delta D_{A1bound\text{-}apo} \approx -0.19$ at 6 s), peptide 217–237 within the flexible loop displays increased exchange ($\Delta D_{A1bound\text{-}apo} \approx 0.19$ at 6 and 600 s), and an example peptide 397–411 shows no detectable difference between PAK1-A1 treated and apo-PAK1 protein. Red traces correspond to PAK1-A1-treated samples (holo-PAK1) and black traces to apo-PAK1 controls. Four labeling time points were measured with up to five replicates acquired for each.

(B) Comparison of proposed PAK1 activator binding sites from different assays, including PAL-MS results using JB120, and the PAK1-A1-binding site predicted by molecular dynamics simulations and validated by HDX-MS. The binding site of PAK1 activators is localized at the interface between the kinase domain and the autoinhibitory domain.

(C and D) Molecular mechanic generalized Born free energy calculations reveal key residues involved in PAK-A1 (C) and NVS-PAK1-1 (D) binding to full-length PAK1. Key residues involved in the binding for both PAK1-A1 and NVS-PAK1-1 are highlighted in gray.

(E–G) Results from molecular dynamic simulations of Apo PAK1 (PDB: 1F3M) (E), PAK1-A1 (F), and NV-PAK1-1-bound PAK1 (G), showing predictive distance between two key residues Glu315 on αC helix and Phe408 on activation loop. Each trace represents independent simulations, with all Apo PAK1, PAK1 + PAK1-A1 and PAK1 + NV-PAK1-1 having three replicates.

(H–J) Molecular dynamic simulation investigates the torsion of the DFG motif upon ligand binding. Torsion angles D407, Phe408, and Gly409 under 400 ns simulations for Apo full-length PAK1 (H), PAK1-A1-bound PAK1 (I), and NV-PAK1-1-bound PAK1 (J).

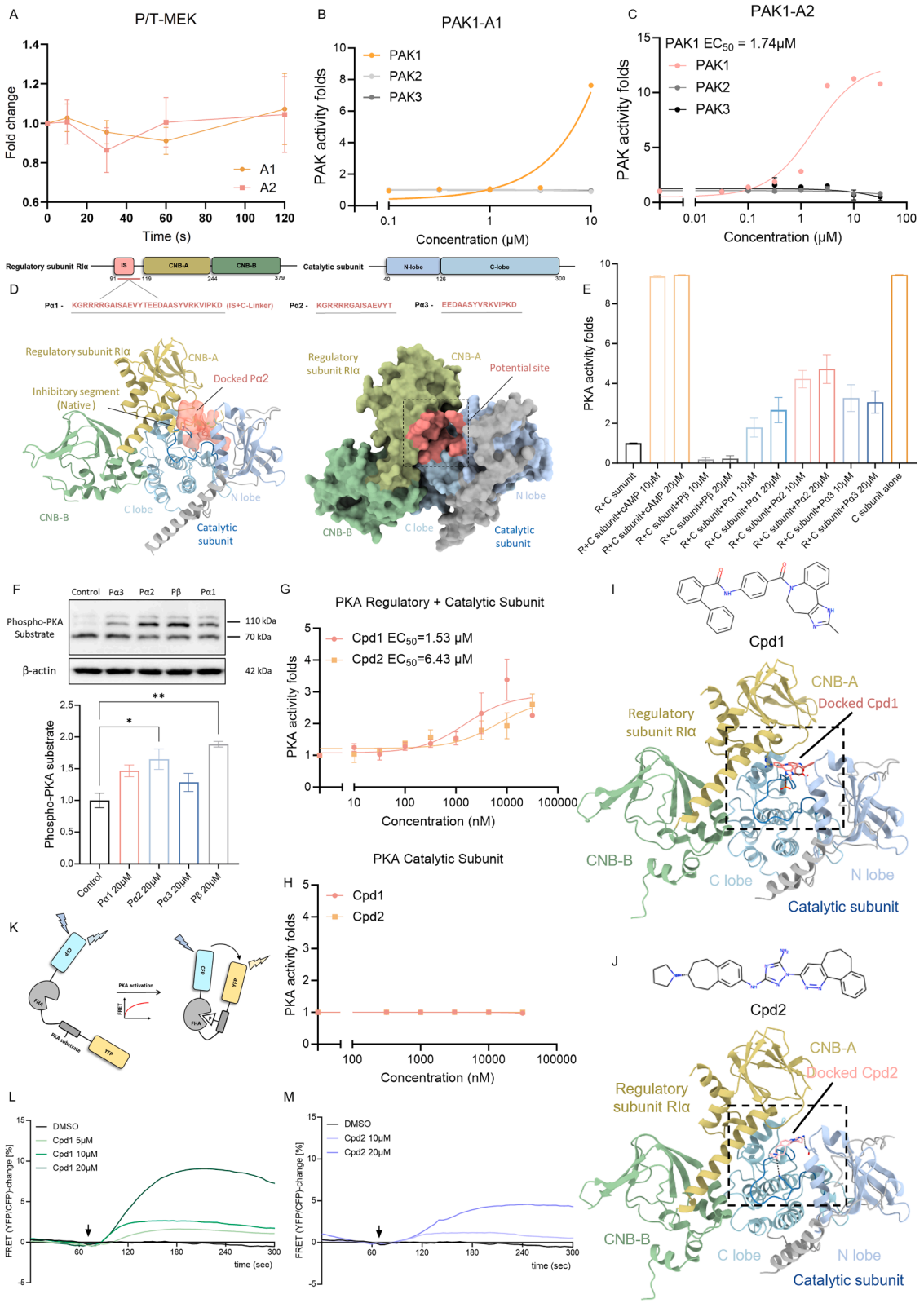

(legend on next page)

Figure S6. Downstream PAK1 signaling induced by activators and proof-of-concept identification of PKA activators targeting an analogous autoinhibition-release site, related to Figure 6

(A) Quantification of phosphorylated MEK1 (Ser298) relative to total PAK1 in cells treated with PAK1-A1 or PAK1-A2 (n = 4 independent experiments).

(B) Dose-response analysis of PAK1-A1 against PAK1–3 using the ^{33}PanQinase radiometric kinase assay (Reaction Biology Service).

(C) Dose-response curves showing selective activation of full-length PAK1 compared with PAK2 and PAK3 by PAK1-A2 using RapidFire-MS assay (n = 2). Data are presented as mean ± SD.

(D) (Top) Pα1 sequence, derived from both the inhibitory segment and its C-linker region within the PKA regulatory subunit RIα, Pα2 sequence corresponds to the inhibitory segment, and Pα3 sequence corresponds to the C-linker region. (Bottom) AlphaFold2 predicted model for Pα2-bound PKA RIα (UniProt: P10644) and catalytic subunit (UniProt: P17612) complex (left) and the potential allosteric active site for PKA activator screening (right). Docked Pα2: shown in coral red, this segment is the Pα2 peptide docked into the PKA RIα and catalytic subunit complex structure. Native inhibitory segment and C-linker: shown in lime green, this is the native inhibitory segment within the PKA RIα structure. For presentation clarity, the sequence preceding the RIα region, including the D/D domain (aa 1–90), has been removed.

(E) RapidFire-MS kinase assay measures the effect of PKA modulating peptides on PKA activity.

(F) PKA modulating peptides enhance cellular PKA activity evidenced by increased phosphorylated PKA substrate levels through immunoblot assays.

(G and H) Dose-response curves for Cpd1 and Cpd2 on PKA activity under different conditions, including the PKA RIα and catalytic subunit complex (G), as well as the catalytic subunit alone (H). Data are presented as mean ± SEM. n = 3. $^{**}p < 0.01$, $^{*}p < 0.05$ according to one-way ANOVA with Tukey's post hoc test.

(I and J) (Top) Chemical structures of cAMP independent PKA activators, Cpd1 (I) and Cpd2 (J). (Bottom) Molecular docking predicted interaction of Cpd1 (I) and Cpd2 (J) within their autoinhibition-release sites. PKA structure PDB: 2QCS was used in the docking. Considering that the inhibitory segment occupies the potential allosteric site for ligand binding within the PKA structure, the inhibitory segment (aa 91–103) was removed during the docking process.

(K) Schematic for AKAR4 FRET biosensor, which exploits a protein domain that can undergo a large conformational change upon PKA-dependent phosphorylation. AKAR4 reaches maximum FRET when an intramolecular portion of the sensor is phosphorylated by PKA.

(L and M) PKA activators, Cpd1 (L) and Cpd2 (M), induce PKA phosphorylation and increase the FRET ratios of AKAR4 sensors. Time courses of FRET ratio changes in CHO cells expressing AKAR4 sensors are normalized to baseline (set to 0%).

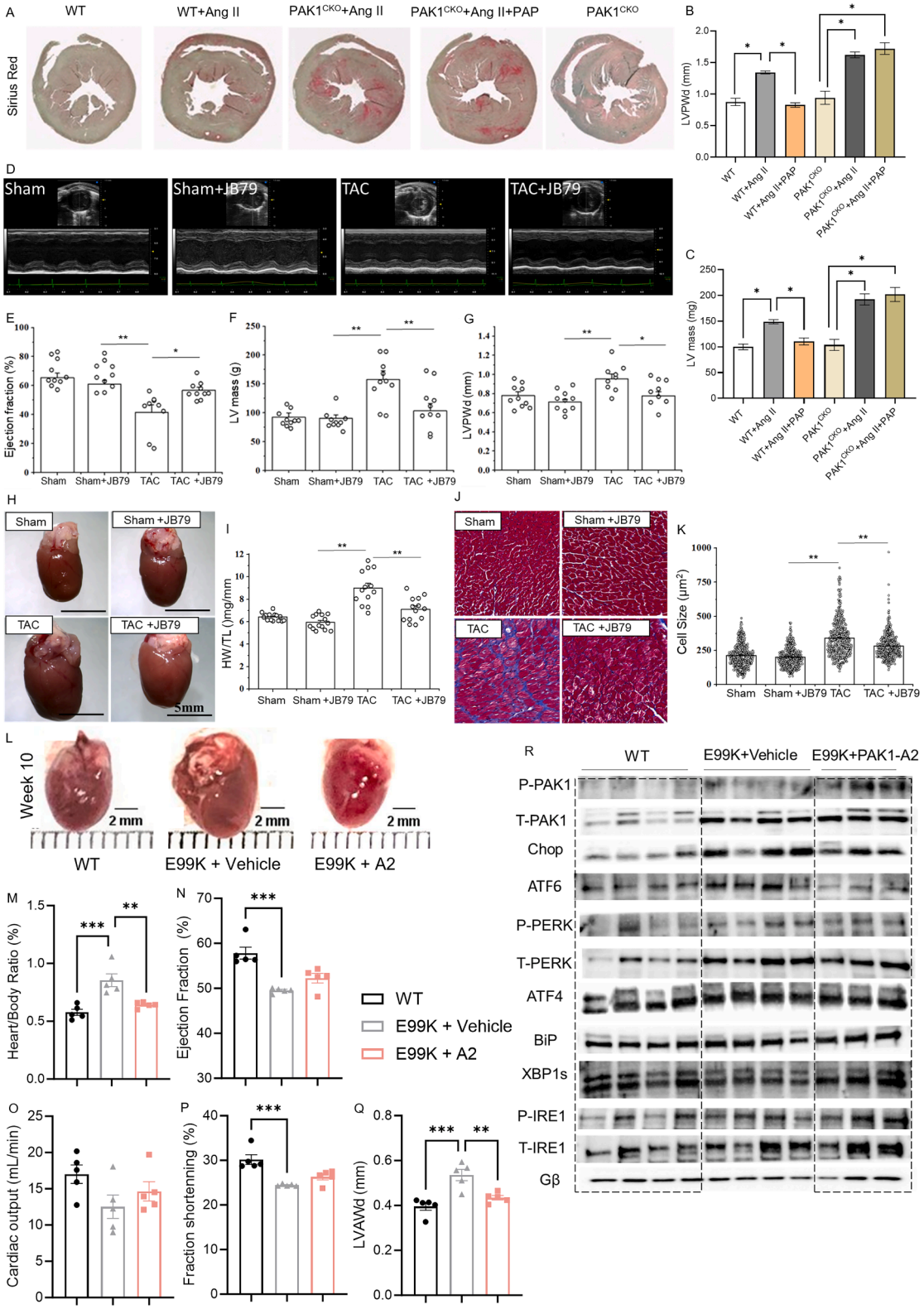

(legend on next page)

Figure S7. Therapeutic evaluation of PAP, JB79, and PAK1-A2 in cardiac hypertrophy models, related to Figure 7

(A–C) Representative images (A) and quantification of LVPW thickness (B) and LV mass (C) evaluated after Sirius red staining for WT and PAK1-knockout (KO) treated with vehicle, angiotensin II (Ang II) and PAP. Data are presented as mean ± SEM. WT ($n = 6$), WT + Ang II ($n = 6$), WT + Ang II + PAP ($n = 6$), $PAK1^{CKO}$ ($n = 5$), $PAK1^{CKO}$ + Ang II ($n = 5$), and $PAK1^{CKO}$ + Ang II + PAP ($n = 5$); equal representation of males and females was used.

(D–G) Representative images of echocardiography (D) and quantification of key parameters, including ejection fraction (E), LV mass (F), and LVPW thickness (G) for sham and TAC mice treated with vehicle and JB79. Data are presented as mean ± SEM. Only male mice were included in this study.

(H and I) Representative images (H) and quantification of heart/body weight (I) for sham and TAC mice treated with vehicle and JB79. Data are presented as mean ± SEM. Only male mice were included.

(J and K) Representative images (J) and quantification of myocyte cell size (K) evaluated after Masson trichrome staining for sham and TAC mice treated with vehicle and JB79. Data are presented as mean ± SEM. $n = 10$.

(L and M) Representative images (L) and quantification of heart/body weight (M) for WT and the HCM mice treated with vehicle and PAK1-A2 (10 mg/kg).

(N–Q) Quantification of fractional shortening, cardiac output, ejection fraction, and diastolic LV anterior wall thickness for echocardiography measurement. $n = 5$ (2 males and 3 females). Data are presented as mean ± SEM. $^{***}p < 0.001$, $^{**}p < 0.01$, $^{*}p < 0.05$ according to one-way ANOVA with Tukey's post hoc test.

(R) Representative immunoblot of ER-stress-related key markers using heart tissues from WT and E99K mice treated with vehicle and PAK1-A2.